NASA/TM-2000-210287
ARL-TR-2207

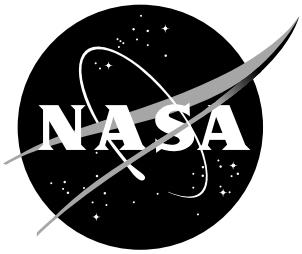

A Shell/3D Modeling Technique for the Analysis of Delaminated Composite Laminates

Ronald Krueger
National Research Council
Langley Research Center, Hampton, Virginia

T. Kevin O'Brien
U.S. Army Research Laboratory
Vehicle Technology Directorate
Langley Research Center, Hampton, Virginia

June 2000

The NASA STI Program Office ... in Profile

Since its founding, NASA has been dedicated to the advancement of aeronautics and space science. The NASA Scientific and Technical Information (STI) Program Office plays a key part in helping NASA maintain this important role.

The NASA STI Program Office is operated by Langley Research Center, the lead center for NASA's scientific and technical information. The NASA STI Program Office provides access to the NASA STI Database, the largest collection of aeronautical and space science STI in the world. The Program Office is also NASA's institutional mechanism for disseminating the results of its research and development activities. These results are published by NASA in the NASA STI Report Series, which includes the following report types:

- TECHNICAL PUBLICATION. Reports of completed research or a major significant phase of research that present the results of NASA programs and include extensive data or theoretical analysis. Includes compilations of significant scientific and technical data and information deemed to be of continuing reference value. NASA counterpart of peer-reviewed formal professional papers, but having less stringent limitations on manuscript length and extent of graphic presentations.

- TECHNICAL MEMORANDUM. Scientific and technical findings that are preliminary or of specialized interest, e.g., quick release reports, working papers, and bibliographies that contain minimal annotation. Does not contain extensive analysis.

- CONTRACTOR REPORT. Scientific and technical findings by NASA-sponsored contractors and grantees.

- CONFERENCE PUBLICATION. Collected papers from scientific and technical conferences, symposia, seminars, or other meetings sponsored or co-sponsored by NASA.

- SPECIAL PUBLICATION. Scientific, technical, or historical information from NASA programs, projects, and missions, often concerned with subjects having substantial public interest.

- TECHNICAL TRANSLATION. English-language translations of foreign scientific and technical material pertinent to NASA's mission.

Specialized services that complement the STI Program Office's diverse offerings include creating custom thesauri, building customized databases, organizing and publishing research results ... even providing videos.

For more information about the NASA STI Program Office, see the following:

- Access the NASA STI Program Home Page at ***http://www.sti.nasa.gov***

- E-mail your question via the Internet to help@sti.nasa.gov

- Fax your question to the NASA STI Help Desk at (301) 621-0134

- Phone the NASA STI Help Desk at (301) 621-0390

- Write to:
  NASA STI Help Desk
  NASA Center for AeroSpace Information
  7121 Standard Drive
  Hanover, MD 21076-1320

NASA/TM-2000-210287
ARL-TR-2207

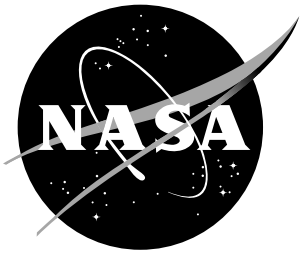

A Shell/3D Modeling Technique for the Analysis of Delaminated Composite Laminates

Ronald Krueger
National Research Council
Langley Research Center, Hampton, Virginia

T. Kevin O'Brien
U.S. Army Research Laboratory
Vehicle Technology Directorate
Langley Research Center, Hampton, Virginia

National Aeronautics and
Space Administration

Langley Research Center
Hampton, Virginia 23681-2199

June 2000

The use of trademarks or names of manufacturers in the report is for accurate reporting and does not constitute an official endorsement, either expressed or implied, of such products or manufacturers by the National Aeronautics and Space Administration or the U.S. Army.

Available from:

NASA Center for AeroSpace Information (CASI)
7121 Standard Drive
Hanover, MD 21076-1320
(301) 621-0390

National Technical Information Service (NTIS)
5285 Port Royal Road
Springfield, VA 22161-2171
(703) 605-6000

A SHELL/3D MODELING TECHNIQUE FOR THE ANALYSIS OF DELAMINATED COMPOSITE LAMINATES

Ronald Krueger[1] and T. Kevin O'Brien[2]
[1] National Research Council Research Associate
[2] U.S. Army Research Laboratory, Vehicle Technology Directorate
NASA Langley Research Center
Hampton, VA 23681

ABSTRACT

A shell/3D modeling technique was developed for which a local three-dimensional solid finite element model is used only in the immediate vicinity of the delamination front. The goal was to combine the accuracy of the full three-dimensional solution with the computational efficiency of a plate or shell finite element model. Multi-point constraints provided a kinematically compatible interface between the local three-dimensional model and the global structural model which has been meshed with plate or shell finite elements. Double Cantilever Beam (DCB), End Notched Flexure (ENF), and Single Leg Bending (SLB) specimens were analyzed first using three-dimensional finite element models to obtain reference solutions. Mixed mode strain energy release rate distributions were computed across the width of the specimens using the virtual crack closure technique. The analyses were repeated using the shell/3D technique to study the feasibility for pure mode I (DCB), mode II (ENF) and mixed mode I/II (SLB) cases. Specimens with a unidirectional layup and with a multidirectional layup where the delamination is located between two non-zero degree plies were simulated. For a local three-dimensional model, extending to a minimum of about three specimen thicknesses on either side of the delamination front, the results were in good agreement with mixed mode strain energy release rates obtained from computations where the entire specimen had been modeled with solid elements. For large built-up composite structures the shell/3D modeling technique offers a great potential for reducing the model size, since only a relatively small section in the vicinity of the delamination front needs to be modeled with solid elements.

KEY WORDS

Composite materials, fracture mechanics, strain energy release rate, finite element analysis, virtual crack closure technique.

INTRODUCTION

One of the most common failure modes for composite structures is delamination. The remote loadings applied to composite components are typically resolved into interlaminar tension and shear stresses at discontinuities that create mixed-mode I and II delaminations. To characterize the onset and growth of these delaminations the use of fracture mechanics has become common practice over the past two decades [1-3]. The total strain energy release rate, G, the mode I component due to interlaminar tension, G_I, the mode II component due to interlaminar sliding shear, G_{II}, and the mode III component, G_{III}, due to interlaminar scissoring shear, are calculated from continuum (2D) and solid (3D) finite element analyses using the virtual crack closure technique [4-8]. In order to predict delamination onset or growth, these calculated G components are compared to interlaminar fracture toughness properties measured over a range from pure mode I loading to pure mode II loading [9-12].

Three-dimensional finite element models have been used to study the behavior of specimens used in fracture toughness testing [7,13-15], as well as the behavior of edge delaminations [1,16] and near-surface delaminations in composite laminates [17,18]. Since many layers of brick elements through the thickness are often necessary to model the individual plies, the size of finite element models required for accurate analyses may become prohibitively large. To improve computational efficiency, built-up structures are therefore traditionally modeled and analyzed using plate or shell finite elements. Computed mixed mode strain energy release rate components, however, depend on many variables such as element order and shear deformation assumptions, kinematic constraints in the neighborhood of the delamination front, and continuity of material properties and section stiffness in the vicinity of the debond when delaminations or debonds are modeled with plate or shell finite elements [7,19]. For example, in reference 19, mesh refinement studies showed that computed G_I, G_{II}, and G_{III} did not converge when the structure above and below the plane of delamination was modeled with plate elements with different section properties (thickness or layup). A comparison of computed mixed mode strain energy release rates obtained from plate models with values computed from three-dimensional models showed differences in results near the free edges of the structure where the stress state is three-dimensional

[20]. These problems may be avoided by using three-dimensional models. Furthermore, three-dimensional analyses are required when matrix cracks and multiple delaminations need to be modeled at different ply interfaces. Three-dimensional analyses become necessary e.g. to analyze the skin/stringer debonding discussed in reference 21, where the failure at the flange tip is inherently three-dimensional as shown in Figure 1. Matrix cracks and delaminations at different ply interfaces need to be modeled with solid elements. Therefore, methods based on three-dimensional modeling to calculate fracture parameters in built-up structures need to be improved.

The overall objective of the current work is to develop a shell/3D modeling technique for which a local solid finite element model is used only in the immediate vicinity of the delamination front and the remainder of the structure is modeled using plate or shell elements. The goal of the shell/3D technique is to combine the computational efficiency of a plate or shell finite element model with the accuracy of the full three-dimensional solution in the areas of interest. Multi-point constraints provide a kinematically compatible interface between the local three-dimensional model and the surrounding global structural model, which can be meshed with plate or shell finite elements. For large composite structures, the shell/3D modeling technique offers great potential for saving modeling and computational effort because only a relatively small section in the vicinity of the delamination front needs to modeled with solid elements as shown in Figure 2. A significant reduction in model size can be expected compared to a full three-dimensional model.

In the current investigation, the feasibility of the shell/3D technique proposed is studied for the pure mode I case, mode II case and a mixed mode I/II case. This is accomplished by using simple specimens like the double cantilever beam (DCB), end notched flexure (ENF), and single leg bending (SLB) specimens. First, all three specimens were modeled entirely with solid elements to validate the three-dimensional model, select suitable element types and an appropriate mesh size around the delamination front. These results were used as reference solutions for comparison with values obtained from the shell/3D technique. For each specimen, mixed mode strain energy release rate distributions were computed across the width from nonlinear finite element analyses using the virtual crack closure technique [3-5]. The length of the local three-dimensional model around the delamination front was increased until the results computed were within 1% of mixed mode strain energy release rates obtained from computations where the entire specimen had been modeled with solid elements.

SPECIMEN DESCRIPTION

For this investigation the double cantilever beam (DCB), the end notched flexure (ENF), and the single leg bending (SLB) specimens, as shown in Figure 3, were chosen to study the feasibility of the shell/3D technique for the pure mode I case, mode II case and a mixed mode I/II case, respectively. In general DCB, ENF and mixed mode tests are performed on unidirectionally reinforced laminates, which means that delamination growth occurs at a [0/0] interface and crack propagation is parallel to the fibers. Although this unidirectional layup is desired for standard test methods to characterize fracture toughness, this kind of delamination growth will rarely occur in real structures. Previously, a number of combined experimental and numerical studies on unidirectional and multidirectional laminates have been performed where the critical strain energy release rates of various interfaces were evaluated under mode I, mode II and mixed-mode conditions [13, 14, 15, 22, 23]. Three different laminates were selected from these previous studies. The unidirectional layup $[0]_{32}$ was designated UD32, the unidirectional layup $[0]_{24}$ was designated UD24 and the multidirectional layup [±30/0/-30/0/30/0_4/30/0/-30/0/-30/30/$_{\uparrow}$-30/30/0/30/0/-30/0_4/30/0/30/0/±30] was designated D±30. The arrow denotes the location of the delamination, which for all three laminates was located in the midplane. For interfacial delaminations between two orthotropic solids care must be exercised in interpreting the computed mixed mode energy release rates obtained from the virtual crack closure technique. This will be discussed in detail in the section on the SLB specimen with D±30 layup. The UD32 and D±30 layup were made of C12K/R6376 graphite/epoxy and the UD24 layup was made of T300/1076 graphite/epoxy. The material properties are given in Table 1 and the layup is summarized in Table 2.

ANALYSIS FORMULATION

FINITE ELEMENT ANALYSIS

The goal of this investigation was to study the accuracy of the shell/3D modeling technique by comparing strain energy release rates computed using the shell/3D modeling technique to results obtained from full three-dimensional models. Therefore, all three specimens were first modeled entirely with solid elements. A typical three-dimensional finite element model of a specimen is shown in Figure 4(a). For the entire investigation, the ABAQUS® geometric nonlinear analysis procedure was used. To study the influence of element selection on the global load/deflection behavior and the computed mixed mode strain energy release rates, several three-dimensional solid

element types were used to model the specimens. The use of standard solid eight-noded brick element C3D8, incompatible mode element C3D8I, reduced integration element C3D8R as well as solid twenty-noded hexahedral elements C3D20 and reduced integration element C3D20R was studied. Shear locking is common in first-order, fully integrated elements, such as C3D8, that are subject to bending. The numerical formulation of this element gives rise to shear strains that do not really exist. Therefore, these elements are too stiff in bending, and many elements over the thickness are required to obtain acceptable results. Elements where a lower-order, reduced integration is used to form the element stiffness such as the C3D8R and C3D20R elements usually provide more accurate results in bending and reduce running time. Incompatible mode elements, such as C3D8I are also recommended for bending and contact problems. In these elements internal deformation modes are added to the standard displacement modes of the element in order to eliminate the parasitic shear stresses that occur in bending [24]. Interpenetration of the delaminated faces was prevented by using multi point constraints or contact elements [24]. Results will be discussed in detail in the following chapter.

The specimens with unidirectional layup were modeled by six elements through the specimen thickness as shown in the detail of Figure 4(b). For the specimens with D±30 layup, two plies on each side of the delamination were modeled individually using one element for each ply as shown in Figure 4(a). The adjacent four plies were modeled by one element with material properties smeared using the rule of mixtures [25]. The adjacent element extended over the four 0˚ plies. The six outermost plies were modeled by one element with smeared material properties. The delamination was modeled as a discrete discontinuity in the center of the specimen, with separate, unconnected nodes (with identical coordinates) on the upper and lower surfaces of the delaminated section. Referring to Figure 4, the specimens were divided into a center section of width, f, and a refined edge section, e, to capture local edge effects and steep gradients. These sections appear as dark areas in the full view of the specimen. Along the length of the model, a refined mesh of length, c, was used in the vicinity of the delamination front as shown in Figure 4(a). To study the influence of the mesh size around the delamination front on computed mixed mode strain energy release rates, the length, c, of the refined zone and the number of elements in the zone were varied, as will be discussed in detail later.

A shell/3D model of a typical specimen is shown in Figure 4(b). The global section was modeled with ABAQUS® four-noded quadrilateral S4 type shell elements. The local three-dimensional section was modeled with ABAQUS® solid eight-noded C3D8I type elements. A combination of reduced integrated eight-noded quadrilateral shell elements S8R with solid twenty-noded hexahedral elements C3D20R was also studied. The transition from the global shell element model to the local three-dimensional model in the vicinity of the delamination front was accomplished by using multi-point constraint options given by ABAQUS® to enforce appropriate

translations and rotations at the shell-solid interface [24]. The theory used for the multi-point constraint option assumes that the interface between the shell elements and solid elements is a surface containing the normals to the shell along the line of intersection of the meshes, so that the lines of nodes on the solid mesh side of the interface in the normal direction to the surface are straight lines. The nodes on the solid mesh side have the possibility of moving along the line and the line is allowed to change length, which means that there are no constraints in thickness direction [24]. An improved coupling of the shell element model to the local three-dimensional model may be obtained by the use of special transition elements using formulations for the shell/3D transition based on a higher-order shell theory [26].

Along the length of the model a refined mesh of length c=5 mm with 10 elements was used for the UD24 layup, c= 3.0 mm, 12 elements for the D±30 layup, and c= 6.0 mm, 24 elements was used for the UD32 layup in the vicinity of the delamination front. These section lengths, c, had been selected in previous studies [14, 15, 23] and remained unchanged during the current investigations. To study the influence of the size of the local zone on computed mixed mode strain energy release rates, the total length of the local zone modeled with solid elements, d, was varied between 10 to 30 mm, in 5mm increments.

VIRTUAL CRACK CLOSURE TECHNIQUE

The Virtual Crack Closure Technique (VCCT) was used to calculate strain energy release rates [3-5]. The mode I, mode II and mode III components of the strain energy release rate, G_I, G_{II} and G_{III}, were calculated for eight noded solid elements as shown in Figure 5

$$G_I = -\frac{1}{2\Delta A} \cdot Z'_{Li} \cdot \left(w'_{L\ell} - w'_{L\ell^*} \right)$$

$$G_{II} = -\frac{1}{2\Delta A} \cdot X'_{Li} \cdot \left(u'_{L\ell} - u'_{L\ell^*} \right)$$

$$G_{III} = -\frac{1}{2\Delta A} \cdot Y'_{Li} \cdot \left(v'_{L\ell} - v'_{L\ell^*} \right)$$

with $\Delta A = \Delta a \cdot b$ [5]. Here ΔA is the area virtually closed, Δa is the length of the elements at the delamination front and b is the width of the elements. For better identification in this and the following figures, columns are identified by capital letters and rows by small letters. Hence, X'_{Li}, Y'_{Li} and Z'_{Li} denote the forces at the delamination front in column L, row i, and $u'_{K\ell}$, $v'_{K\ell}$ and $w'_{K\ell}$ are the relative displacements at the corresponding node row ℓ behind the delamination front as shown in Figure 5. For geometrically nonlinear analysis, both forces and displacements were transformed into a local coordinate system (x', y'), that defined the normal and tangential coordinate directions

at the delamination front in the deformed configuration.

For twenty noded solid elements the equations to calculate the strain energy release rate components at the element corner nodes (location Li) as shown in Figure 6 are as follows [17]

$$G_I = -\frac{1}{2\Delta A}\left[\frac{1}{2}Z'_{Ki}\left(w'_{K\ell} - w'_{K\ell^*}\right) + Z'_{Li}\left(w'_{L\ell} - w'_{L\ell^*}\right) + Z'_{Lj}\left(w'_{Lm} - w'_{Lm^*}\right) + \frac{1}{2}Z'_{Mi}\left(w'_{M\ell} - w'_{M\ell^*}\right)\right]$$

$$G_{II} = -\frac{1}{2\Delta A}\left[\frac{1}{2}X'_{Ki}\left(u'_{K\ell} - u'_{K\ell^*}\right) + X'_{Li}\left(u'_{L\ell} - u'_{L\ell^*}\right) + X'_{Lj}\left(u'_{Lm} - u'_{Lm^*}\right) + \frac{1}{2}X'_{Mi}\left(u'_{M\ell} - u'_{M\ell^*}\right)\right]$$

$$G_{III} = -\frac{1}{2\Delta A}\left[\frac{1}{2}Y'_{Ki}\left(v'_{K\ell} - v'_{K\ell^*}\right) + Y'_{Li}\left(v'_{L\ell} - v'_{L\ell^*}\right) + Y'_{Lj}\left(v'_{Lm} - v'_{Lm^*}\right) + \frac{1}{2}Y'_{Mi}\left(v'_{M\ell} - v'_{M\ell^*}\right)\right].$$

Here X'_{Ki}, Y'_{Ki} and Z'_{Ki} denote the forces at the delamination front in column K, row i, and $u'_{K\ell}$, $v'_{K\ell}$ and $w'_{K\ell}$ are the relative displacements at the corresponding column K, node row ℓ behind the delamination front as shown in Figure 6. Similar definitions are applicable in column M for the forces at node row i and displacements at node row ℓ and in column L for the forces at node row i and j and displacements at node row ℓ and m respectively. As mentioned previously, for geometrically nonlinear analysis, both forces and displacements were transformed into a local coordinate system (x', y'), that defined the normal and tangential coordinate directions at the delamination front in the deformed configuration. The equations to calculate the strain energy release rate components at the mid side node (location Mi) as shown in Figure 7 are as follows [17]

$$G_I = -\frac{1}{2\Delta A}\begin{bmatrix}\frac{1}{2}Z'_{Li}\left(w'_{L\ell} - w'_{L\ell^*}\right) + \frac{1}{2}Z'_{Lj}\left(w'_{Lm} - w'_{Lm^*}\right) + Z'_{Mi}\left(w'_{M\ell} - w'_{M\ell^*}\right)\\ +\frac{1}{2}Z'_{Ni}\left(w'_{N\ell} - w'_{N\ell^*}\right) + \frac{1}{2}Z'_{Nj}\left(w'_{Nm} - w'_{Nm^*}\right)\end{bmatrix}$$

$$G_{II} = -\frac{1}{2\Delta A}\begin{bmatrix}\frac{1}{2}X'_{Li}\left(u'_{L\ell} - u'_{L\ell^*}\right) + \frac{1}{2}X'_{Lj}\left(u'_{Lm} - u'_{Lm^*}\right) + X'_{Mi}\left(u'_{M\ell} - u'_{M\ell^*}\right)\\ +\frac{1}{2}X'_{Ni}\left(u'_{N\ell} - u'_{N\ell^*}\right) + \frac{1}{2}X'_{Nj}\left(u'_{Nm} - u'_{Nm^*}\right)\end{bmatrix}$$

$$G_{III} = -\frac{1}{2\Delta A}\begin{bmatrix}\frac{1}{2}Y'_{Li}\left(v'_{L\ell} - v'_{L\ell^*}\right) + \frac{1}{2}Y'_{Lj}\left(v'_{Lm} - v'_{Lm^*}\right) + Y'_{Mi}\left(v'_{M\ell} - v'_{M\ell^*}\right)\\ +\frac{1}{2}Y'_{Ni}\left(v'_{N\ell} - v'_{N\ell^*}\right) + \frac{1}{2}Y'_{Nj}\left(v'_{Nm} - v'_{Nm^*}\right)\end{bmatrix}.$$

Additional information with respect to the application of the VCCT and improved equations for

twenty noded solids are given in the literature [4-8, 17].

The total strain energy release rate, G_T, was obtained by summing the individual mode components as

$$G_T = G_I + G_I + G_{III} .$$

The data required to perform the Virtual Crack Closure Technique were accessed from the ABAQUS® result file. The calculations were performed in a separate post-processing step using nodal displacements and nodal forces obtained from elements at the delamination front.

ANALYSIS OF SPECIMENS WITH UNIDIRECTIONAL LAYUP

Numerical validation of the finite element models and the post processing to compute the mixed mode strain energy release rates was performed using three-dimensional models of unidirectionally laminated DCB, ENF and SLB specimens. For each specimen, mixed mode strain energy release rate distributions were computed across the width from nonlinear finite element analyses using the virtual crack closure technique. Results were used as reference solutions for comparison with values obtained from the shell/3D technique. The analyses were then repeated using the shell/3D modeling technique to study the feasibility for pure mode I (DCB), mode II (ENF) and mixed mode I/II cases (SLB).

COMPUTATION OF STRAIN ENERGY RELEASE RATES ACROSS A STRAIGHT DELAMINATION FRONT IN A DCB SPECIMEN WITH UNIDIRECTIONAL LAYUP

For this investigation, the symmetry of the DCB specimen was taken into account and only one half of the specimen width B/2 was modeled as shown in Figure 8(a). The influence of element selection on the global load/deflection behavior and the computed mode I strain energy release rates was studied using ABAQUS® C3D8, C3D8I, C3D8R, C3D20 and C3D20R type elements to model the specimen. Along the length of the model, a refined mesh of length, c, was used in the vicinity of the delamination front. This section length, c, was varied to determine the length required for accurately computing the mixed mode strain energy release rates. For this study, the specimen was modeled with C3D8I elements and the number of elements, n, was varied accordingly to keep the element size constant as shown in Figures 8(a) to (c). Additionally, the influence of mesh size on computed mixed mode strain energy release rates was studied by keeping the length of the refined zone, c, constant, and increasing the number of elements, n, in this zone

as shown in Figures 9(a) to (c). The specimen was divided into a center section of width, f, and a refined edge section of width, e, to capture local edge effects and steep gradients. Section widths and mesh sizes used in the current investigation were taken from a previous study [23] where the effect of mesh size across the width on computed mixed mode energy release had been investigated.

To study the influence of element selection on the global load/deflection behavior and the computed mixed mode strain energy release rates the mesh shown in Figure 8(b) was used for all element types. The load/deflection behavior of the specimen is shown in Figure 10 where the tip opening displacement δ, as shown in Figure 3(a), is plotted versus the applied load P. The deformation behavior computed using C3D8I, C3D20 and C3D20R elements matches previous results using solid twenty-noded hexahedral elements [23], the model therefore accurately captured the global response of the specimen. The classical eight noded brick element, C3D8, however, shows the tendency to lock, which means that an unnaturally stiff behavior of the structure is observed during computation. The eight noded brick element with reduced integration, C3D8R appears to model an excessively compliant structural behavior. In Figure 11 the computed mode I strain energy release rate normalized with respect to the value from beam theory,

$$G_{I,beam}(a) = \frac{12 \cdot a^2 \cdot P^2}{B^2 \cdot h^3 \cdot E_1}$$

is plotted versus the normalized width, y/B, of the specimen. Here, a denotes the delamination length, P the external load, B the specimen width, h the thickness of the cantilever arms as shown in Figure 3 and E_1 the modulus of elasticity. Strain energy release rates obtained from models using C3D8I, C3D20 and C3D20R elements are in excellent agreement with the values from the analyses using twenty noded solid elements [13]. The mode I strain energy release rate is fairly constant in the center part of the specimen progressively dropping towards the edges causing the straight front to grow into a curved front as explained in detail in the literature [8, 13, 27, 28]. As expected, the mode II and mode III strain energy release rates are computed to be nearly zero and hence are not shown. The results indicate that the post processing module used to compute the strain energy release rate using VCCT operates accurately. The model made of C3D8 elements yields results which do not correctly capture the drop of the mode I strain energy release rate towards the edge. Studies, where the model made of C3D8 elements was repeatedly refined in all three spatial directions verify that the load/deflection behavior and the strain energy release rates converge to the results reported for the higher order elements. The mixed mode strain energy release rates computed from the model made of C3D8R elements are noticeably higher across the entire width compared to the other results. The response of specimens modeled with C3D8R elements was not investigated any further. Compared to the model made of C3D20 elements the

models made of C3D8I and C3D20R yield nearly the same results and require less computation time. Therefore these element types were chosen for the following studies.

The influence of the length, c, of the refined section around the delamination tip (Figure 8) on the computed mode I strain energy release rate distribution across the width of a DCB specimen was studied next for a model made of C3D8I type elements. As the length of the refined section was increased, the element length was kept constant at Δa=0.5 mm. The plot in Figure 12 indicates that the length, c, has only a small influence on the computed strain energy release rate distribution. In order to be consistent with previous studies [13, 23], a length of c= 5 mm was chosen for the local section of the shell/3D model. Additionally, the influence of mesh size was studied. The mesh size is defined as the length of the elements in the refined section, c, which is identical to the length, Δa, of the elements at the delamination tip. The influence on the mode I strain energy release rate distribution across the width is moderate as shown in Figure 13 and only very long elements (n=2, Δa =5 mm) need to be avoided. Hence, ten elements (n=10) were chosen for the local three-dimensional section of the shell/3D model, which leads to an element length of Δa=0.5 mm at the delamination tip.

A shell/3D model of a DCB specimen is shown in Figure 14(a). The global section was modeled with S8R type shell elements. The local three-dimensional section was modeled with solid C3D20R type elements. A combination of quadrilateral shell elements S4 with solid eight-noded elements C3D8I, was also studied. Along the length a refined mesh of length c=5 mm with 10 elements was used in the vicinity of the delamination front. This section length, c, was kept constant during the entire investigation. To study the influence of the length of the local zone on computed mixed mode strain energy release rates, the total length of the local zone modeled with solid elements, d, was varied (d=10, 15, 20, 25, 30 mm) as shown in Figures 14 (a) to (f).

The computed strain energy release rate distributions across the width of the specimen are shown in Figure 15 for the combination of twenty noded brick elements in the local three-dimensional model with eight noded shell elements in the global model. As expected, the mode II and mode III strain energy release rates are computed to be nearly zero and hence are not shown. With increasing length of the local three-dimensional model, d, computed results from the shell/3D model converge to the solution obtained from a full three-dimensional model. For a local three-dimensional model extending to a minimum of about three specimen thicknesses in front and behind the delamination front (d/2h=6.67), the results were within 1% of the mode I strain energy release rates obtained from computations where the entire specimen had been modeled with solid elements. The shell/3D model is capable of accurately simulating the anticlastic bending effect that causes the strain energy release rate to be highest in the center of the specimen and lowest at its edges. Results for the combination of eight noded brick elements with four noded shell elements are shown in Figure 16. When compared to the model with twenty noded solids and eight noded

shell elements, the combination of eight noded brick elements with four noded shell elements yields identical results and provides a reduced model size. Therefore, the combination of eight noded brick elements with four noded shell elements was used for the remainder of this study.

COMPUTATION OF STRAIN ENERGY RELEASE RATES ACROSS A STRAIGHT DELAMINATION FRONT IN AN ENF SPECIMEN WITH UNIDIRECTIONAL LAYUP

For this investigation, the symmetry of the ENF specimen was taken into account and only one half of the specimen width $B/2$ was modeled as shown in Figure 17. The influence of element selection on the computed mode II strain energy release rates was studied using ABAQUS® C3D8, C3D8I, C3D8R, C3D20 and C3D20R type elements to model the specimen. Along the length of the model a section $c=10\ mm$ was used for the refined mesh in the vicinity of the delamination front. Twenty elements were used yielding an element length $\Delta a=c/n=0.5\ mm$. This mesh size was found suitable during the initial investigation of the DCB specimen described in the previous section. Interpenetration of the cantilever arms was first prevented by using contact elements [24]. A previous study [23] showed that penetration of the arms could be prevented by introducing multi point constraints in the plane of delamination only along a string of nodes above the left support as schematically shown in Figure 18. The use of multi point constraints appears advantageous as less modeling effort is required and a computationally expensive contact analysis is avoided. Therefore, the influence of the multi point constraint technique on the computed mode II and mode III strain energy release rates was also studied.

In Figures 19 and 20 the computed mode II and mode III strain energy release rates normalized with the reference value, $G_{II,beam}$, from classical beam theory (not accounting for transverse shear)

$$G_{II,beam}(a) = \frac{9 \cdot a^2 \cdot P^2}{16 \cdot B^2 \cdot h^3 \cdot E_1} \ .$$

are plotted versus the normalized width, y/B, of the specimen. Computed mode II and mode III strain energy release rates obtained from models using C3D8I, C3D20 and C3D20R elements are in excellent agreement with the values from previous analyses using twenty noded solid elements [13]. The mode II strain energy release rate is fairly constant across almost the entire width of the specimen, peaking in the immediate vicinity of the edges. The mode III contribution is zero in the center of the specimen peaking to about only 5% of $G_{II,beam}$ at the edges. The computed G_I values are nearly zero and therefore are not shown. The model made of C3D8 elements yields results which do not correctly capture the mode II and III distribution. The mode II values computed from

the model made of C3D8R elements appear excessively high across the entire width. These observations support the results obtained from the study of the UD24 DCB specimen discussed above. Models made of C3D8 and C3D8R elements were not investigated any further. Compared to the model made of C3D20 elements the models made of C3D8I elements yield nearly the same results and provide a reduced model size. Therefore this element type was chosen for the following studies.

Computed mode II and mode III strain energy release rates obtained from models where the penetration of the cantilever arms was prevented by multi point constraints or contact analysis are shown in Figure 21. The results shown are in almost exact agreement. Therefore, the technique using the multi point constraints to avoid penetration was used for the remainder of this study.

A shell/3D model of an ENF specimen is shown in Figure 22. The global section was modeled with quadrilateral shell elements S4. The local three-dimensional section was modeled with eight-noded C3D8I type elements. Along the length, a refined mesh of length $c=5$ mm with 10 elements was used in the vicinity of the delamination front. As discussed in the study of the DCB specimen above, the section length, c, was kept constant during the entire investigation. To study the influence of the length of the local zone on computed mixed mode strain energy release rates, the total length of the local zone modeled with solid elements, d, was varied ($d=10$, 15, 20, 25, 30 mm) as shown in Figures 14 (a) to (f).

The computed mode II and III strain energy release rate distributions across the width of the specimen are shown in Figures 23 and 24. As expected, the mode I strain energy release rate is computed to be nearly zero and hence is not shown. With increasing length of the local three-dimensional model, d, computed results from the shell/3D model converge to the solution obtained from a full three-dimensional model. For a local three-dimensional model extending to a minimum of about three specimen thicknesses in front and behind the delamination front ($d/2h=6.67$), the results were within 1% of the mode II strain energy release rates obtained from computations where the entire specimen had been modeled with solid elements. The results obtained from all shell/3D models are in excellent agreement with the mode III strain energy release rate obtained from computations where the entire specimen had been modeled with solid elements as shown in Figure 24. For a unidirectional layup, however, the mode III contribution is very small. Therefore, the influence of the size of the local three-dimensional model on mode II and mode III separation needs to verified for a case where the mode III contribution is more obvious and the mode II contribution is less dominant. This will be discussed in the section on the ENF specimen with multidirectional layup.

COMPUTATION OF STRAIN ENERGY RELEASE RATES ACROSS A STRAIGHT DELAMINATION FRONT IN A SLB SPECIMEN WITH UNIDIRECTIONAL LAYUP

The single leg bending (SLB) specimen, as shown in Figure 3(c), was introduced for the determination of fracture toughness as a function of mixed mode I/II ratio [15]. This test may be performed in a standard three point bending fixture such as that used for the ENF test. By varying the relative thickness of the delaminated regions (t_1 and t_2) various mode mixities may be achieved. The test is of particular interest because compliance calibration can be used to accurately determine the critical strain energy release rate [15]. This type of specimen was selected for this study to verify that the shell/3D modeling technique is also capable of accurately simulating the mixed mode I/II case. Mixed mode strain energy release rates which served as reference solutions had been computed in a previous study using three-dimensional FE models [23].

For this investigation, the symmetry of the SLB specimen was taken into account and only one half of the specimen width $B/2$ was modeled as shown in Figure 25. The finite element model is basically identical to the one used for the ENF and DCB specimens discussed in the previous sections, except the boundary conditions were modified by omitting the suppressions simulating the lower support pin of the ENF test. The influence of element selection on the computed mixed mode strain energy release rates was studied using ABAQUS® C3D8, C3D8I, C3D8R, C3D20 and C3D20R type elements to model the specimen. Along the length of the model, a section $c=6$ mm was used for the refined mesh in the vicinity of the delamination front. Twenty four elements were used yielding an element length $\Delta a=c/n=0.25$ mm. This mesh size was found suitable during the initial investigation of the DCB specimen described in the previous section.

In Figures 26 to 28 the computed mode I, II and mode III strain energy release rates are plotted versus the normalized width, y/B, of the specimen. Computed strain energy release rates obtained from models using C3D8I, C3D20 and C3D20R elements are in excellent agreement with the values from a previous analysis using continuum based shell elements [23, 29]. As shown in Figure 26, the mode I strain energy release rate is fairly constant in the center part of the specimen progressively dropping towards the edges as previously discussed for the DCB specimen. The model made of C3D8 elements yields results which do not correctly capture the drop of the mode I strain energy release rate towards the edge. The values computed from the model made of C3D8R elements appear excessively high. The mode II strain energy release rate as shown in Figure 27 is fairly constant across almost the entire width of the specimen, peaking in the immediate vicinity of the edges, which was discussed earlier in the section about the ENF specimen. As shown in Figure 28, the mode III contribution is zero in the center of the specimen peaking to about only 8% of G_{II} at the edges. The model made of C3D8 elements yields results which do not correctly capture the mode II and III distribution. The mode II values computed from the model made of

C3D8R elements appear excessively high across the entire width of the specimen. These observations support the results obtained from the study of the UD24 DCB and ENF specimens discussed previously. Models made of C3D8 and C3D8R elements were not investigated any further. Compared to the model made of C3D20 elements the models made of C3D8I elements yield nearly the same results and provide a reduced model size. Therefore this element type was chosen for the following studies.

A shell/3D model of a SLB specimen is shown in Figure 29. The global section was modeled with quadrilateral shell elements S4. The local three-dimensional section was modeled with eight-noded C3D8I type elements. Along the length a refined mesh of length $c=6$ mm with 24 elements was used in the vicinity of the delamination front. As discussed in the study of the DCB and ENF specimens above, the section length, c, was kept constant during the entire investigation. To study the influence of the length of the local zone on computed mixed mode strain energy release rates, the total length of the local zone modeled with solid elements, d, was varied ($d=10$, 15, 20, 25, 30 mm) as shown in Figures 14 (a) to (f).

The computed mode I, II and III strain energy release rate distributions across the width of the specimen are shown in Figures 30 to 32. With increasing length of the local three-dimensional model, d, computed results from the shell/3D model converge to the solution obtained from a full three-dimensional model. For a local three-dimensional model extending to a minimum of about three specimen thicknesses in front and behind the delamination front ($d/2h=6.16$), the results were within 1% of the mode I and II strain energy release rates obtained from computations where the entire specimen had been modeled with solid elements. As shown in Figure 32, the results obtained from all shell/3D models are in excellent agreement with the mode III strain energy release rate obtained from computations where the entire specimen had been modeled with solid elements. For unidirectional layup, however, the mode III contribution is very small. Therefore, the influence of the size of the local three-dimensional model on in plane shear mode II and mode III separation needs to verified for a case where the mode III contribution is more obvious and the mode II contribution is less dominant. This will be discussed in the sections on the ENF and SLB specimens with multidirectional layup.

ANALYSIS OF SPECIMENS WITH A MULTIDIRECTIONAL LAYUP

In general DCB, ENF and mixed mode tests are performed on unidirectionally reinforced laminates, which means that delamination growth occurs at a [0/0] interface and crack propagation is parallel to the fibers. Although this unidirectional layup is desired for standard test methods to characterize fracture toughness, this kind of delamination growth will rarely occur in real structures. Previously, a number of combined experimental and numerical studies on specimens with multidirectional layup have been performed where the critical strain energy release rates of various interfaces were evaluated under mode I, mode II and mixed-mode conditions [14, 15, 23]. In this study, DCB, ENF and SLB specimens with a multidirectional layup were first modeled entirely with solid elements to validate the three-dimensional model and select an appropriate mesh size around the delamination front. For each specimen type, mixed mode strain energy release rate distributions were computed across the width from nonlinear finite element analyses using the virtual crack closure technique. Results were used as reference solutions for comparison with values obtained from the shell/3D technique. The analyses were then repeated using the shell/3D modeling technique to study the feasibility for pure mode I (DCB), mode II (ENF) and mixed mode I/II cases (SLB).

COMPUTATION OF STRAIN ENERGY RELEASE RATES ACROSS A STRAIGHT DELAMINATION FRONT IN A SLB-TYPE SPECIMEN

Previous investigations have shown that care must be exercised in interpreting the values for G_I, G_{II} and G_{III} obtained using the virtual crack closure technique for interfacial delaminations between two orthotropic solids [30, 31]. Mathematical solutions of the near crack tip field indicate that stresses start to oscillate in the immediate vicinity of the tip when crack growth occurs at interfaces between materials with dissimilar properties. In the current investigation, this phenomenon has to be considered as the delamination growth occurs at a +30°/-30° interface. Therefore, the mixed mode SLB specimen was studied first and an appropriate mesh size was determined which was then also used for the models of the D±30 DCB and ENF specimens.

For the investigation of the D±30 SLB specimen, the finite element model shown in Figure 33 was used. The model was made of eight noded ABAQUS® C3D8I elements. It had been shown above that compared to the model made of C3D20 elements the models made of C3D8I yield nearly the same results and provide a reduced model size. Therefore these element types were chosen for this and the following studies. The specimen was divided into a center section of width, f, and a refined edge section of width, e, to capture local edge effects and steep gradients. Section widths and mesh sizes used in the current investigation were taken from a previous study [23]

where the effect of mesh size across the width on computed mixed mode energy release had been investigated. Along the length of the model a refined mesh of length c was used in the vicinity of the delamination front. This section length, c=3.0 mm, was kept constant. The number of elements, n, was varied to study the influence of mesh size on computed mixed mode strain energy release rates.

First, the influence of mesh size was studied. The mesh size equals the length of the elements in the refined section, which is identical to the length of the elements at the delamination tip. As shown in Figure 34, the zone with a constant G_I distribution in the center becomes smaller compared to the UD32 case and the drop towards the edges is more pronounced. The drop is caused by increased anticlastic bending due to the lower values of bending rigidities in the individual arms. The influence of mesh refinement on the mode I strain energy release rate distribution across the width is moderate and only very long elements (n=3, $\Delta a=c/n=1$ mm) need to be avoided. This is confirmed by the mode II and mode III distributions as shown in Figures 35 and 36 where the mode II strain energy release rate is fairly constant across almost the entire width of the specimen and peaks near the edges accompanied by local mode III contribution. Compared to the UD32 layup these peaks become more visible for specimens with the D±30 layup caused by increased anticlastic bending. The distribution of the mixed mode ratio G_I/G_{II} is shown in Figure 37. For the range studied (n=3 up to 48), there is only a small dependence of computed mixed mode ratio on element size $\Delta a=c/n$. Hence, twelve elements were chosen (n=12) in the refined section (c=3 mm). For the delamination in the +30°/-30° ply interface, the element length was therefore chosen to be $\Delta a=c/n=0.25$ mm and this element length was used consistently during the entire investigation.

Second, the computed mode I, II and mode III strain energy release rates as shown in Figures 38 to 40 were compared with values from previous analyses using layered, continuum based shell elements [23, 29]. The good agreement of the results indicates that the model was set up appropriately and the post processing module to compute the strain energy release rate using VCCT operates accurately. For comparison, mixed mode strain energy release rates were computed from models where the local penetration of the cantilever arms at the specimen edge near the delamination front was prevented by contact analysis. The results included in Figure 38 to 40 are in almost exact agreement with results from simple analyses, where the penetration was not prevented. It was therefore chosen not to prevent the penetration and thus avoid the complicated contact analysis for the remainder of this study.

A shell/3D model of a SLB D±30 specimen is shown in Figure 41. The global section was modeled with quadrilateral S4 type shell elements. The local three-dimensional section was modeled with eight-noded C3D8I type elements. Along the length a refined mesh of length c=3 mm with 12 elements was used in the vicinity of the delamination front. As discussed earlier, the

section length, c, was kept constant during the entire investigation. To study the influence of the length of the local zone on computed mixed mode strain energy release rates, the total length of the local zone modeled with solid elements, d, was varied (d=10, 15, 20, 25, 30 mm) as shown in Figures 14 (a) to (f).

The computed mode I, II and III strain energy release rate distributions across the width of the specimen are shown in Figures 42 to 44. With increasing length of the local three-dimensional model, d, computed results from the shell/3D model converge to the solution obtained from a full three-dimensional model. For a local three-dimensional model extending to a minimum of about three specimen thicknesses in front and behind the delamination front (d/2h=6.16), the results were within 1% of the mode I and II strain energy release rates obtained from computations where the entire specimen had been modeled with solid elements. As shown in Figure 43, the computed mode II contribution is constant across the center of the specimen, with larger values near the edges compared to the results obtained for the UD32 layup. For the D±30 layup also a considerable amount of mode III is present due to the increased anticlastic bending for this layup as shown in Figure 44. As before, the results from the shell/3D technique were within 1% of the reference solution obtained from computations where the entire specimen had been modeled with solid elements. These results indicate that the shell/3D technique is capable of accurately simulating the increased anticlastic bending effect due to the lower values of bending rigidities in the individual arms for this layup which causes the mode II and III strain energy release rate to be higher towards the free edges.

COMPUTATION OF STRAIN ENERGY RELEASE RATES ACROSS A STRAIGHT DELAMINATION FRONT IN A DCB SPECIMEN

For this investigation, the entire width B of the DCB specimen was modeled as shown in Figure 45. The eight noded brick element ABAQUS® C3D8I was used for the simulation. Along the length of the model, a refined mesh of length c= 3 mm was used in the vicinity of the delamination front. The refined section was divided into n= 12 number of elements, which was found to yield a reasonable mesh $\Delta a=c/n=0.25$ mm as discussed for the SLB specimen in the previous section. The specimen was divided into a center section of width, f, and a refined edge section of width, e, to capture local edge effects and steep gradients. Section widths and mesh sizes used in the current investigation were taken from a previous study [23] where the effect of mesh size across the width on computed mixed mode energy release had been investigated.

The computed mode I strain energy release rate distribution as shown in Figure 46 was compared with values from a previous analysis using layered, continuum based shell elements [23, 29]. The mode I strain energy release rate is fairly constant in the center part of the specimen

progressively dropping towards the edges causing the straight front to grow into a curved front. Basically the distributions are similar to those computed for the UD24-layup. For specimens with multidirectional layup the zone with a constant mode I distribution in the center becomes smaller and the drop towards the edges is more pronounced. This phenomenon is caused by the smaller bending rigidities in the individual arms of the specimens and has been the subject of detailed experimental and analytical investigations [14, 23]. As expected, the mode II and mode III strain energy release rates are computed to be nearly zero and hence are not shown. The good agreement of the results indicates that the model was set up appropriately and the post processing module to compute the strain energy release rate using VCCT operates accurately. The computed mode I strain energy release rate obtained from a model where the penetration of the cantilever arms was prevented near the delamination front using contact analysis was also included in Figure 46 for comparison. The distribution shown is in almost exact agreement with the distribution obtained from a simple analysis, where the penetration was not prevented. It was therefore chosen not to enforce contact and thus avoid the complicated contact analysis for the remainder of this study.

A shell/3D model of a DCB specimen is shown in Figure 47. The global section was modeled with S4 type shell elements. The local three-dimensional section was modeled with C3D8I type solid elements. Along the length a refined mesh of length $c=3$ mm with 12 elements was used in the vicinity of the delamination front, which is identical to the refined mesh used for the full three-dimensional model discussed above. This section length, c, was kept constant during the entire investigation. To study the influence of the length of the local zone on computed mixed mode strain energy release rates, the total length of the local zone modeled with solid elements, d, was varied ($d=10$, 15, 20, 25, 30 mm) as shown in Figures 14 (a) to (f).

The computed strain energy release rate distributions across the normalized width of the specimen are shown in Figure 48. As expected, the mode II and mode III strain energy release rates are computed to be nearly zero and hence are not shown. With increasing length of the local three-dimensional model, d, computed results from the shell/3D model converge to the solution obtained from a full three-dimensional model. For a local three-dimensional model extending to a minimum of about three specimen thicknesses in front and behind the delamination front ($d/2h=6.16$), the results were within 1% of the mode I strain energy release rates obtained from computations where the entire specimen had been modeled with solid elements. As shown in Figure 48, the zone with a constant G_I distribution in the center becomes smaller compared to the UD24 case and the drop towards the edges is more pronounced. The drop is caused by increased anticlastic bending due to the lower values of bending rigidities in the individual arms for this layup. The good agreement with results obtained from full three-dimensional models suggests that these effects are accurately simulated by the shell/3D model.

COMPUTATION OF STRAIN ENERGY RELEASE RATES ACROSS A STRAIGHT DELAMINATION FRONT IN AN ENF SPECIMEN

For the mode II ENF tests, references 14 and 23 show that the mode II strain energy release rate is fairly constant across almost the entire width of the specimen, peaking in the immediate vicinity of the edges and accompanied by local mode III contributions in the same areas. These peaks become more visible for specimens with multidirectional layup [14, 23]. Therefore an ENF specimen with D±30 layup was selected for this study to verify the accuracy of the shell/3D technique in simulating this local mixed mode case near the edge of the specimen. For this investigation, the entire width B of the ENF specimen was modeled as shown in Figure 49. Along the length of the model a refined mesh of length $c = 3$ mm was used in the vicinity of the delamination front. The refined section was divided into $n = 12$ number of elements, which was found to yield a reasonable mesh with element size $\Delta a = c/n = 0.25$ mm as discussed for the SLB specimen in the previous section. The specimen was divided into a center section of width f and a refined edge section of width e to capture local edge effects and steep gradients. Section widths and mesh sizes used in the current investigation were taken from a previous study [23] where the effect of mesh size across the width on computed mixed mode energy release had been investigated. Interpenetration of the cantilever arms was first prevented by using contact elements [24]. Earlier studies [23] showed, that penetration of the arms could be prevented by introducing multi point constraints in the plane of delamination only along a string of nodes above the left support as schematically shown in Figure 18. The use of multi point constraints appears advantageous as less modeling effort is required and a computationally expensive contact analysis is avoided. Therefore, the influence of the multi point constraint technique on the computed mode II and mode III strain energy release rates was also studied.

In Figures 50 and 51 the computed mode II and mode III strain energy release rates are plotted versus the normalized width, y/B, of the specimen. The results are in good agreement with the distribution from a previous analysis using layered, continuum based shell elements [23, 29]. The mode II strain energy release rate is fairly constant across almost the entire width of the specimen, peaking near the edges and accompanied by local mode III contributions in the same area. Compared to the UD32 layup these peaks become more visible for specimens with D±30 layup caused by increased anticlastic bending effect due to the lower values of bending rigidities in the individual arms for this layup. The computed G_I values are nearly zero and therefore are not shown. Computed mode II and mode III strain energy release rates obtained from models where the penetration of the cantilever arms was prevented by multi point constraints were included in Figures 50 and 51. The results shown are in almost exact agreement with the values obtained from a contact analysis. Therefore, the technique using the multi point constraints to avoid penetration was used for the remainder of this study.

A shell/3D model of an ENF specimen is shown in Figure 52. The global section was modeled with quadrilateral S4 type shell elements. The local three-dimensional section was modeled with eight-noded C3D8I type elements. Along the length a refined mesh of length c=3 mm with 12 elements was used in the vicinity of the delamination front. As discussed in the study of the DCB specimen above, the section length, c, was kept constant during the entire investigation. To study the influence of the length of the local zone on computed mixed mode strain energy release rates, the total length of the local zone modeled with solid elements, d, was varied (d=10, 15, 20, 25, 30 mm) as shown in Figures 14 (a) to (f).

The computed mode II and III strain energy release rate distributions across the normalized width of the specimen are shown in Figures 53 and 54. As expected, the mode I strain energy release rates is computed to be nearly zero and hence is not shown. With increasing length of the local three-dimensional model, d, computed results from the shell/3D model converge to the solution obtained from a full three-dimensional model. For a local three-dimensional model extending to a minimum of about three specimen thicknesses in front and behind the delamination front (d/2h=6.16), the results were within 1% of the mode II and III strain energy release rates obtained from computations where the entire specimen had been modeled with solid elements. As shown in Figure 53, the computed mode II contribution is constant across the center of the specimen, with larger values near the edges compared to the results obtained for the UD24 layup. For the D±30 layup also a considerable amount of mode III is present due to the increased anticlastic bending for this layup as shown in Figure 53. These results indicate that the shell/3D technique is capable of accurately simulating the increased anticlastic bending effect due to the lower values of bending rigidities in the individual arms for this layup which causes the mode II and III strain energy release rate to be higher towards the free edges.

CONCLUDING REMARKS

A shell/3D modeling technique was presented for the analysis of composite laminates with delaminations. The individual mode and total strain energy release rates along the delamination front were evaluated. In this analysis, a local solid finite element model was used only in the immediate vicinity of the delamination front. The goal was to combine the accuracy of the full three-dimensional solution with the computational efficiency of a plate or shell finite element model. Multi-point constraints provided a kinematically compatible interface between the local three-dimensional model and the global structural model which was meshed with shell finite elements.

For DCB, ENF, and SLB specimens, mixed mode strain energy release rate distributions were computed across the width from nonlinear finite element analyses using the virtual crack closure technique. This served to study the feasibility of the proposed shell/3D modeling technique for the pure mode I case (DCB), mode II case (ENF) and a mixed mode I/II case (SLB). Specimens with a unidirectional layup, for which the delamination is located between two 0° plies, as well as a multidirectional layup were simulated. First, all three specimens were modeled entirely with solid elements to validate the three-dimensional model, to select suitable element types and appropriate mesh size around the delamination front, and to check the need for contact analysis to prevent the interpenetration of the delaminated surfaces. Results were used as reference solutions for comparison with values obtained from the shell/3D technique. The geometrically nonlinear solution option of the ABAQUS® finite element code was used for the entire investigation. For each specimen, mixed mode strain energy release rate distributions were computed across the width from nonlinear finite element analyses using the virtual crack closure technique.

The computation of mixed mode strain energy release rates is most critical for interfacial delaminations between two different orthotropic solids. Therefore, general recommendations for the selection of element types and appropriate mesh size around the delamination front may be taken from the results obtained from the specimens where the delamination is located between two non-zero plies. Compared to earlier studies, the models made of solid twenty-noded hexahedral elements (ABAQUS® types C3D20 and C3D20R with reduced integration) and solid eight-noded incompatible mode elements (ABAQUS®, type C3D8I) yield excellent results. The mesh refinement study showed that only a section of about 1 mm on either side of the delamination front needs to be refined. The influence of mesh size on the computed mixed mode ratio was negligible for elements lengths between $\Delta a = 0.5$ mm (four ply thicknesses) and $\Delta a = 0.0625$ mm (half a ply thickness). For the ENF specimen, it was found that instead of a complicated contact analysis, penetration of the arms could be prevented by introducing multi-point constraints between the delaminated surfaces just above the left support without compromising the accuracy of the

computed results. For the DCB and SLB specimens the influence of interpenetration was negligible.

For the current investigation, two shell/3D combinations were studied: eight noded solid elements in the local section combined with four noded shell elements in the global section of the model and twenty-noded solid elements in the local section combined with eight-noded shell elements in the global section. The shell elements were connected to the local three-dimensional model using multi-point constraints to enforce appropriate translations and rotations. An overview of all element types, shell/3D combinations and mesh refinements investigated is given in Table 3 for all specimen types.

Finite element analyses showed that the accuracy achieved depends on the size of the local area. With increasing size of the local three-dimensional model, the computed results converged towards the strain energy release rates obtained from full three-dimensional finite element analysis for all specimens, layups and element types simulated. The results were in good agreement with the reference solution once the local zone was extended to about three times the specimen thickness in front and behind the delamination front.

For large composite structures the shell/3D modeling technique offers great potential for reducing the model size because only a relatively small section in the vicinity of the delamination front needs to modeled with solid elements. A significant reduction in model size can be expected compared to a full three-dimensional model. In the current investigation, the application of the shell/3D technique reduced the number of degrees of freedom by about 35% compared to a full three-dimensional model for all three specimen types. Existing plate models may be modified to shell/3D models, which is a considerable advantage compared to the creation of an entirely new three-dimensional finite element model.

REFERENCES

[1] O'Brien, T.K., "Characterization of Delamination Onset and Growth in a Composite Laminate," *Damage in Composite Materials, ASTM STP 775*, 1982, pp. 140-167.

[2] O'Brien, T.K. "Interlaminar fracture toughness: the long and winding road to standardization," *Composites Part B.*, Vol. 29B, 1998, pp. 57-62.

[3] Martin, R. H., "Incorporating Interlaminar Fracture Mechanics Into Design," International Conference on Designing Cost-Effective Composites, IMechE Conference Transactions, London, 15-16 September, 1998, pp. 83-92.

[4] Rybicki, E.F. and Kanninen, M.F., "A Finite Element Calculation of Stress Intensity Factors by a Modified Crack Closure Integral," *Eng. Fracture Mech.*, 9, 1977, pp. 931-938.

[5] Raju, I.S., "Calculation Of Strain-Energy Release Rates With Higher Order And Singular Finite Elements," *Eng. Fracture Mech.*, 28, 1987, pp. 251-274.

[6] Buchholz, F.G., Grebner, H., Dreyer, K.H. and Krome, H., "2D- and 3D-Applications of the Improved and Generalized Modified Crack Closure Integral Method," *Computational Mechanics '88*, Atluri, S.N. and Yagawa, G., eds., Springer Verlag, 1988.

[7] Raju, I.S., Sistla, R. and Krishnamurthy, T., "Fracture Mechanics Analysis For Skin-Stiffener Debonding," *Eng. Fracture Mech.*, 54, 1996, pp. 371-385.

[8] Raju, I.S., Shivakumar, K.N. and Crews, J.H., "Three-dimensional elastic analysis of a composite double cantilever beam specimen," *AIAA J.*, 26, 1988, pp. 1493-1498.

[9] O'Brien, T.K. and Martin, R.H., "Round Robin Testing for Mode I Interlaminar Fracture Toughness of Composite Materials," *J. of Composite Technology and Research.*, 1993, pp. 269-281.

[10] O'Brien, T.K. "Composite Interlaminar Shear Fracture Toughness, G_{IIc}: Shear Measurement or Sheer Myth ?," *Composite Materials: Fatigue and Fracture, Seventh Volume, ASTM STP 1330*, 1998, pp. 3-18.

[11] Reeder, J.R and Crews, J.H., "Redesign of the Mixed-Mode Bending Delamination Test to Reduce Nonlinear Effects," *J. of Composite Technology and Research.*, 1992, pp. 12-19.

[12] Reeder, J.R., "A Bilinear Failure Criterion for Mixed-Mode Delamination," *Composite Materials: Testing and Design, Eleventh Volume*, ASTM STP 1206, 1993, pp. 303-322.

[13] Krüger, R., König, M. and Schneider, T., "Computation of Local Energy Release Rates Along Straight and Curved Delamination Fronts of Unidirectionally Laminated DCB- and ENF - Specimens," AIAA-93-1457-CP, *Proc. 34th AIAA/ASME/ASCE/AHS/ASC SSDM Conference, La Jolla, CA*, 1993, pp. 1332-1342.

[14] Davidson, B.D., Krüger, R. and König, M., "Effect of Stacking Sequence on Energy Release Rate Distributions in Multidirectional DCB and ENF specimens," *Engineering*

Fracture Mechanics, 1996, 55(4), pp. 557-569.

[15] Davidson, B.D., Krüger, R. and König, M., "Three Dimensional Analysis of Center Delaminated Unidirectional and Multidirectional Single Leg Bending Specimens," *Composites Science and Technology*, 1995, 54(4), pp. 385-394.

[16] Salpekar, S.A. and O'Brien, T.K., "Combined Effect of Matrix Cracking and Free Edge on Delamination," *Composite Materials: Fatigue and Fracture, Third Volume, ASTM STP 1110*, 1991, pp. 287-311.

[17] Whitcomb, J.D, "Three-Dimensional Analysis of a Postbuckled Embedded Delamination," *J. Composite Mat.,* Vol. 23, 1989, pp. 862-889.

[18] Krüger, R., Rinderknecht, S., Hänsel, C., and König, M., "Computational Structural Analysis and Testing: An Approach to Understand Delamination Growth," *Fracture of Composites*, E.A. Armanios, ed., Key Eng. Mat., Vols. 120-121, Transtec Publ. Ltd.,1996, pp. 181-202.

[19] Glaessgen, E.H., Riddell, W.T., and Raju, I.S., "Effect of Shear Deformation and Continuity on Delamination Modeling with Plate Elements," *Proceedings of the AIAA/ASME/ASCE/AHS/ASC 39th Structures, Structural Dynamics and Materials Conference*, AIAA-98-2023-CP, 1998.

[20] Krüger, R., Rinderknecht, S., and König, M., "Two- and Three-Dimensional Finite Element Analyses of Crack Fronts in a Multidirectional Composite ENF Specimen," ISD-Report No. 97/1, Institute for Statics and Dynamics of Aerospace Structures, University of Stuttgart, 1997.

[21] Krueger, R., Cvitkovich, M.K., O'Brien, T.K. and Minguet, P.J., "Testing and Analysis of Composite Skin/Stringer Debonding Under Multi-Axial Loading," NASA TM-1999-209097, February 1999.

[22] Davidson, B.D., Krüger, R. and König, M., "Three Dimensional Analysis and Resulting Design Recommendations for Unidirectional and Multidirectional End-Notched Flexure Tests", *J. Compos. Mater.*, Vol. 29, 1995, pp. 2108-2133.

[23] Krüger, R., "Three Dimensional Finite Element Analysis of Multidirectional Composite DCB, SLB and ENF Specimens," ISD-Report No. 94/2, Institute for Statics and Dynamics of Aerospace Structures, University of Stuttgart, 1994.

[24] ABAQUS/Standard, "User's Manual, Volume II," Version 5.6, 1996.

[25] Tsai, S.W., *Theory of Composite Design*, Think Composites, ISBN 0-9618090-3-5, pp. 4–6,7–3, 1992.

[26] Dávila, C. G., "Solid-To-Shell Transition Elements for the Computation of Interlaminar Stresses", *Computing Systems in Engineering*, Vol. 5, No. 2, 1994, pp. 193-202.

[27] Crews, J. H., Shivakumar, K. N., and Raju, I. S., "Strain energy release rate distribution

for double cantilever beam specimens," *AIAA J.*, Vol. 29, 1991, pp. 1686-1691.

[28] Davidson, B. D., "An analytical investigation of delamination front curvature in double cantilever beam specimens," *J. Compos. Mater.*, Vol. 24, 1990, pp. 1124-1137.

[29] Parisch, H., "A Continuum-Based Shell Theory For Nonlinear Applications," *Int. J. Num. Meth. Eng.*, 35, 1995, pp. 1855-1883.

[30] Raju, I. S., Crews, J.H., and Aminpour, M.A., "Convergence of Strain Energy Release Rate Components for Edge-Delaminated Composite Laminates," *Eng. Fracture Mech.*, 30, 1988, pp. 383-396.

[31] Sun, C. T. and Manoharan, M. G., "Strain Energy Release Rates of an Interfacial Crack Between Two Orthotropic Solids," *J. Compos. Mater.*, Vol. 23, May 1989, pp. 460-478.

TABLES

TABLE 1. MATERIAL PROPERTIES.

T300/1076 Unidirectional Graphite/Epoxy Prepreg [16]		
E_{11} = 139.4 GPa	E_{22} = 10.16 GPa	E_{33} = 10.16 GPa
ν_{12} = 0.30	ν_{13} = 0.30	ν_{23} = 0.436
G_{12} = 4.6 GPa	G_{13} = 4.6 GPa	G_{23} = 3.54 GPa
C12K/R6376 Unidirectional Graphite/Epoxy Prepreg [16]		
E_{11} = 146.9 GPa	E_{22} = 10.6 GPa	E_{33} = 10.6 GPa
ν_{12} = 0.33	ν_{13} = 0.33	ν_{23} = 0.33
G_{12} = 5.45 GPa	G_{13} = 5.45 GPa	G_{23} = 3.99 GPa

TABLE 2. STACKING SEQUENCE.

Layup-ID	Stacking Sequence	Material
UD24	$[0]_{24}$	T300/1076
UD32	$[0]_{32}$	C12K/R6376
D±30	$[\pm 30/0/-30/0/30/0_4/30/0/-30/0/-30/30/_{\uparrow}\text{-}30/30/30/0/30/0/-30/0_4/-30/0/30/0/\pm 30]$	C12K/R6376

TABLE 3. OVERVIEW OF FINITE ELEMENT ANALYSES.

	DCB UD24	ENF UD24	SLB UD32	DCB D±30	ENF D±30	SLB D±30	Remarks
element type[1]							C3D8I, C3D20 and C3D20R elements yielded almost identical results.
C3D8	+	+	+				
C3D8I	+	+	+				C3D8I was found to be computationally most efficient
C3D8R	+	+	+				
C3D20	+	+	+				
C3D20R	+	+	+				
element length[2]							The influence of mesh size on the computed mixed mode ratio was negligible for elements lengths between $\Delta a = 0.5$ mm (four ply thicknesses) and $\Delta a = 0.0625$ mm (half a ply thickness).Only very long elements ($\Delta a = 5$ mm) need to be avoided.
5 mm	+						
2 mm	+						
1 mm	+					+	
0.5 mm	+					+	
0.25 mm	+					+	
0.125 mm						+	
0.0625 mm						+	
section length c[3]							The mesh refinement study showed that only a section of about 1 mm on either side of the delamination front needs to be refined ($c = 2.0$ mm).
1 mm	+						
2 mm	+						
5 mm	+						
10 mm	+						
15 mm	+						
20 mm	+						
section length d[4]							Computed strain energy release rates were in good agreement with the reference solution once the local zone was extended to about three times the specimen thickness in front and behind the delamination front.
5 mm	+[5]	+	+	+	+	+	
10 mm	+[5]	+	+	+	+	+	
15 mm	+[5]	+	+	+	+	+	
20 mm	+[5]	+	+	+	+	+	
25 mm	+[5]	+	+	+	+	+	
30 mm	+[5]	+	+	+	+	+	
Contact analysis		+			+		MPCs more efficient
				+		+	Contact negligible

[1] for DCB and ENF specimen $c = 10$ mm, $n = 20$; for SLB specimen $c = 6$ mm, $n = 24$; C3D8I elements used

[2] the section length, c, was kept constant and the number of elements, n, was varied; $c = 10$ mm for DCB specimen, $c = 3$ mm for SLB specimen; C3D8I elements used

[3] the section length, c, was varied as shown; n was modified to keep a constant element length $c/n = 0.5$ mm; C3D8I elements used

[4] S4 type shell elements combined with C3D8I solid elements

[5] for DCB-UD24,additionally, a combination of S8R type shell elements with C3D20R solid elements was studied

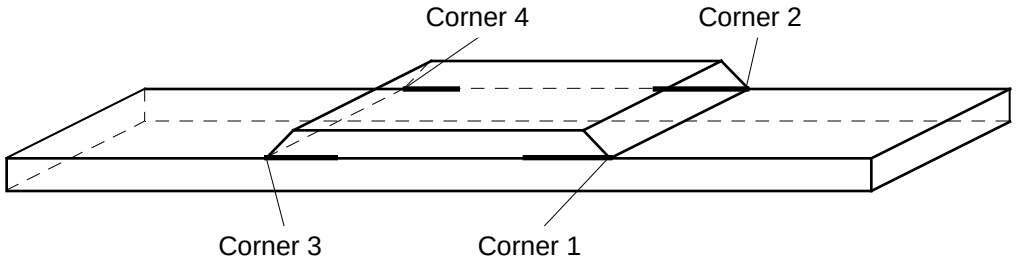

(a) Specimen with crack locations.

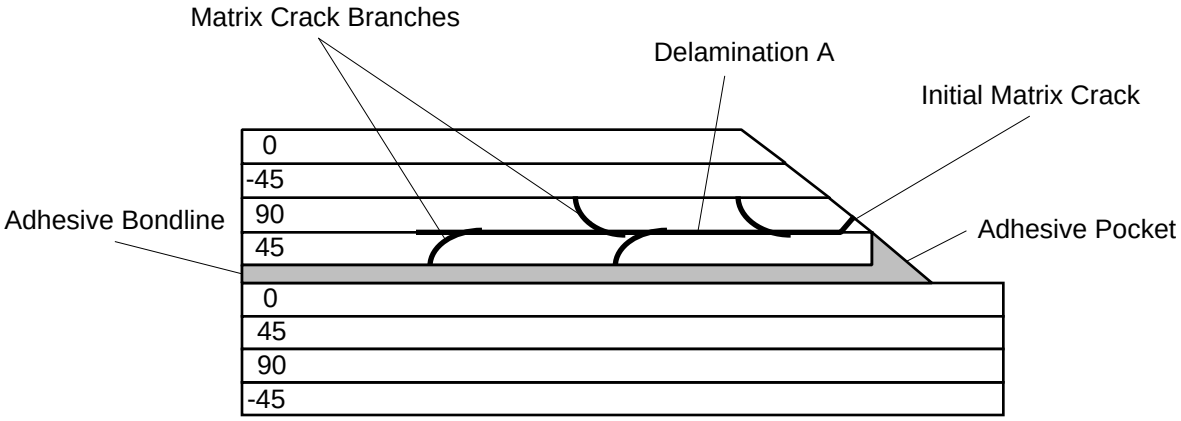

(b) Corners 1 and 4

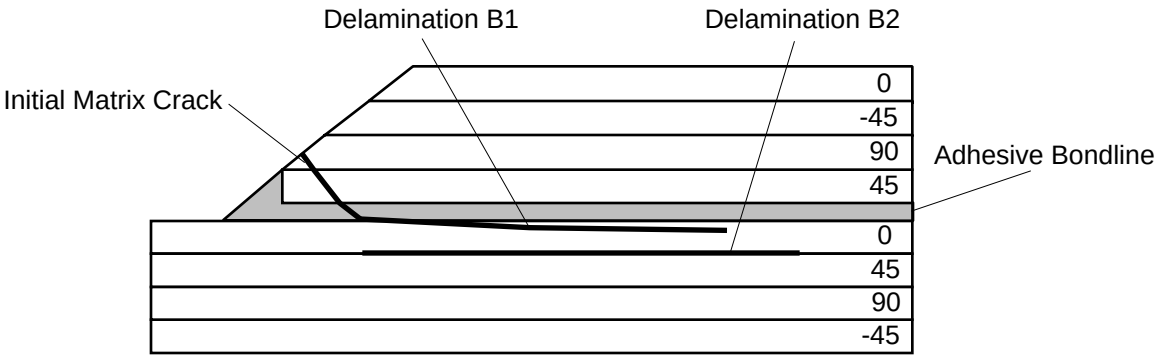

(c) Corners 2 and 3

Figure 1. Typical damage patterns observed in skin/stringer specimens [21]

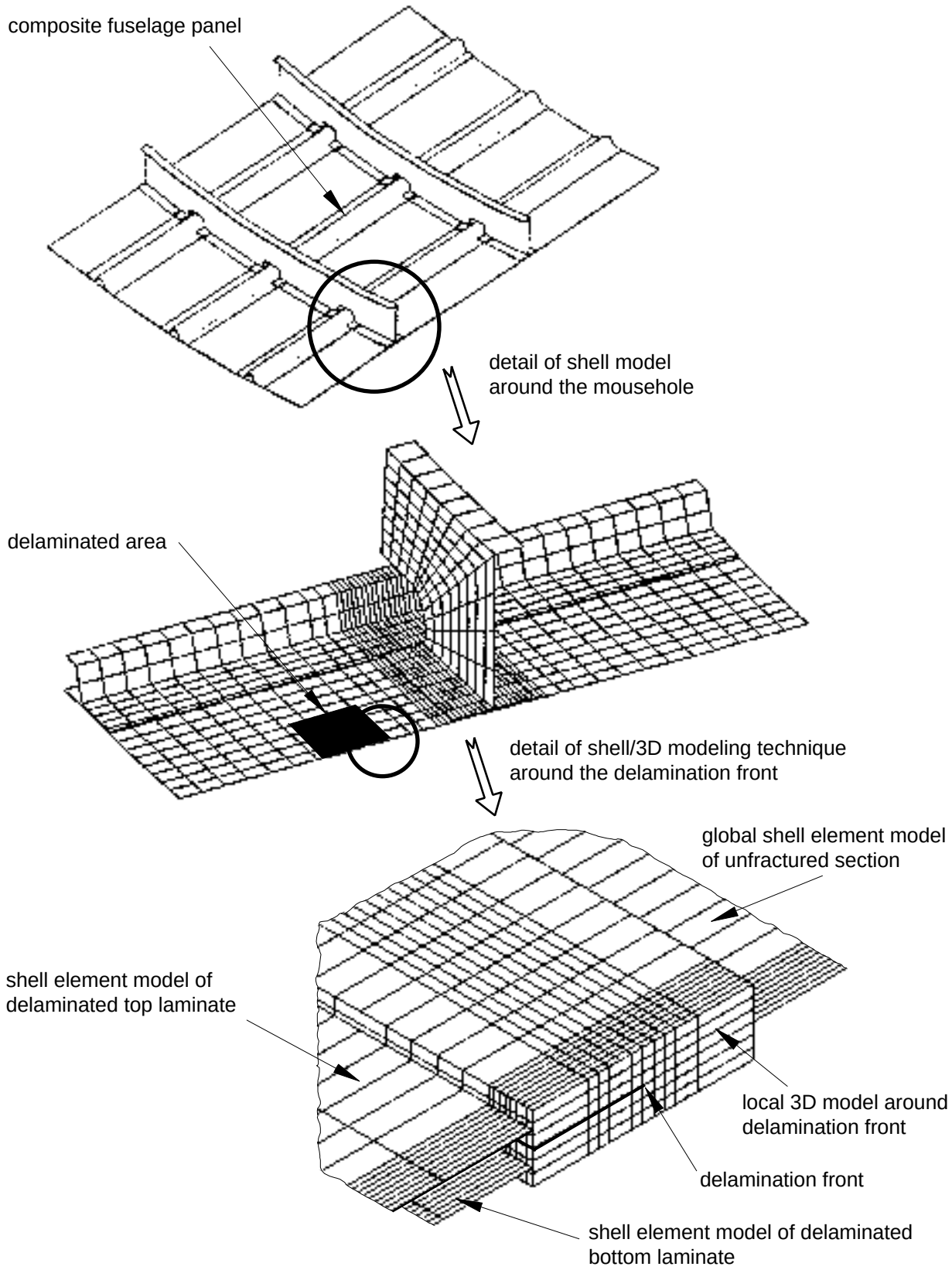

Figure 2. Application of shell/3D modeling technique to large built-up structures.

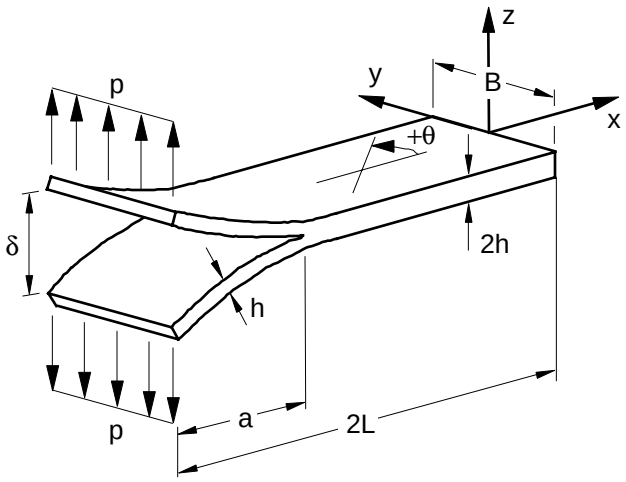

	layup UD24	layup D±30
B	25.0 mm	25.4 mm
2h	3.0 mm	4.06 mm
2L	150.0 mm	150.0 mm
a	111.5 mm	57.2 mm
P	12.66 N	10.0 N

(a) **D**ouble **C**antilever **B**eam Specimen (DCB)

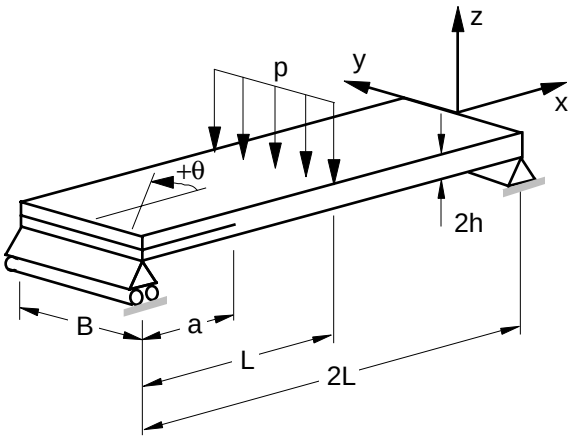

	layup UD24	layup D±30
B	25.0 mm	25.5 mm
2h	3.0 mm	4.06 mm
2L	150.0 mm	127.0 mm
a	30.0 mm	31.8 mm
P	503.0 N	100.0 N

(b) **E**nd **N**otched **F**lexure Specimen (ENF)

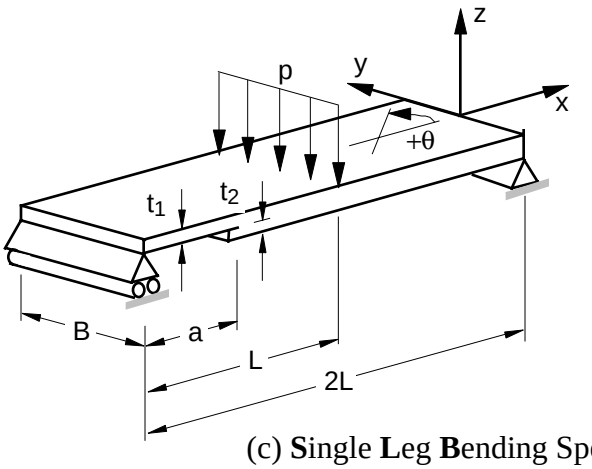

	layup UD32	layup D±30
B	25.0 mm	25.4 mm
t_1	2.03 mm	2.03 mm
t_2	2.03 mm	2.03 mm
2L	177.8 mm	177.8 mm
a	34.3 mm	34.3 mm
P	100.0 N	100.0 N

(c) **S**ingle **L**eg **B**ending Specimen (SLB)

Figure 3. Specimen configurations.

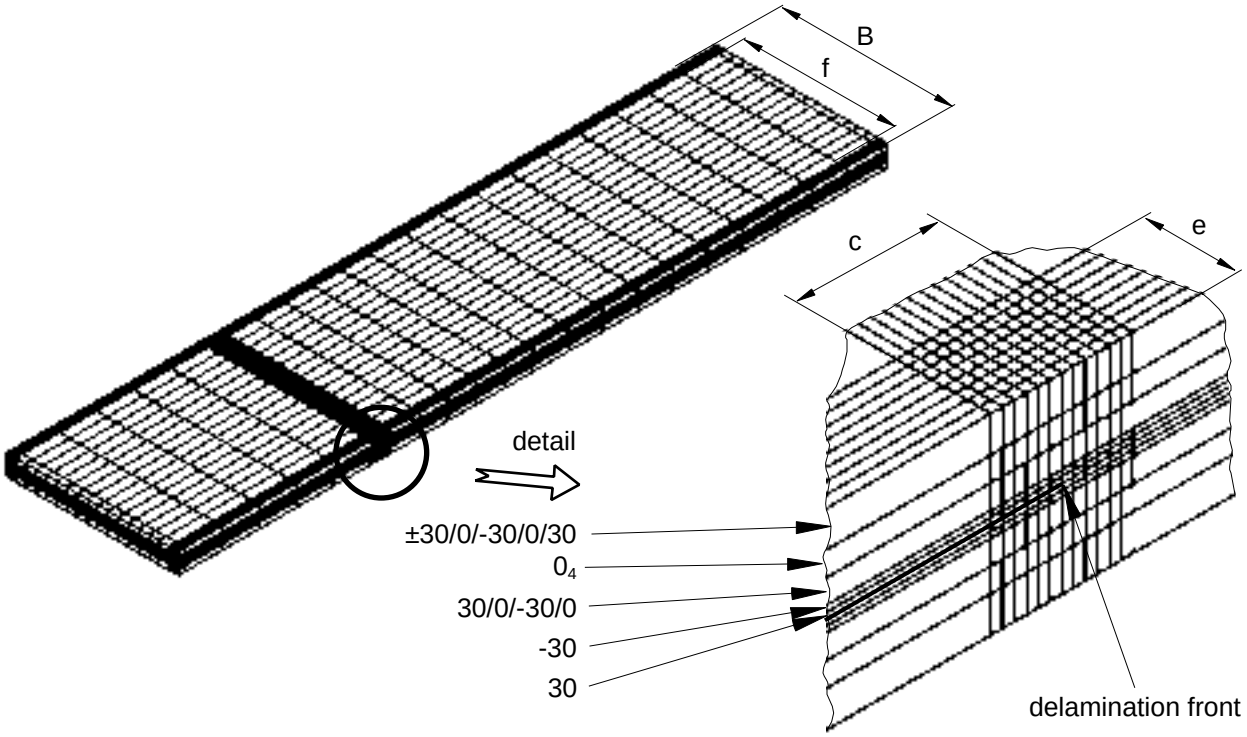

(a) Full three dimensional FE model of specimen with D±30 layup
and detail around delamination front

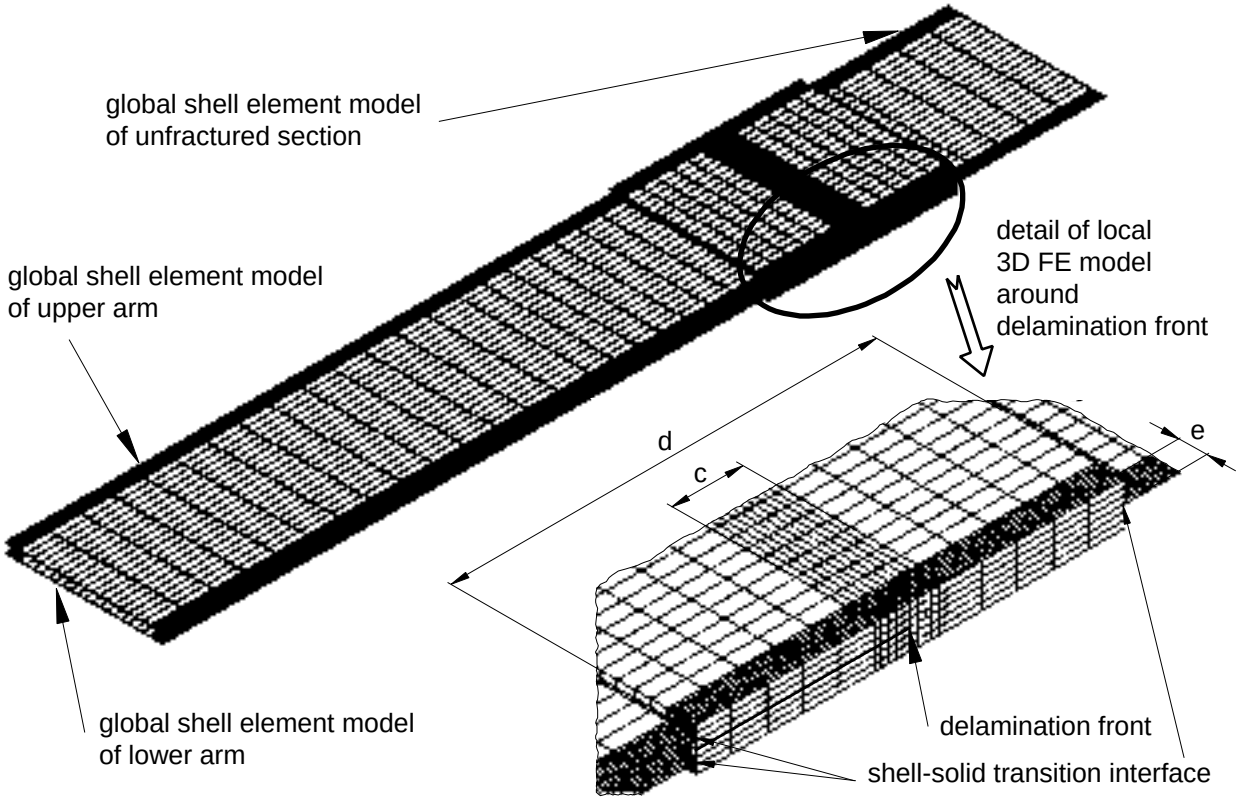

(b) Shell/3D FE model of specimen with UD24 or UD32 layup
and detail around delamination front

Figure 4. Finite element models

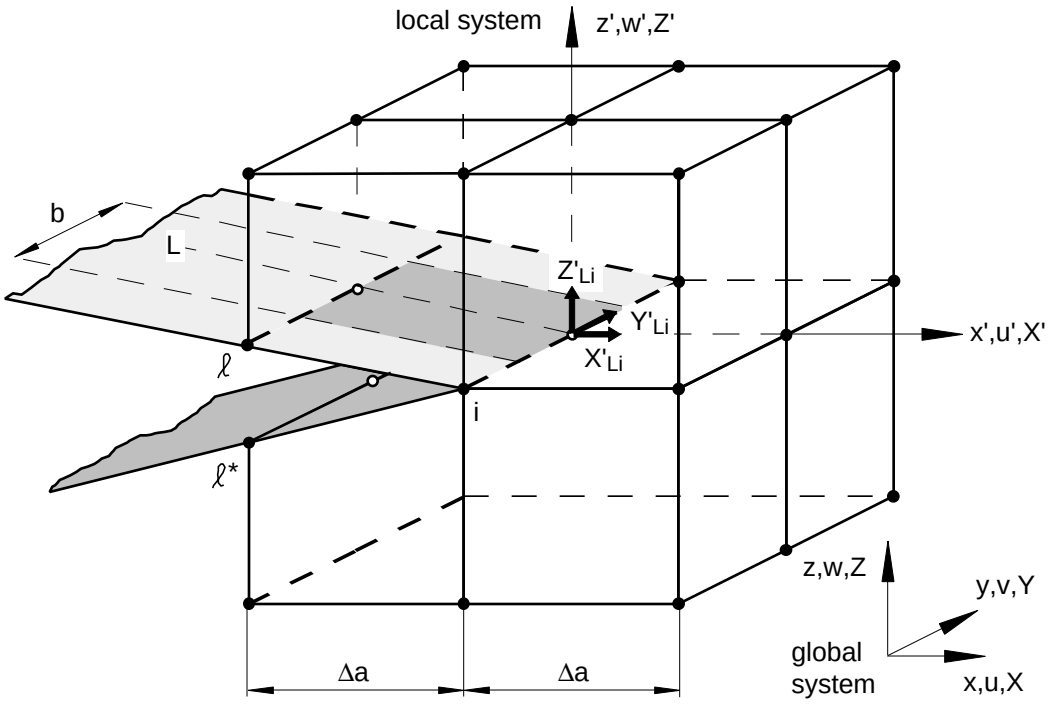

(a) 3D view

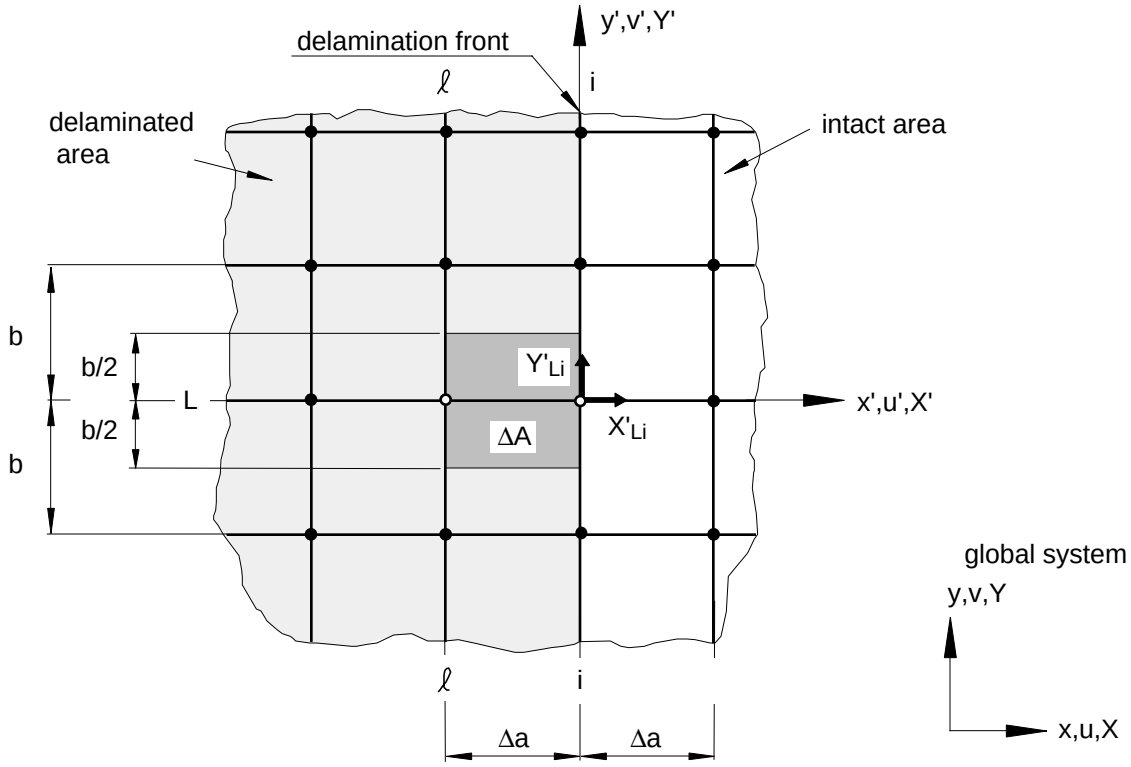

(b) Top view

Figure 5. Virtual Crack Closure Technique for eight noded elements.

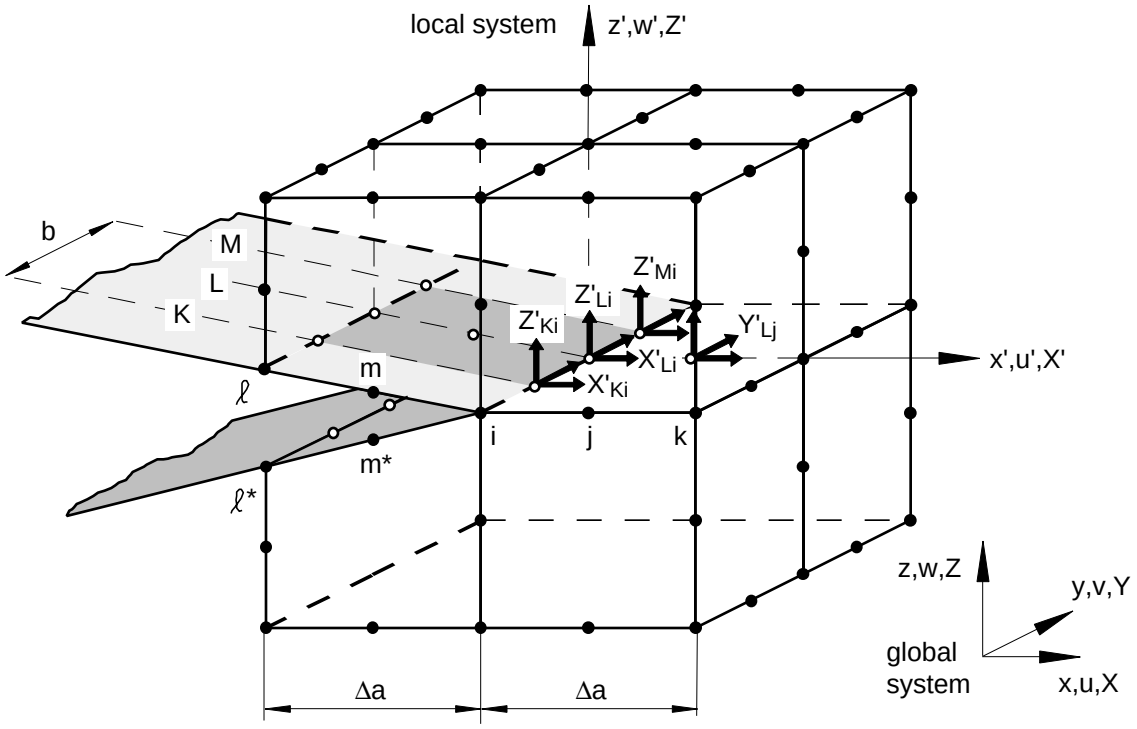

(a) 3D view

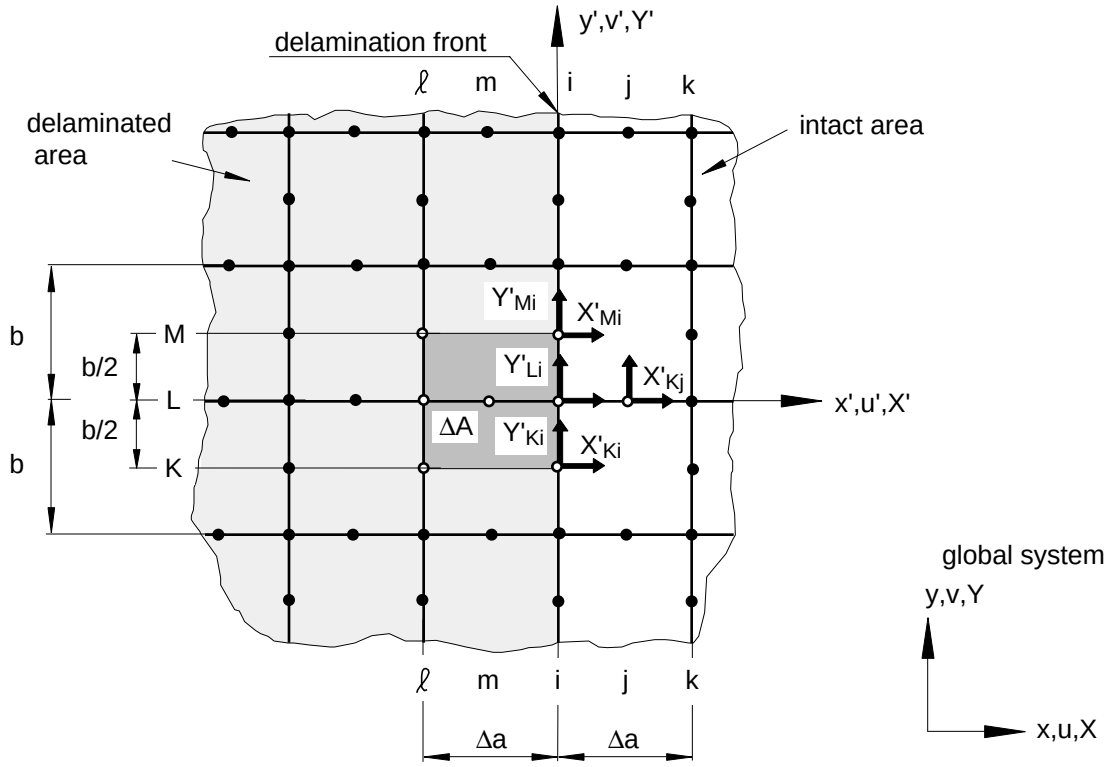

(b) Top view

Figure 6. Virtual Crack Closure Technique for corner nodes in twenty noded elements.

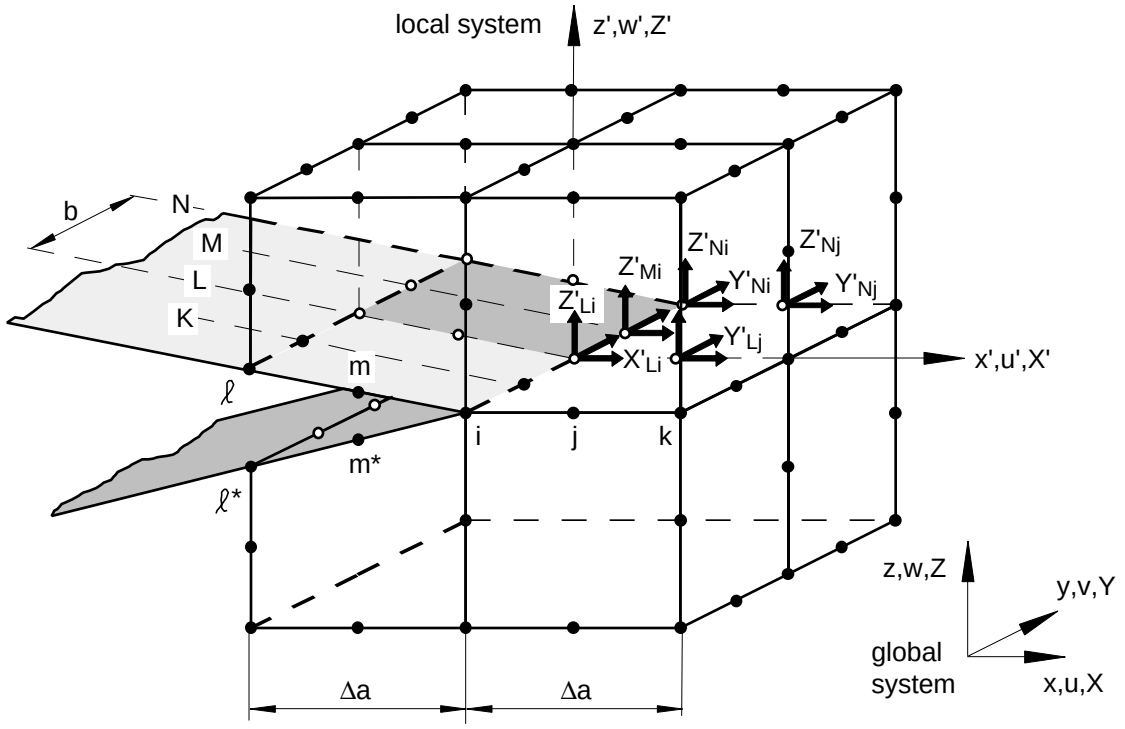

(a) 3D view

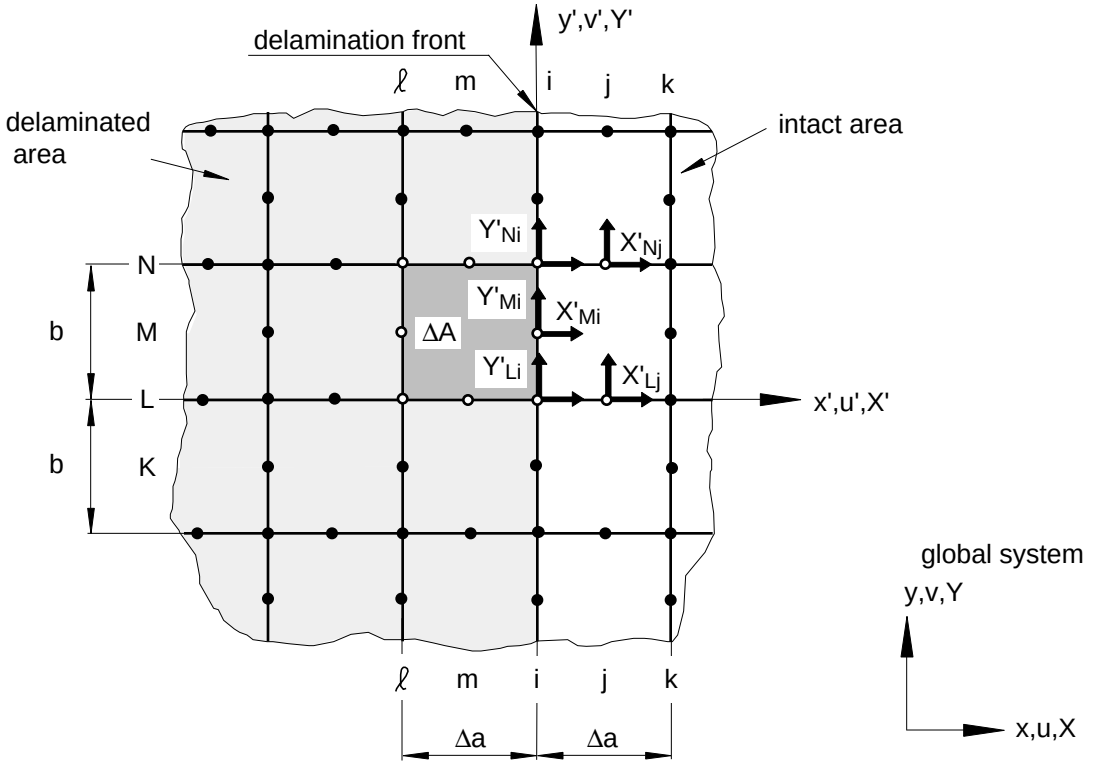

(b) Top view

Figure 7. Virtual Crack Closure Technique for midside nodes in twenty noded elements.

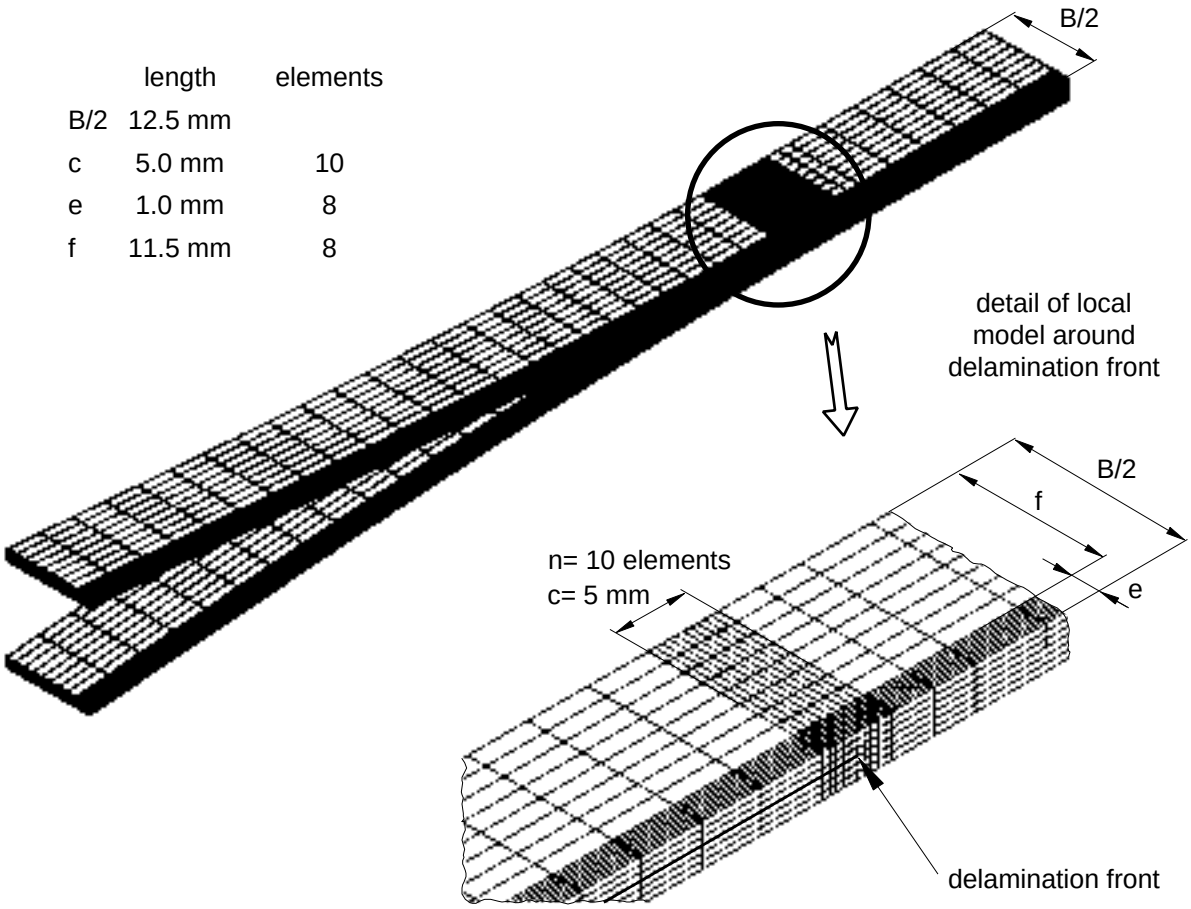

(a) FE model and detail around delamination front (c= 5 mm, n=10)

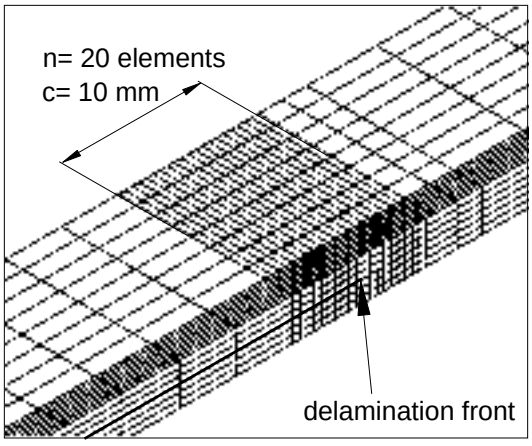

(b) Detail around delamination front (c= 10 mm, n=20)

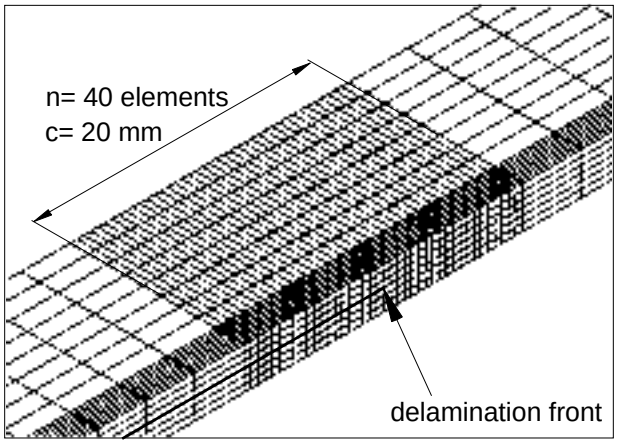

(c) Detail around delamination front (c=20 mm, n=40)

Figure 8. Finite element model of a DCB specimen with UD24 layup

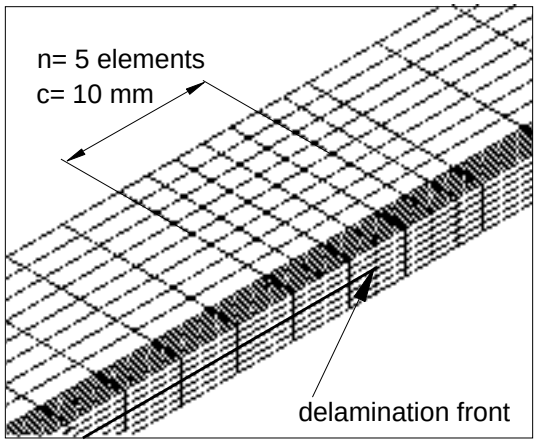

(a) Detail around delamination front (c=10 mm, n=5)

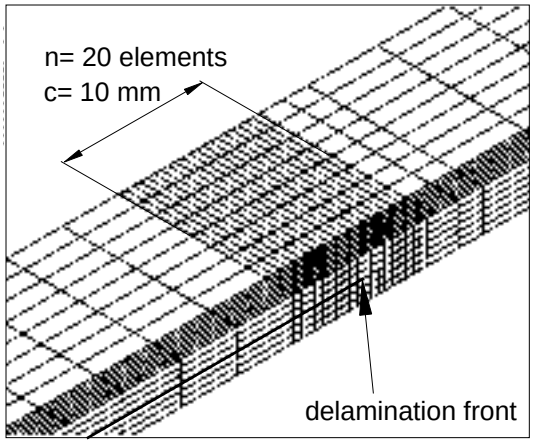

(b) Detail around delamination front (c= 10 mm, n=20)

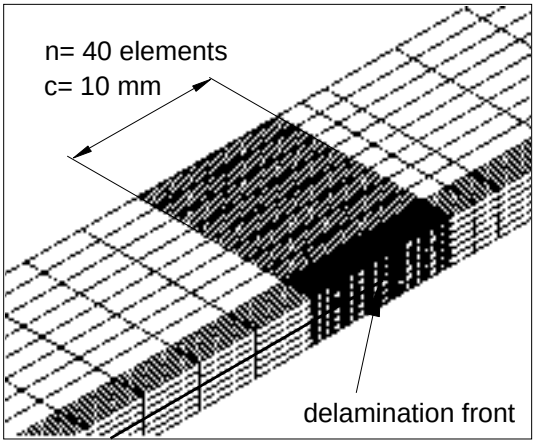

(c) Detail around delamination front (c=10 mm, n=40)

Figure 9. Mesh detail around delamination front

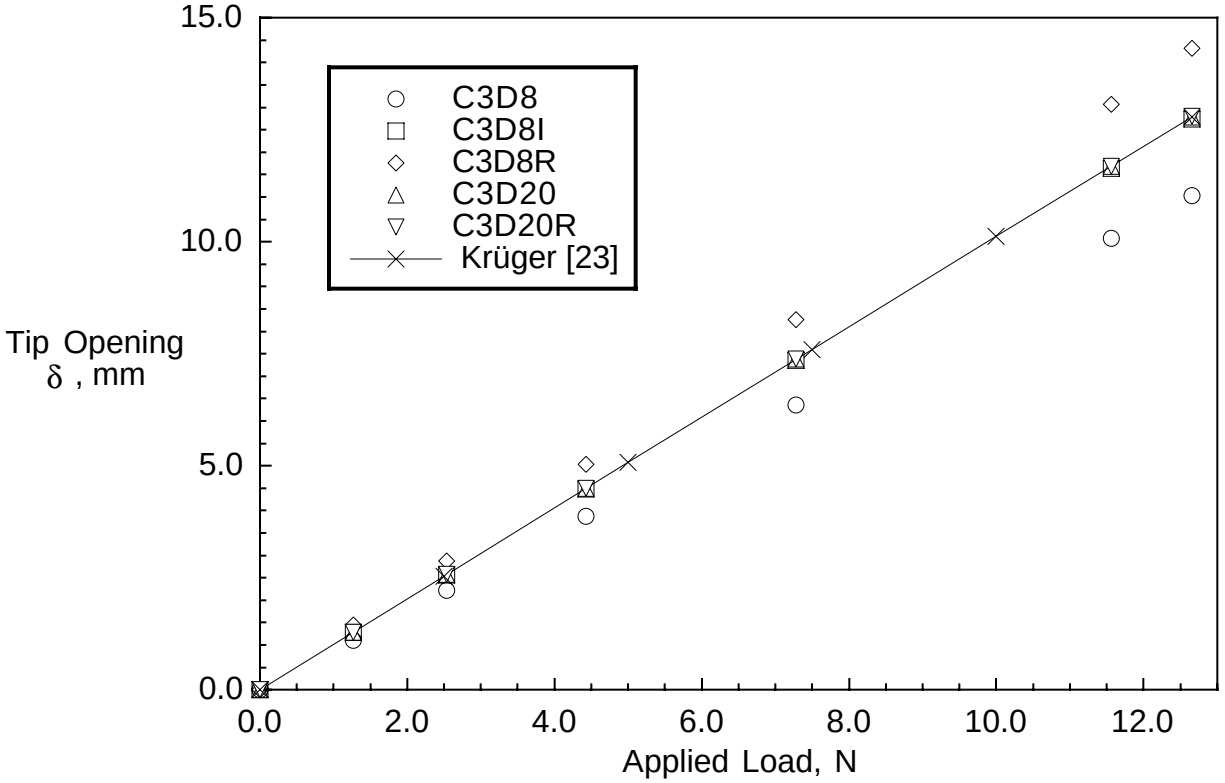

Figure 10. Influence of element selection on computed load-displacement behavior of a DCB specimen with UD24 layup .

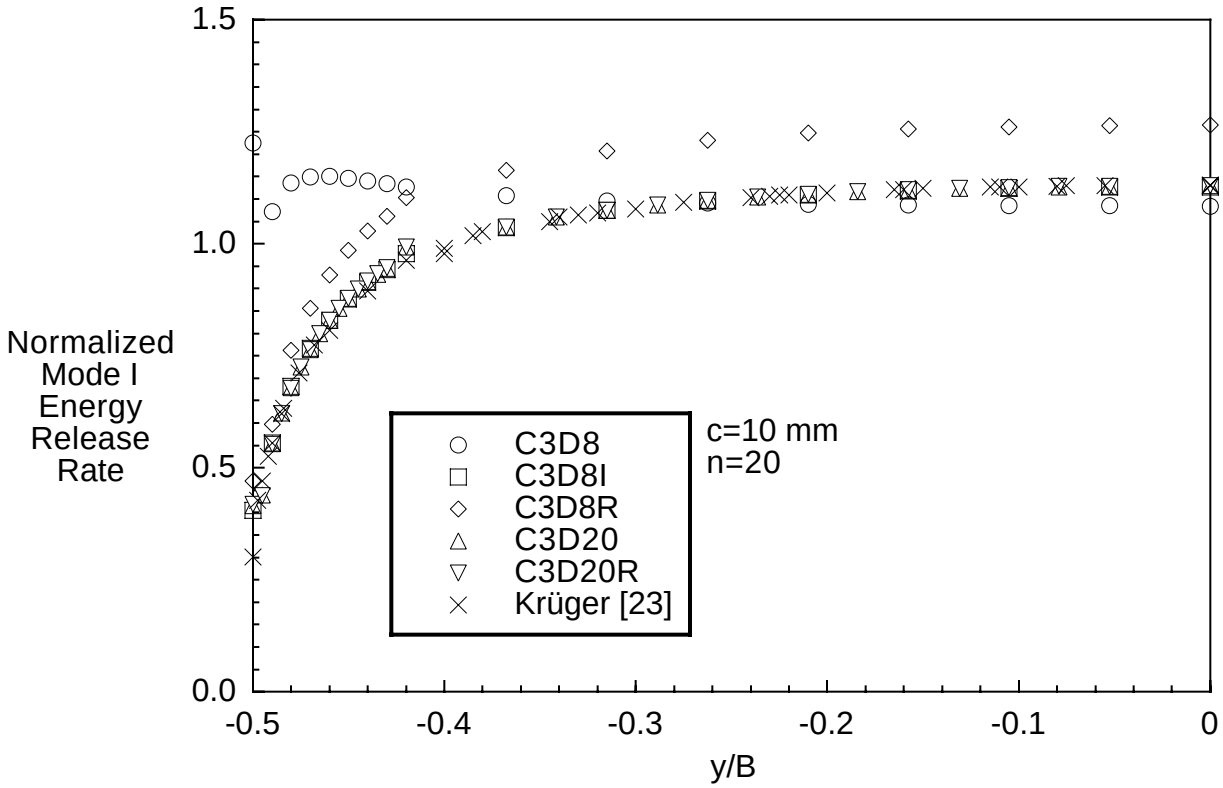

Figure 11. Influence of element selection on computed strain energy release rate distribution across the width of a DCB specimen with UD24 layup.

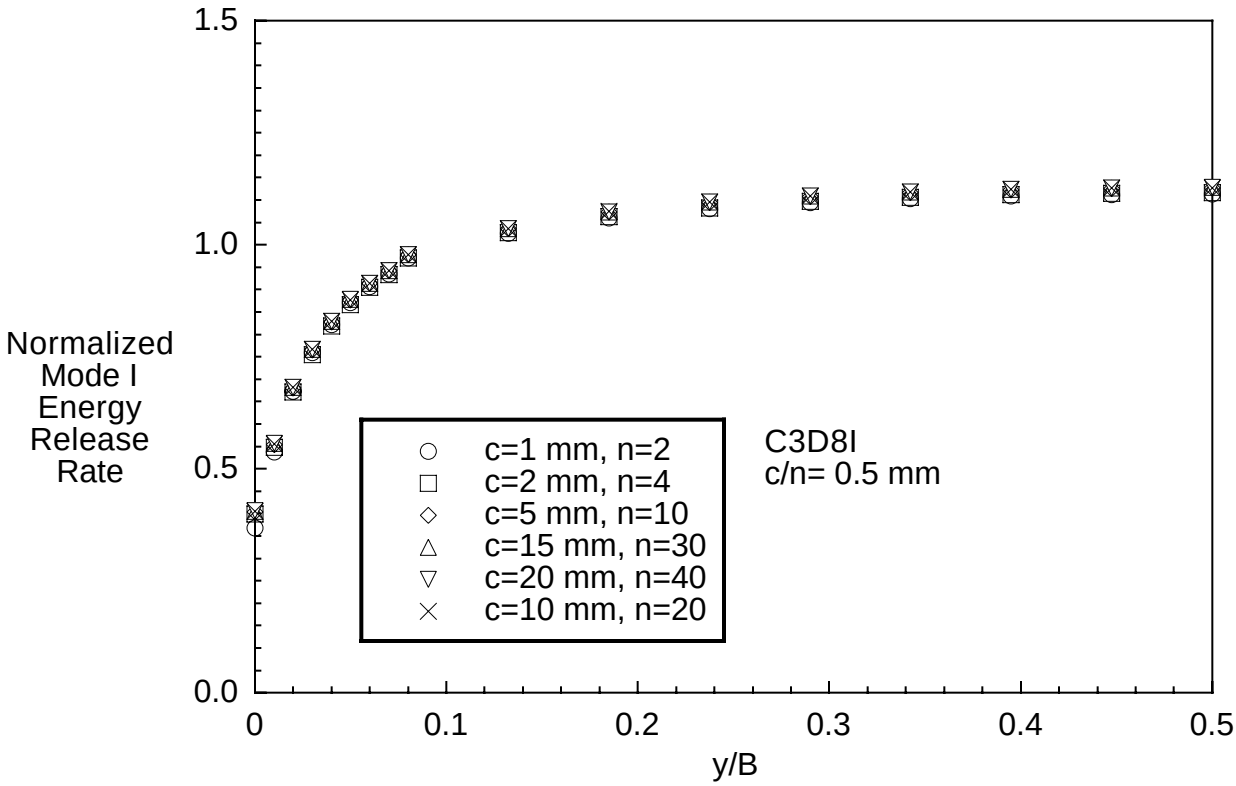

Figure 12. Influence of refined section on computed strain energy release rate distribution across the width of a DCB specimen with UD24 layup.

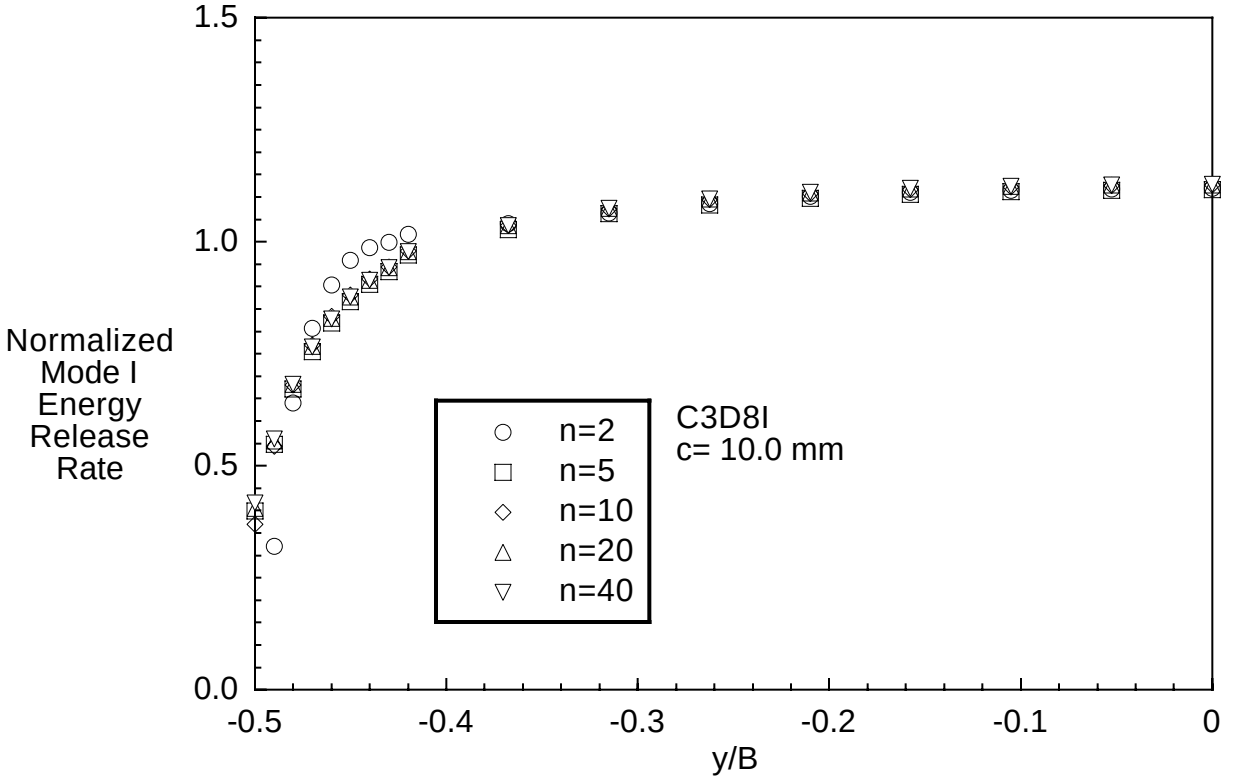

Figure 13. Influence of number of elements in refined section on computed strain energy release rate distribution across the width of a DCB specimen with UD24 layup.

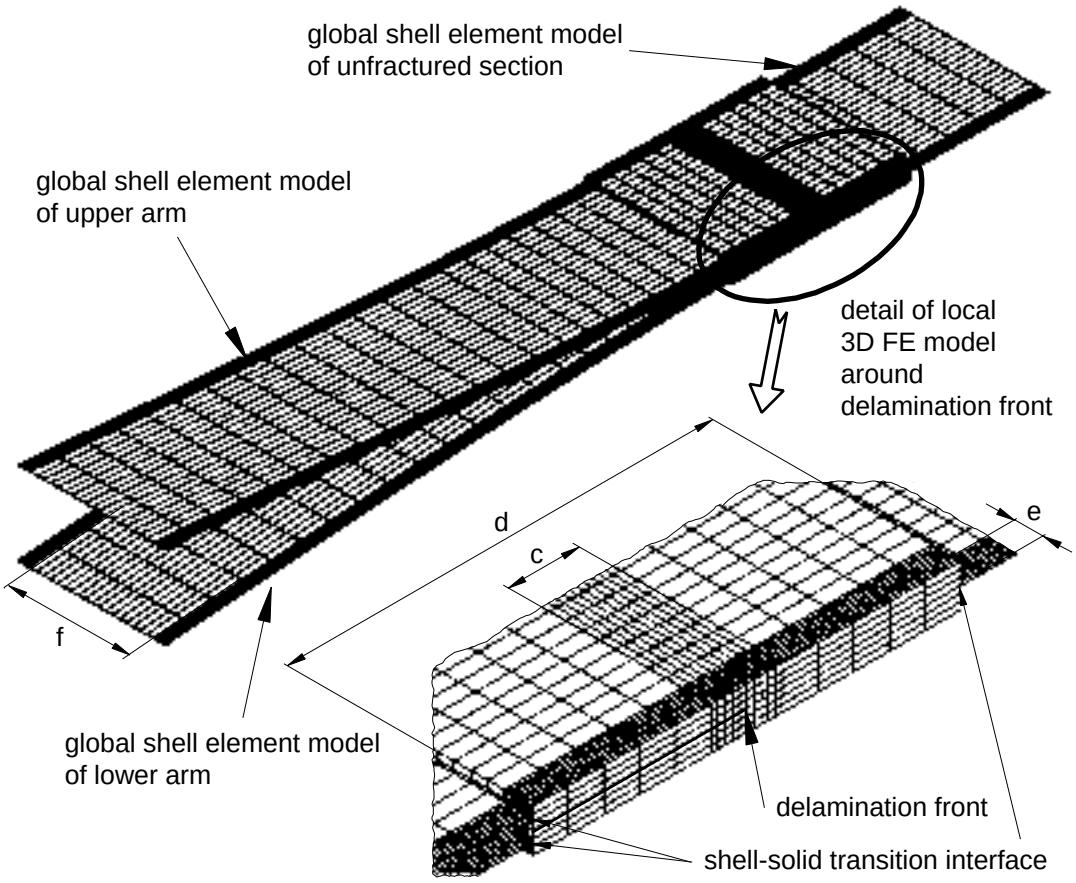

(a) FE model and detail around delamination front
(c= 5 mm, d= 30 mm, e= 2 mm, f= 21.0 mm)

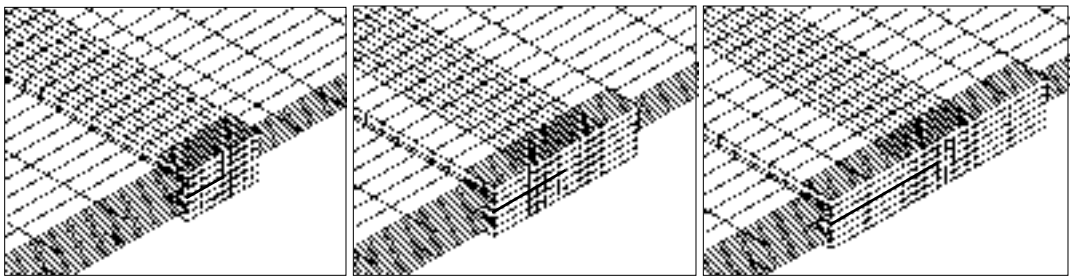

(b) Detail (c= d= 5 mm) (c) Detail (d= 10 mm) (d) Detail (d= 15 mm)

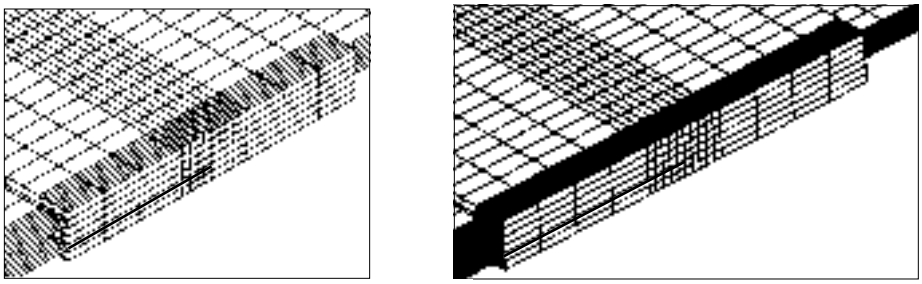

(e) Detail (d= 20 mm) (f) Detail (d= 25 mm)

Figure 14. Shell/3D Finite element model of a DCB Specimen with UD24 layup.

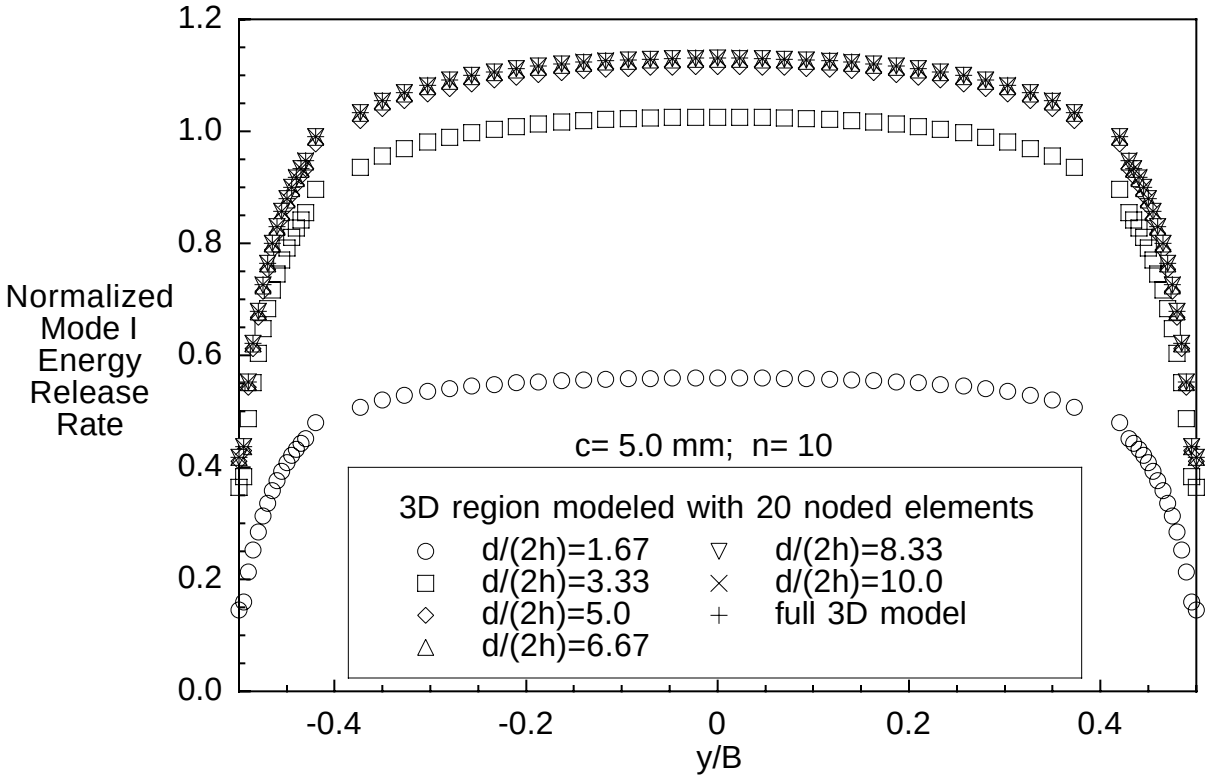

Figure 15. Strain energy release rate distribution across the width of a DCB specimen with UD24 layup modeled with 20 noded elements.

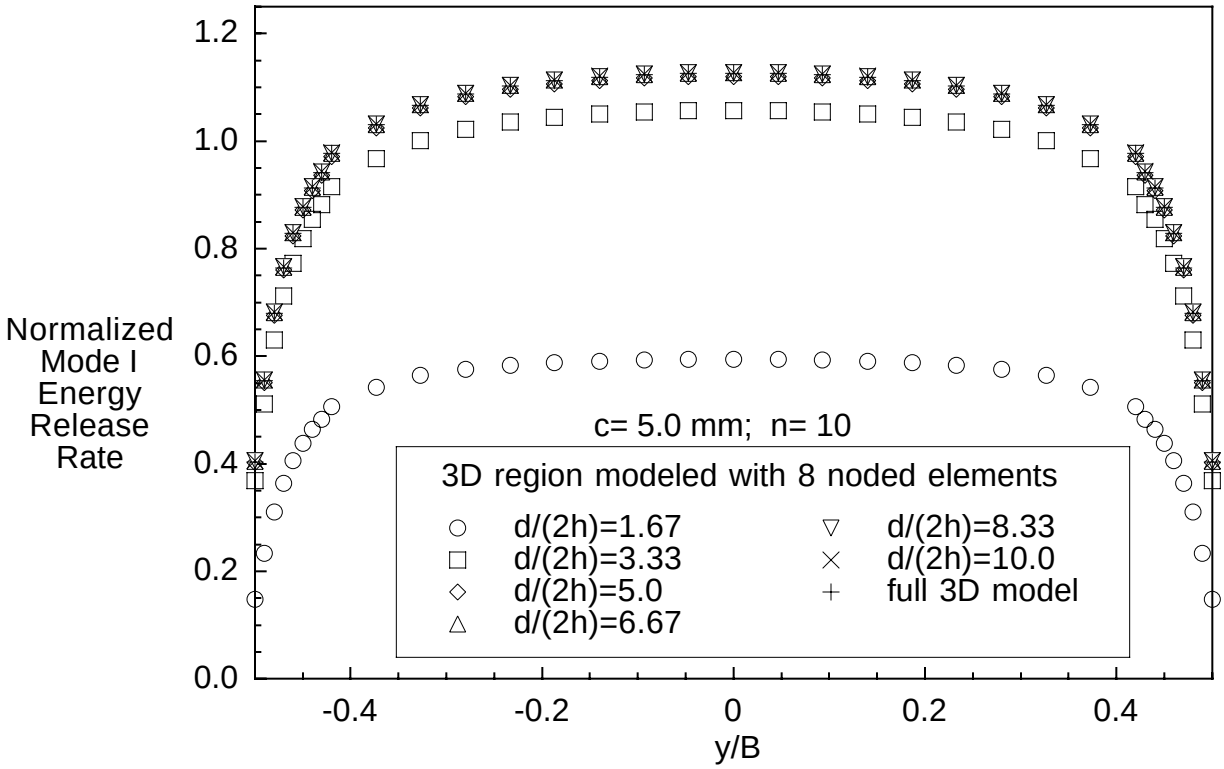

Figure 16. Strain energy release rate distribution across the width of a DCB specimen with UD24 layup modeled with 8 noded elements.

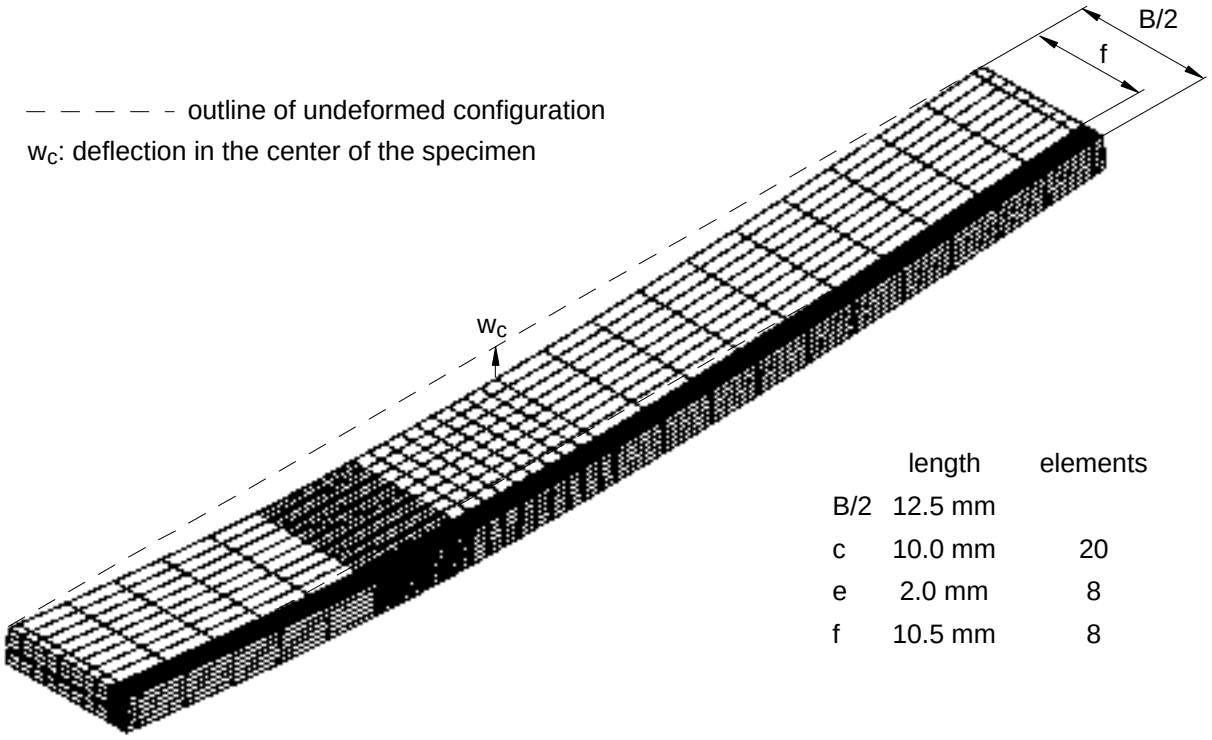

Figure 17. Finite element model of an ENF specimen with UD24 layup

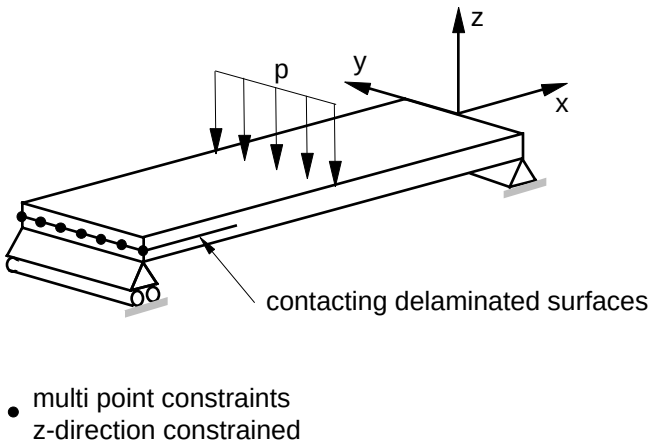

Figure 18. Multi point constraints to prevent contact of delaminated surfaces

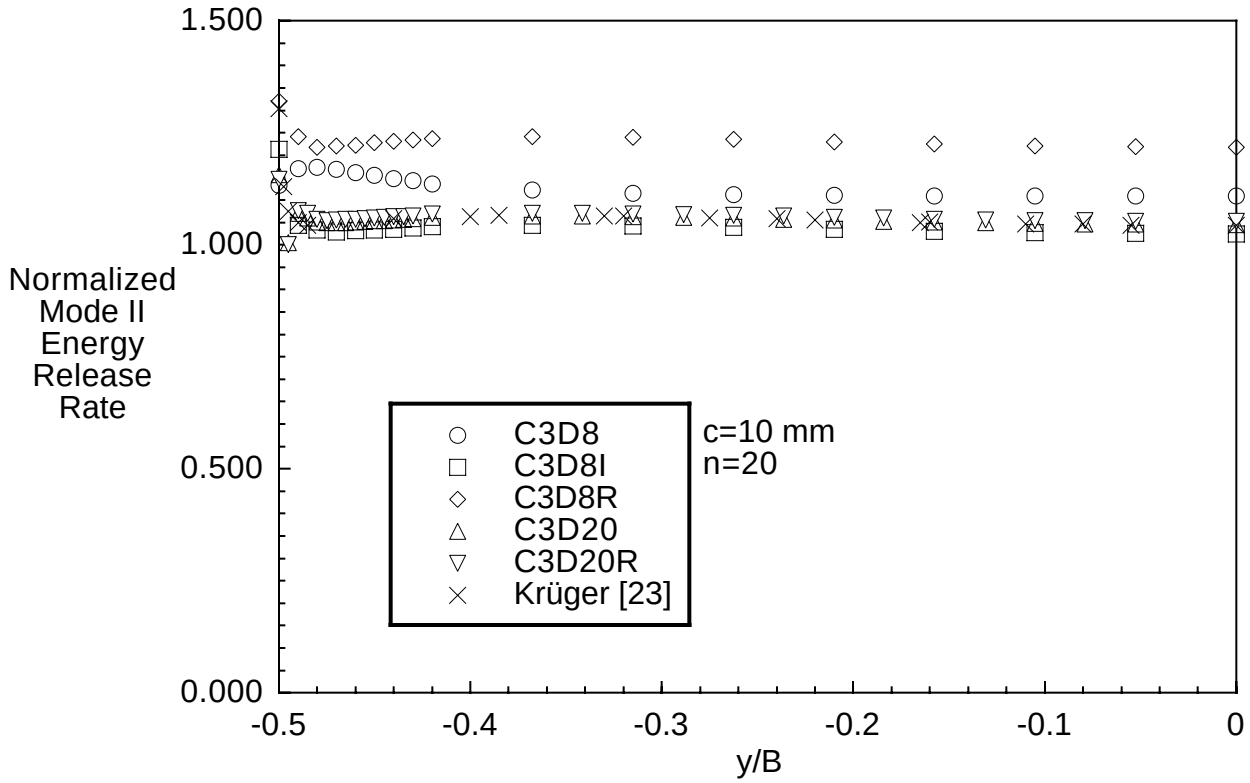

Figure 19. Influence of element selection on computed mode II strain energy release rate distribution across the width of an ENF specimen with UD24 layup.

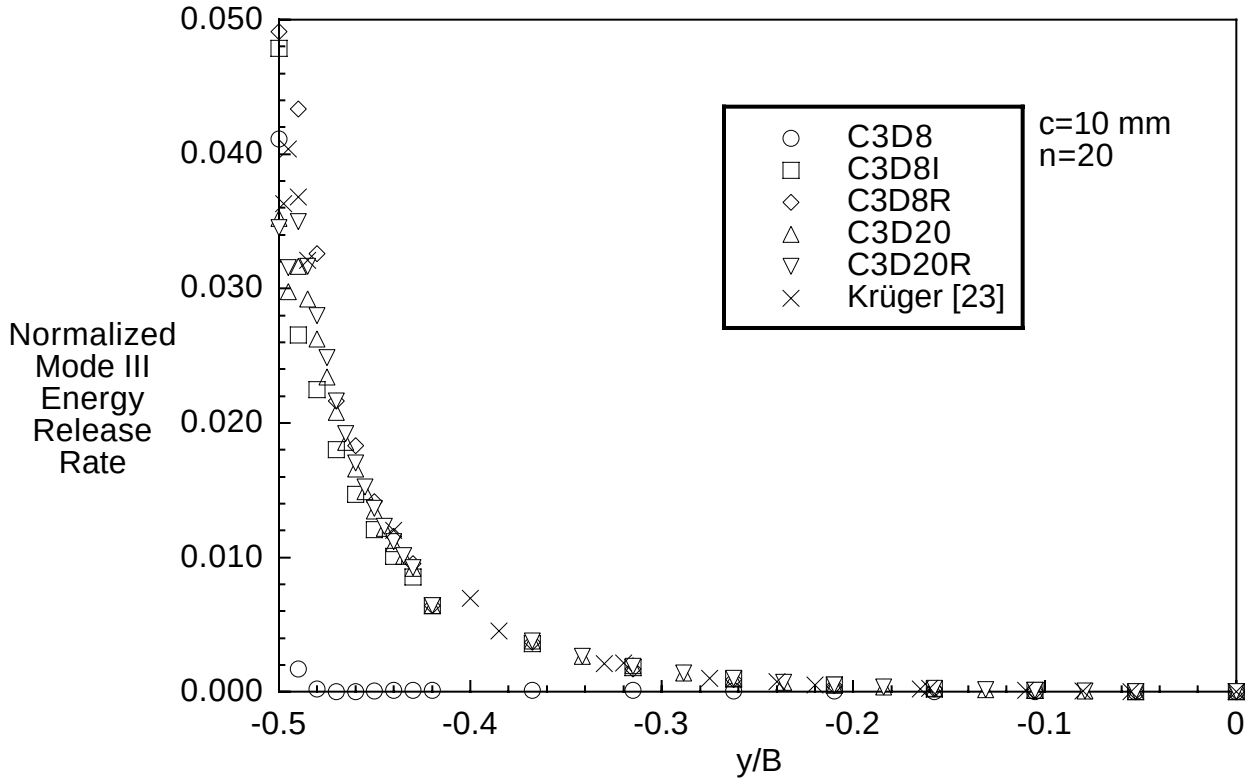

Figure 20. Influence of element selection on computed mode III strain energy release rate distribution across the width of an ENF specimen with UD24 layup.

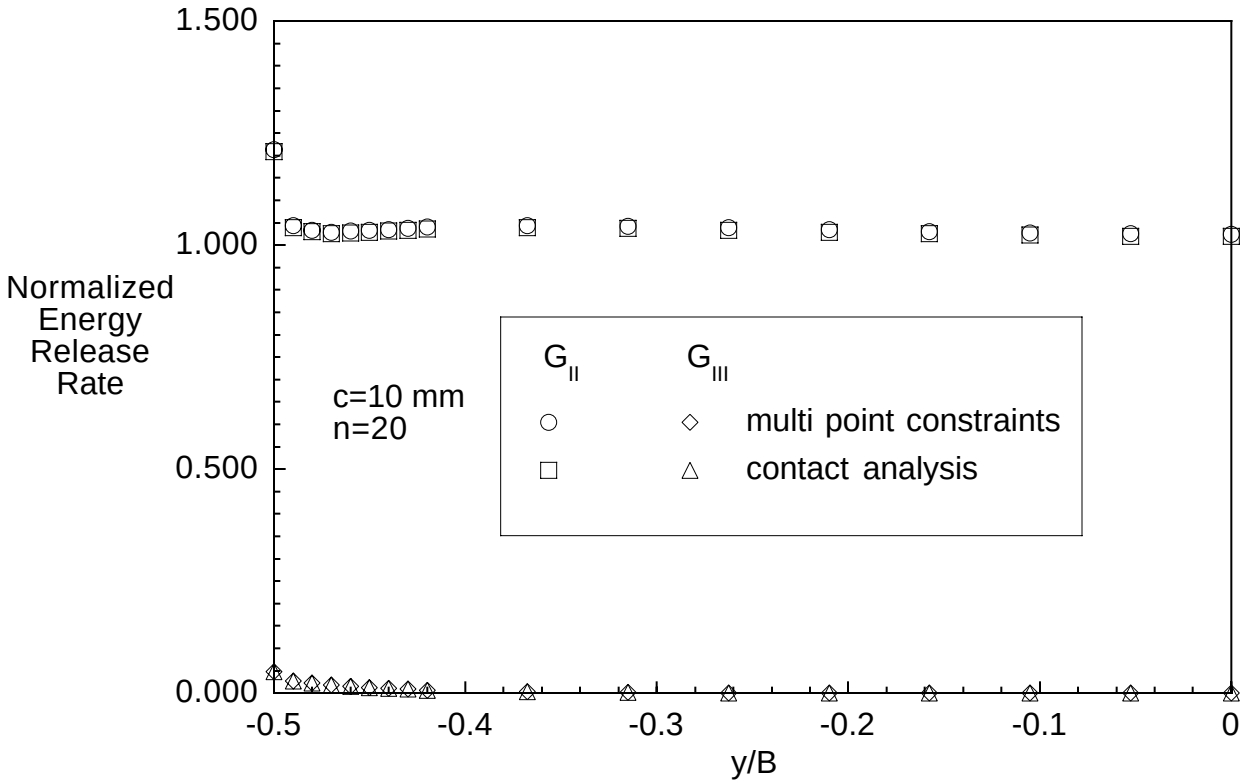

Figure 21. Influence of delamination surface contact on computed strain energy release rate distribution across the width of an ENF specimen with UD24 layup.

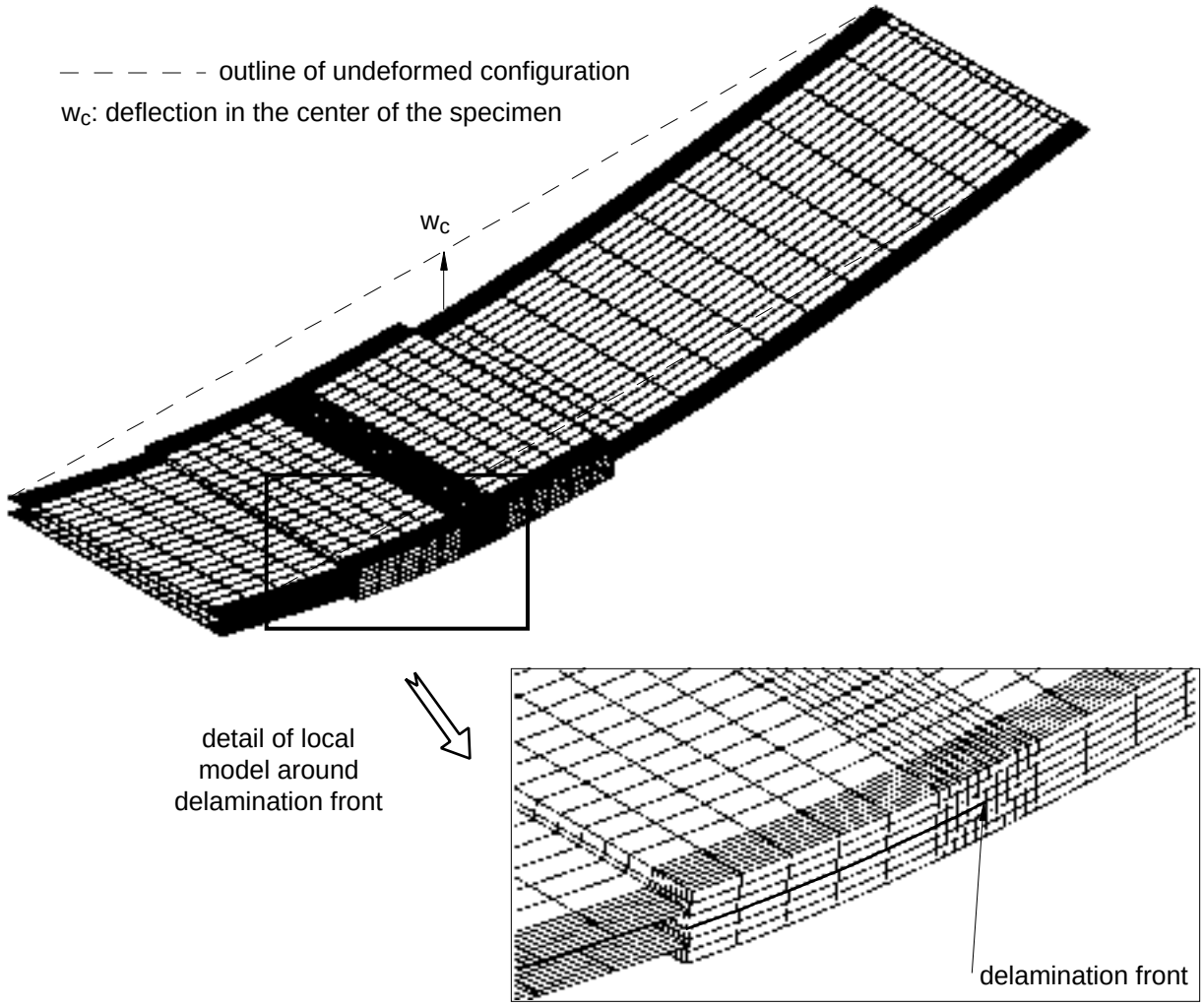

Figure 22. Shell/3Dfinite element model of an ENF specimen with UD24 layup
(c= 5 mm, n= 10, d= 30 mm)

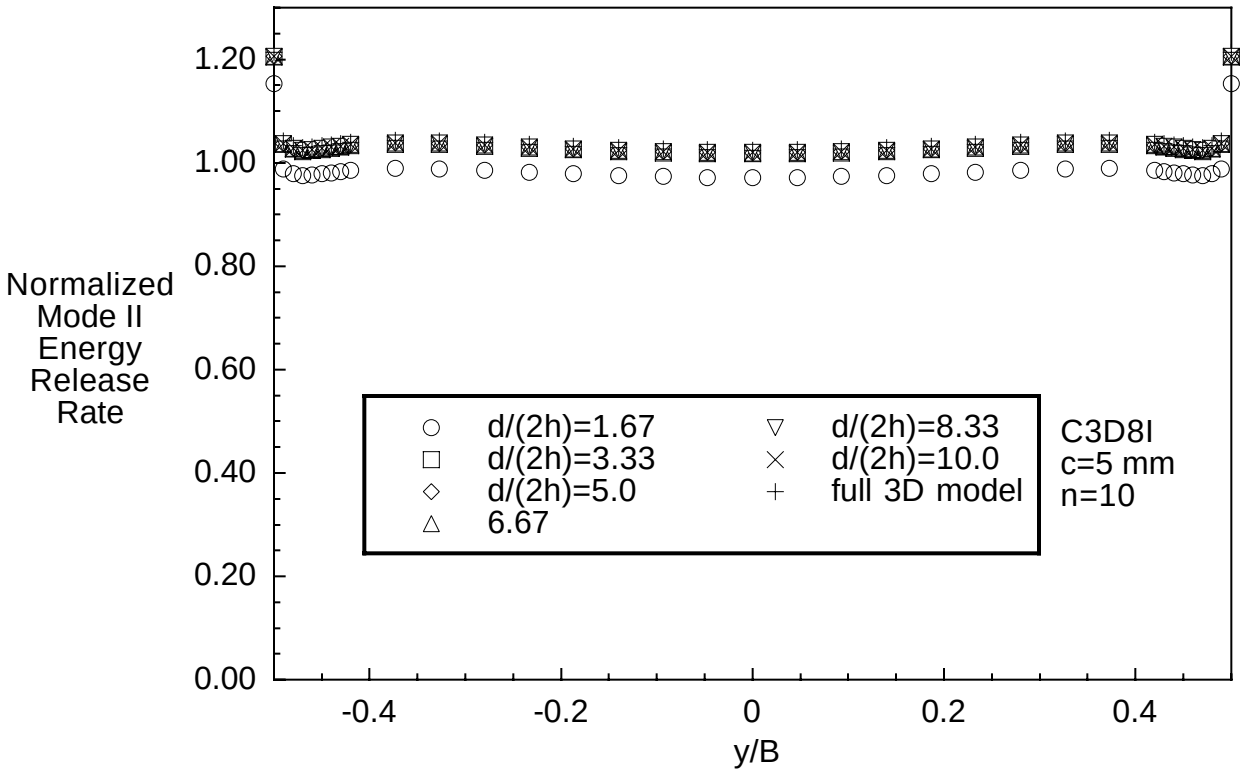

Figure 23. Mode II strain energy release rate distribution across the width of an ENF specimen with UD24 layup calculated using the shell/3D modeling technique

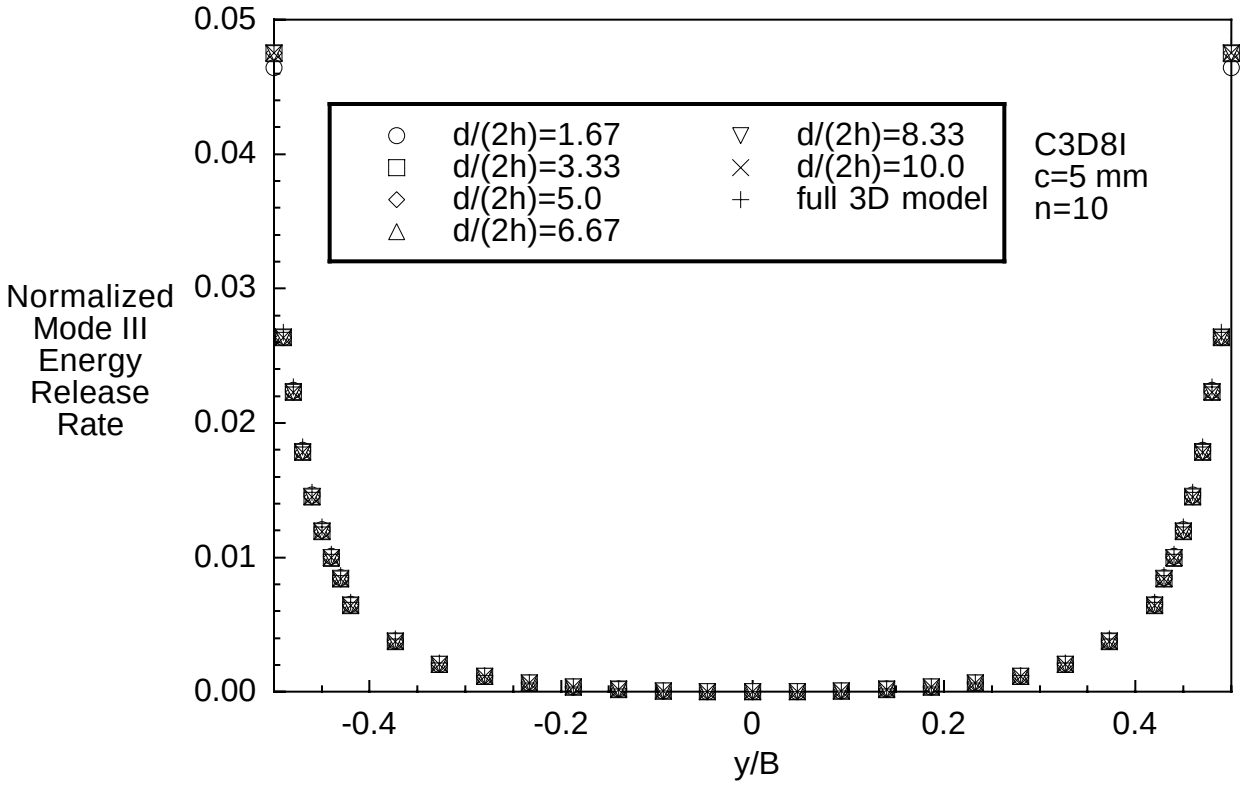

Figure 24. Mode III strain energy release rate distribution across the width of an ENF specimen with UD24 layup calculated using the shell/3D modeling technique.

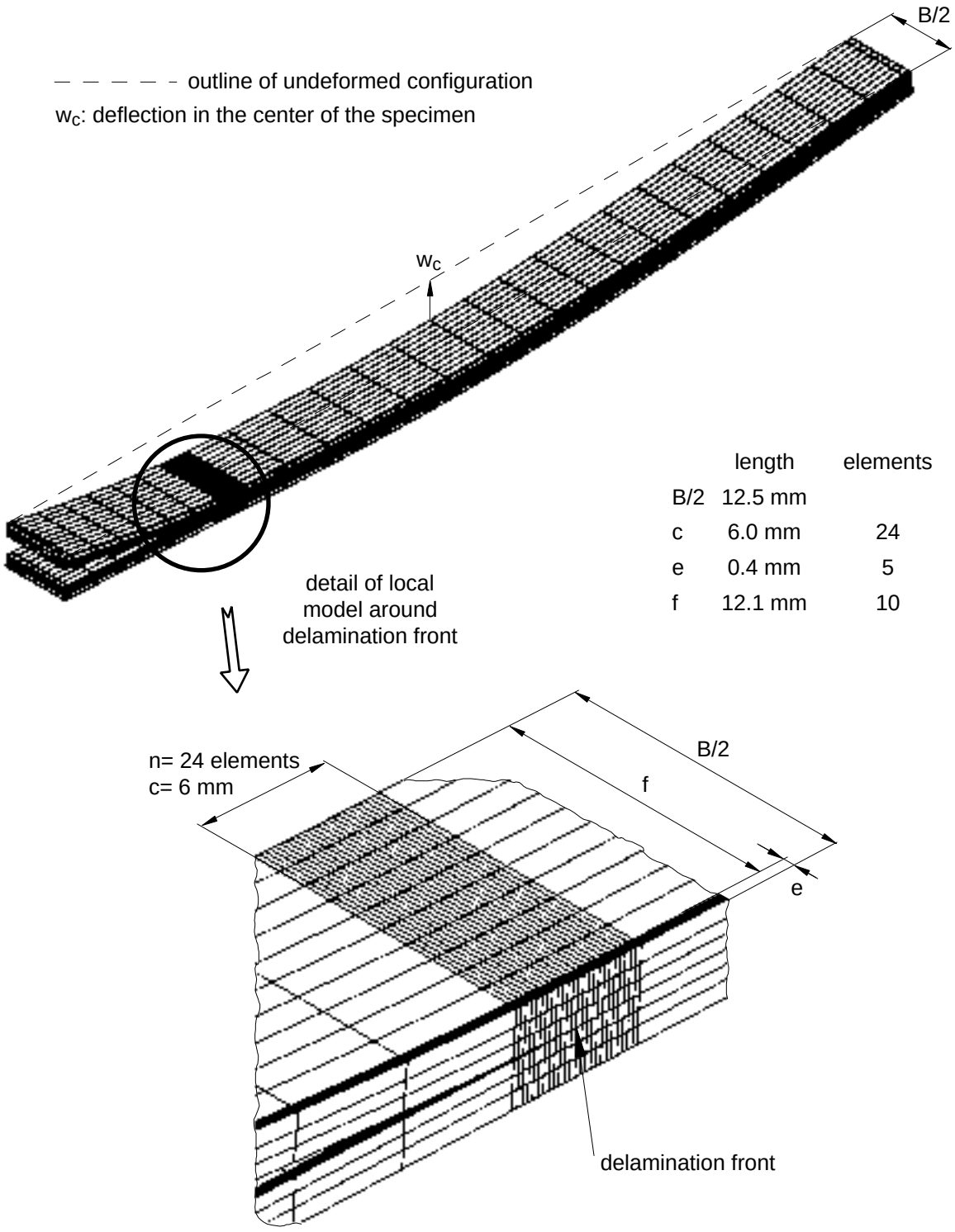

Figure 25. Finite element model of a SLB specimen with UD32 layup.

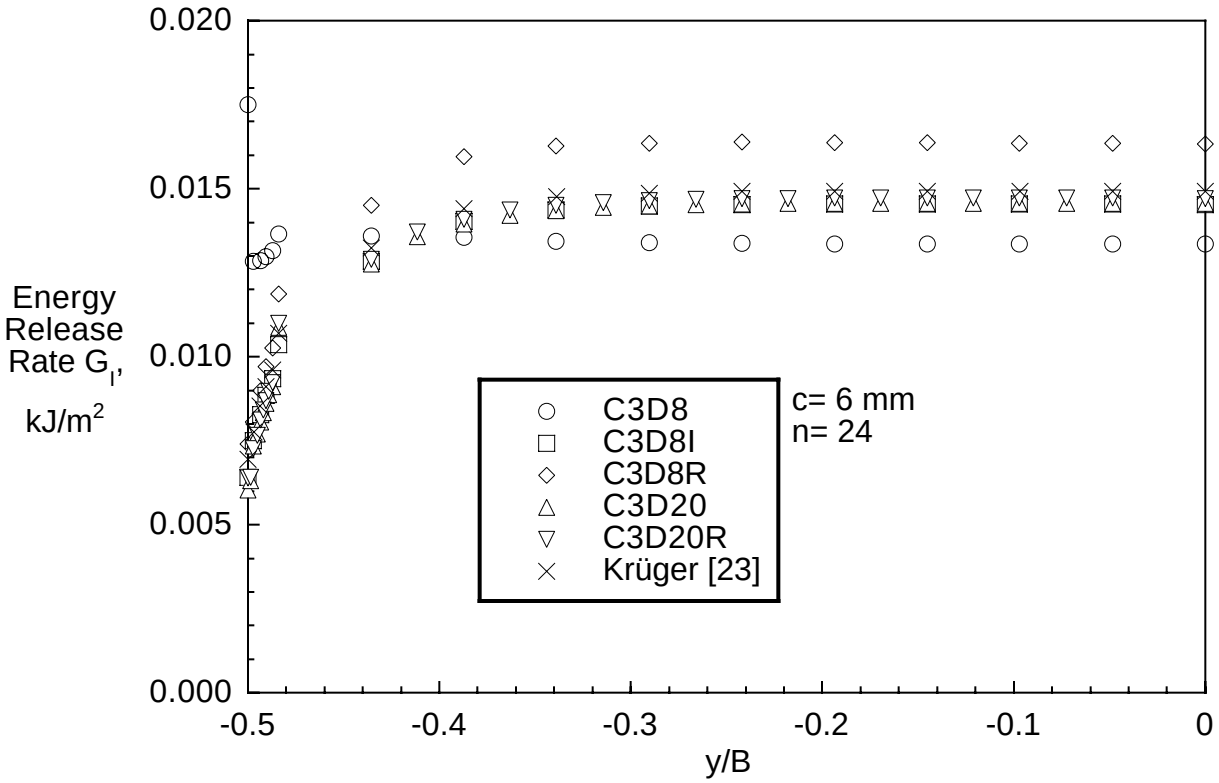

Figure 26. Influence of element selection on computed mode I strain energy release rate distribution across the width of a SLB specimen with UD32 layup.

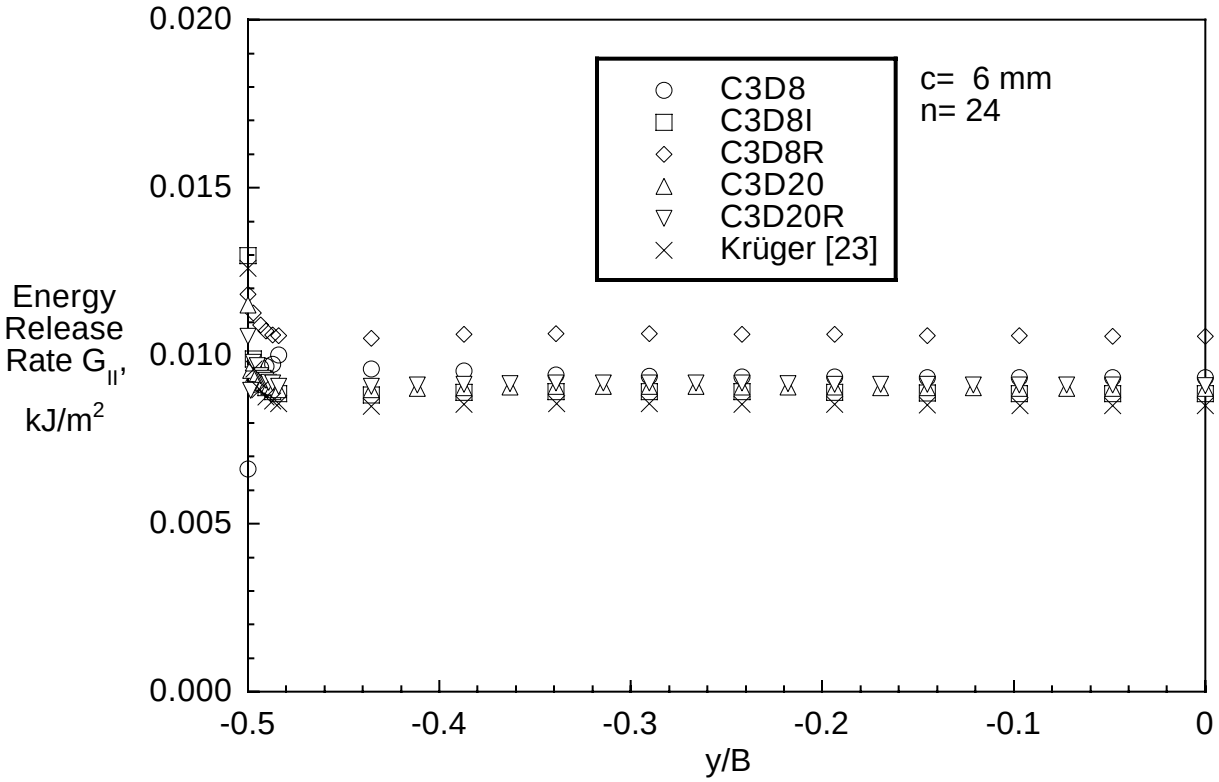

Figure 27. Influence of element selection on computed mode II strain energy release rate distribution across the width of a SLB specimen with UD32 layup.

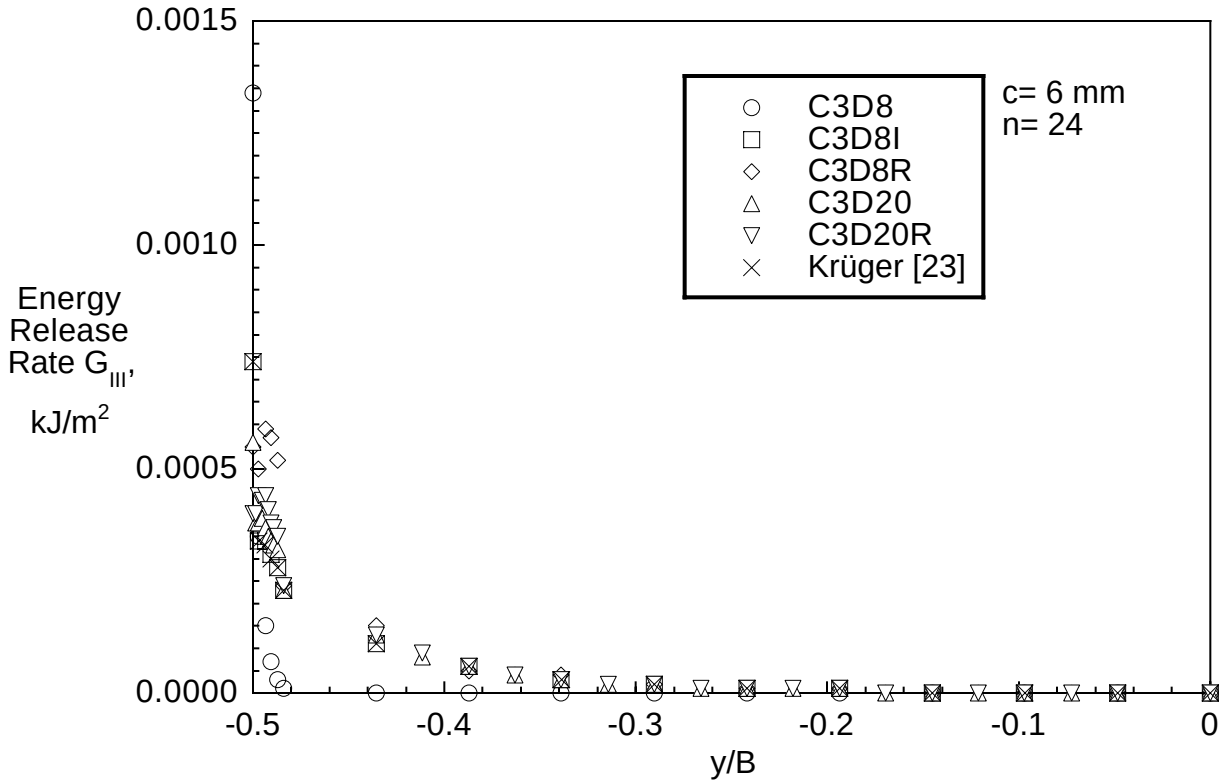

Figure 28. Influence of element selection on computed mode III strain energy release rate distribution across the width of a SLB specimen with UD32 layup.

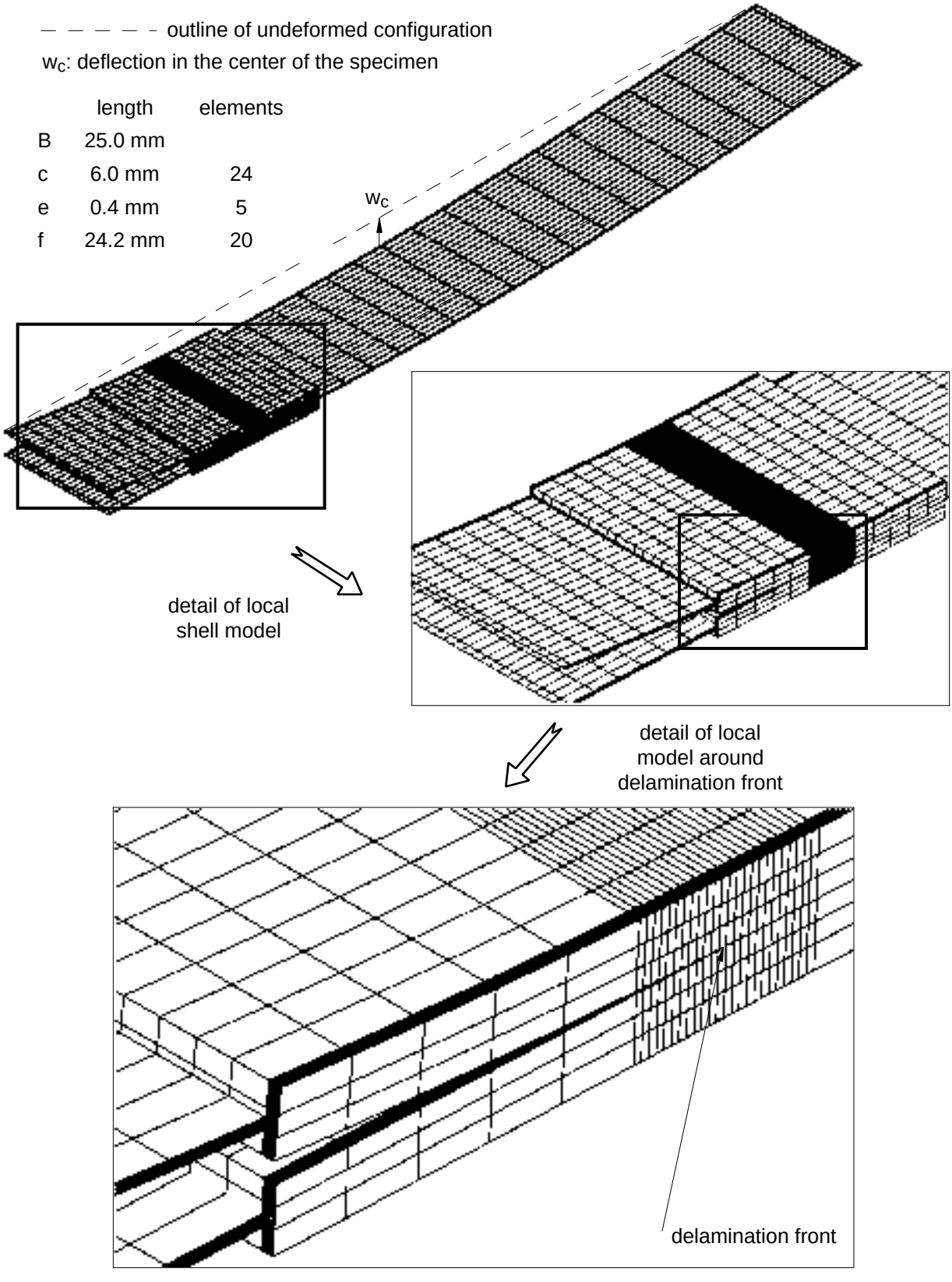

Figure 29. Shell/3Dfinite element model of a SLB Specimen with UD32 layup (c= 6mm, n= 24, d= 30 mm)

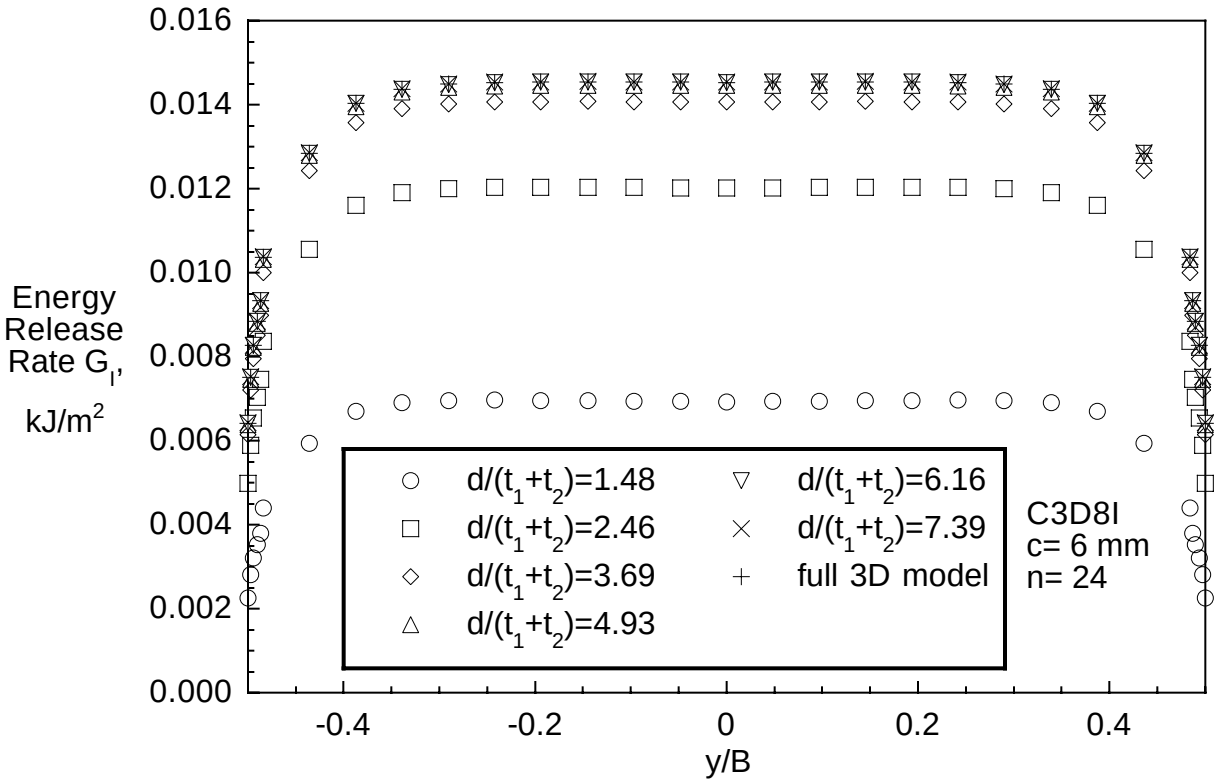

Figure 30. Mode I strain energy release rate distribution across the width of a SLB specimen with UD32 layup calculated using the shell/3D modeling technique

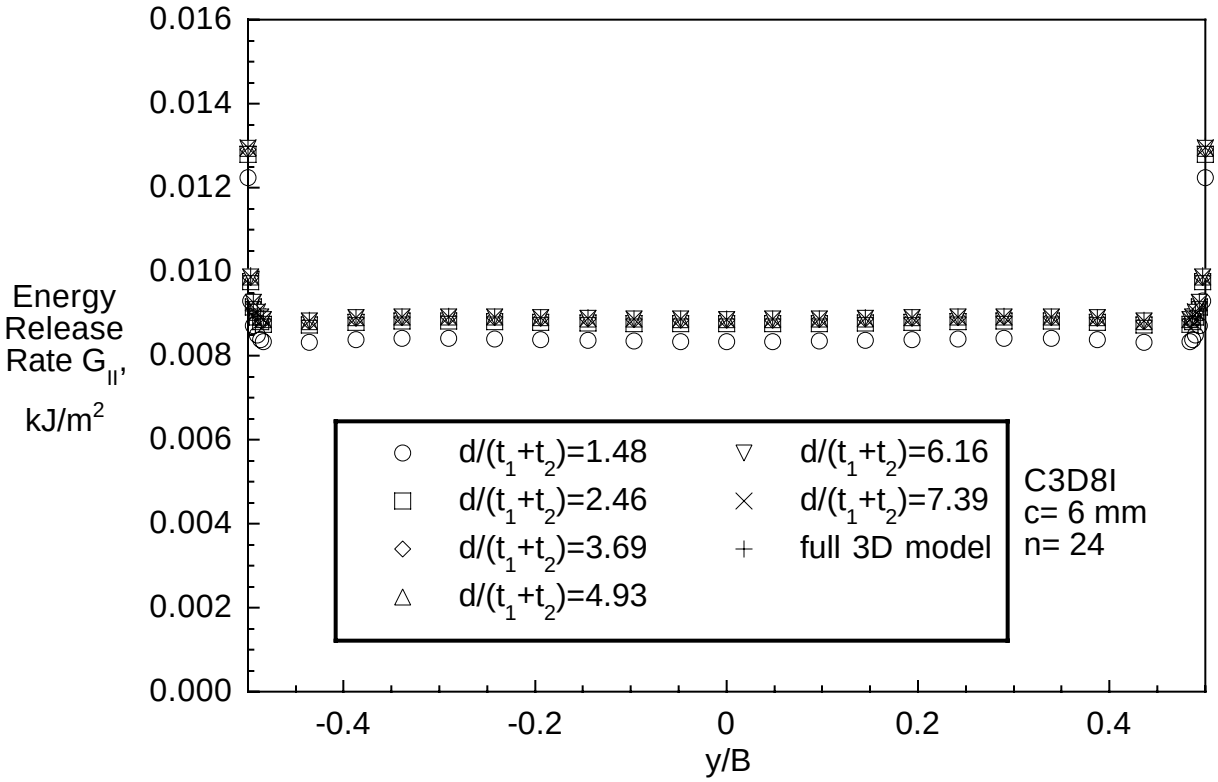

Figure 31. Mode II strain energy release rate distribution across the width of a SLB specimen with UD32 layup calculated using the shell/3D modeling technique

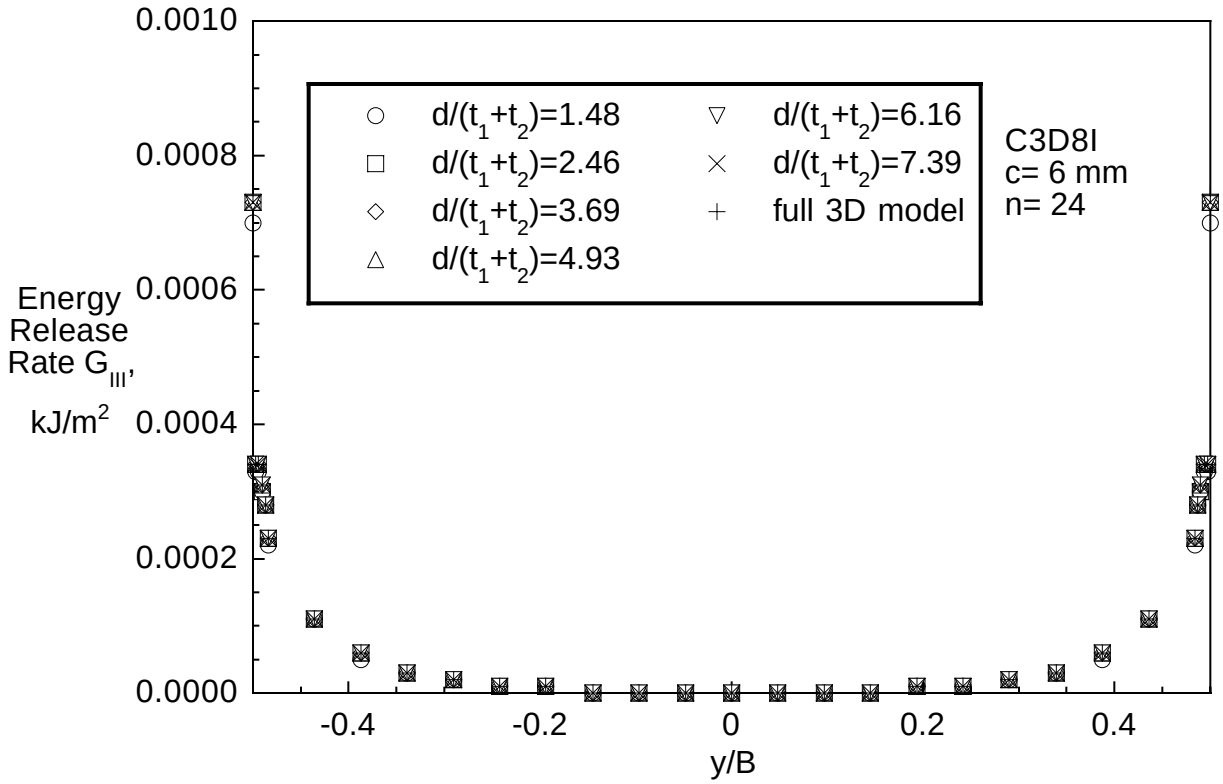

Figure 32. Mode III strain energy release rate distribution across the width of a SLB specimen with UD32 layup calculated using the shell/3D modeling technique

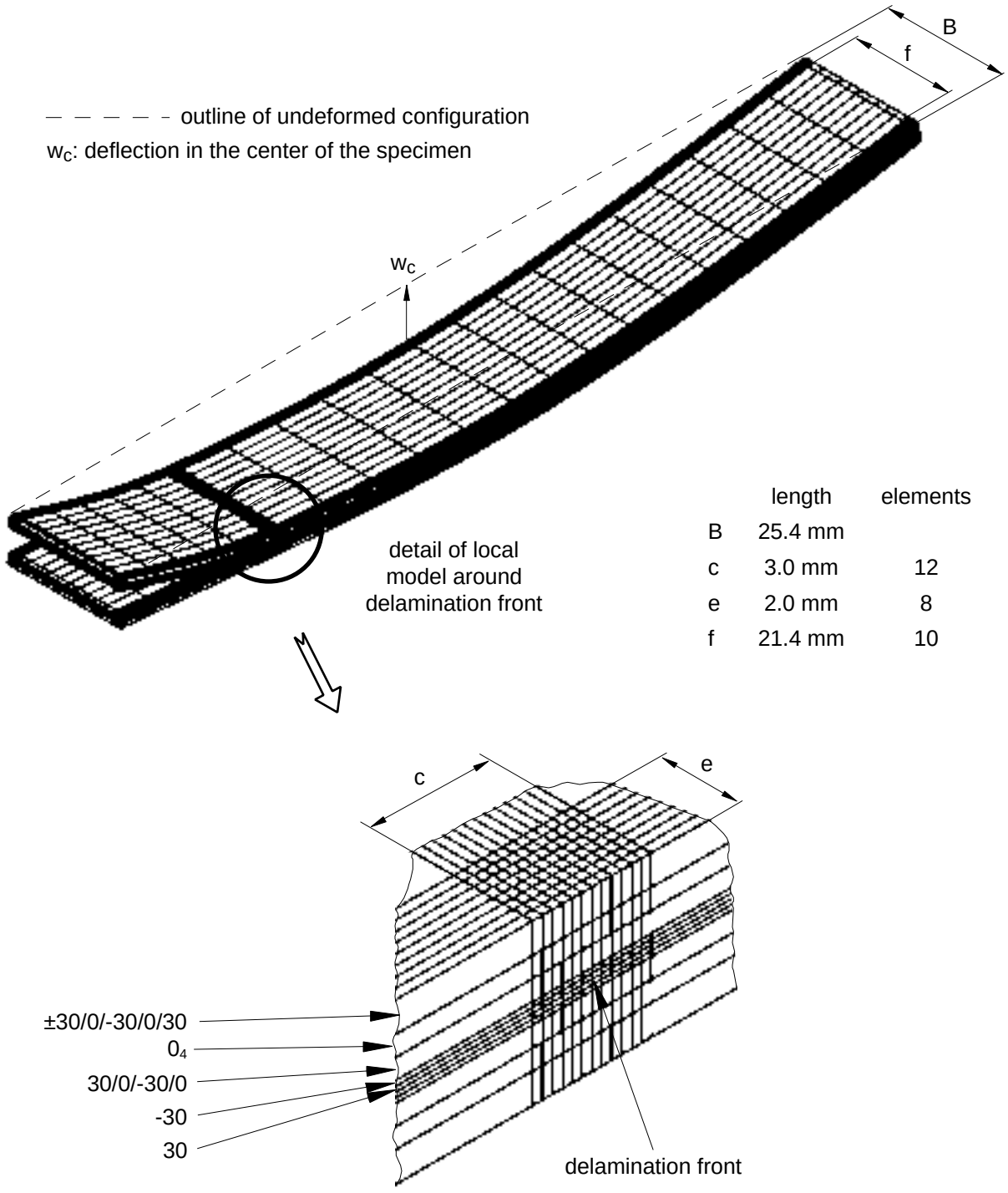

Figure 33. Finite element model of SLB specimen with D±30 layup

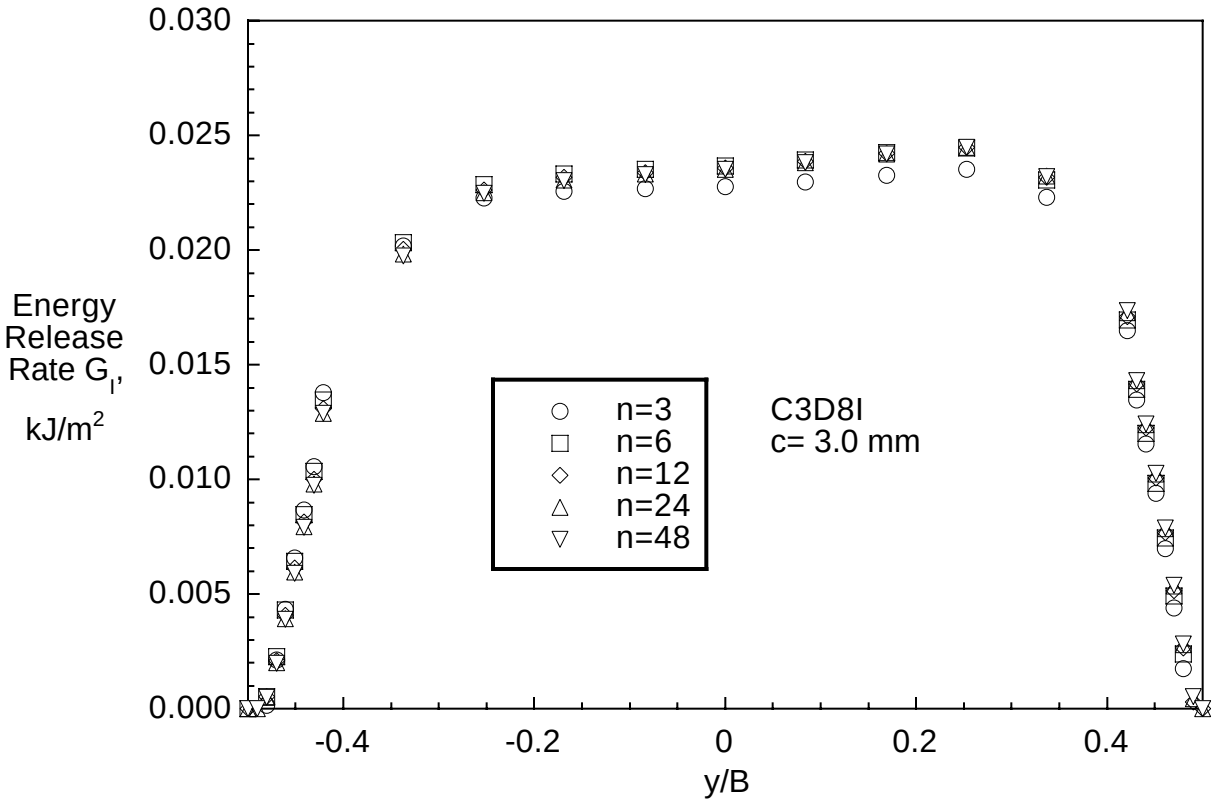

Figure 34. Influence of number of elements in refined section on computed mode I strain energy release rate distribution across the width of a SLB specimen with D±30 layup.

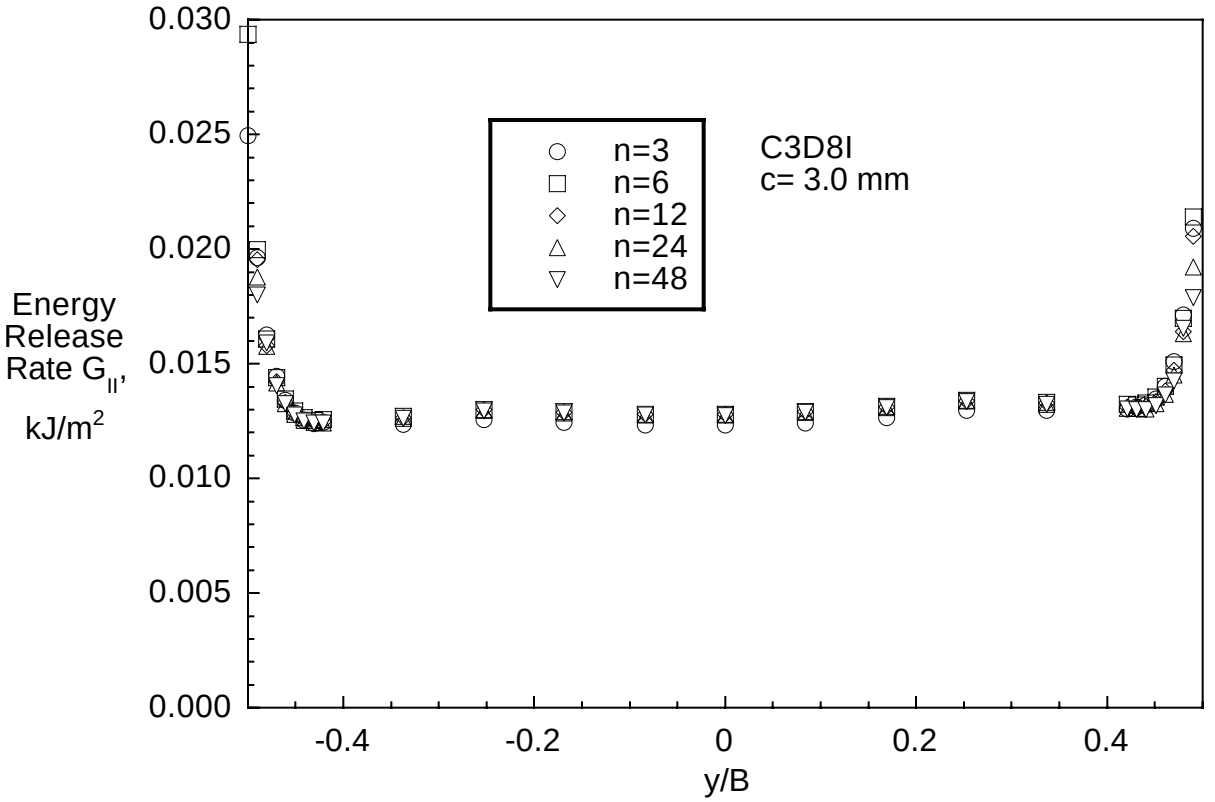

Figure 35. Influence of number of elements in refined section on computed mode II strain energy release rate distribution across the width of a SLB specimen with D±30 layup.

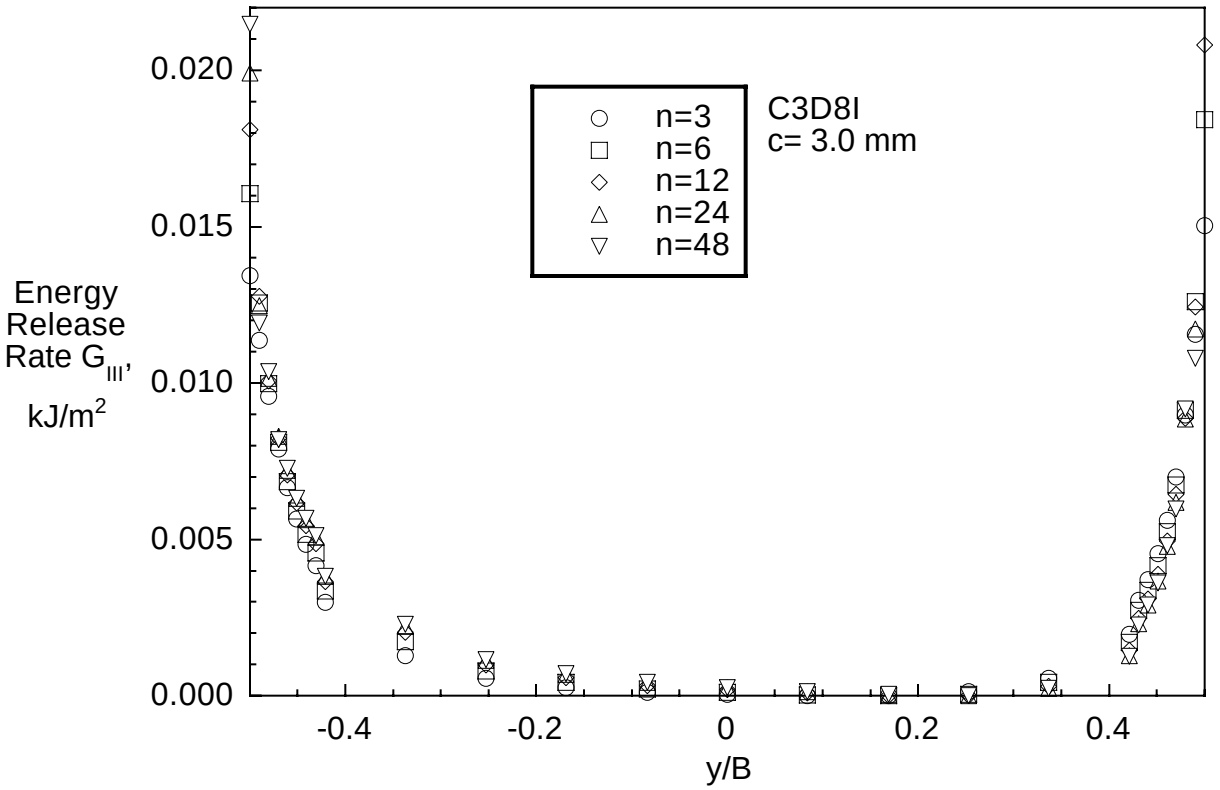

Figure 36. Influence of number of elements in refined section on computed mode III strain energy release rate distribution across the width of a SLB specimen with D±30 layup.

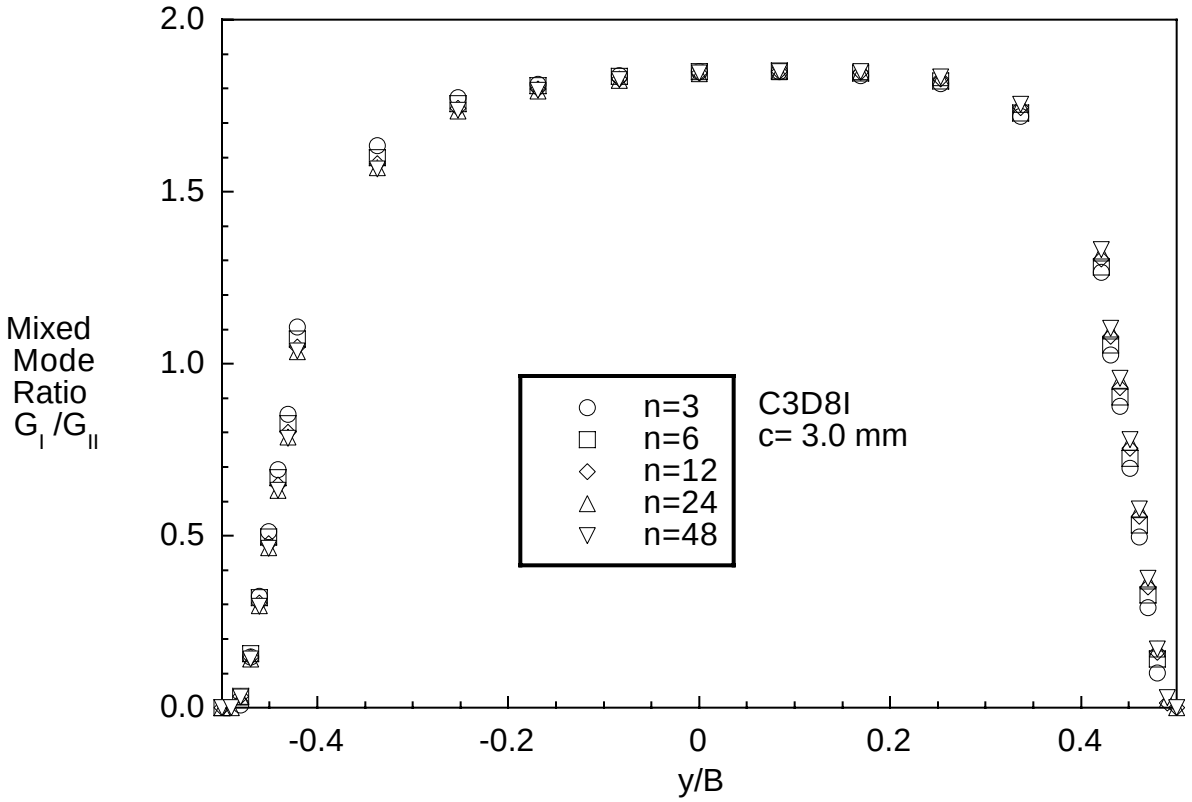

Figure 37. Influence of number of elements in refined section on mixed mode ratio distribution across the width of a SLB specimen with D±30 layup.

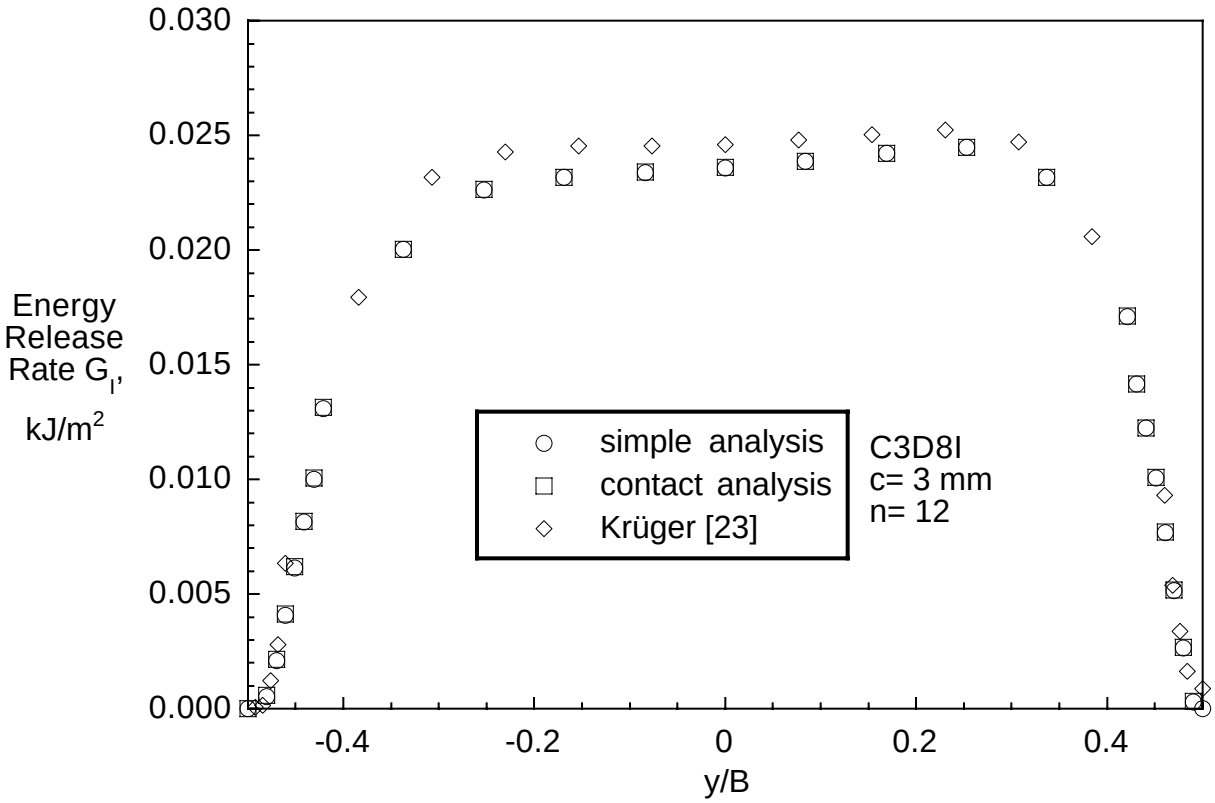

Figure 38. Influence of delamination surface contact on computed mode I strain energy release rate distribution across the width of SLB specimen with D±30 layup.

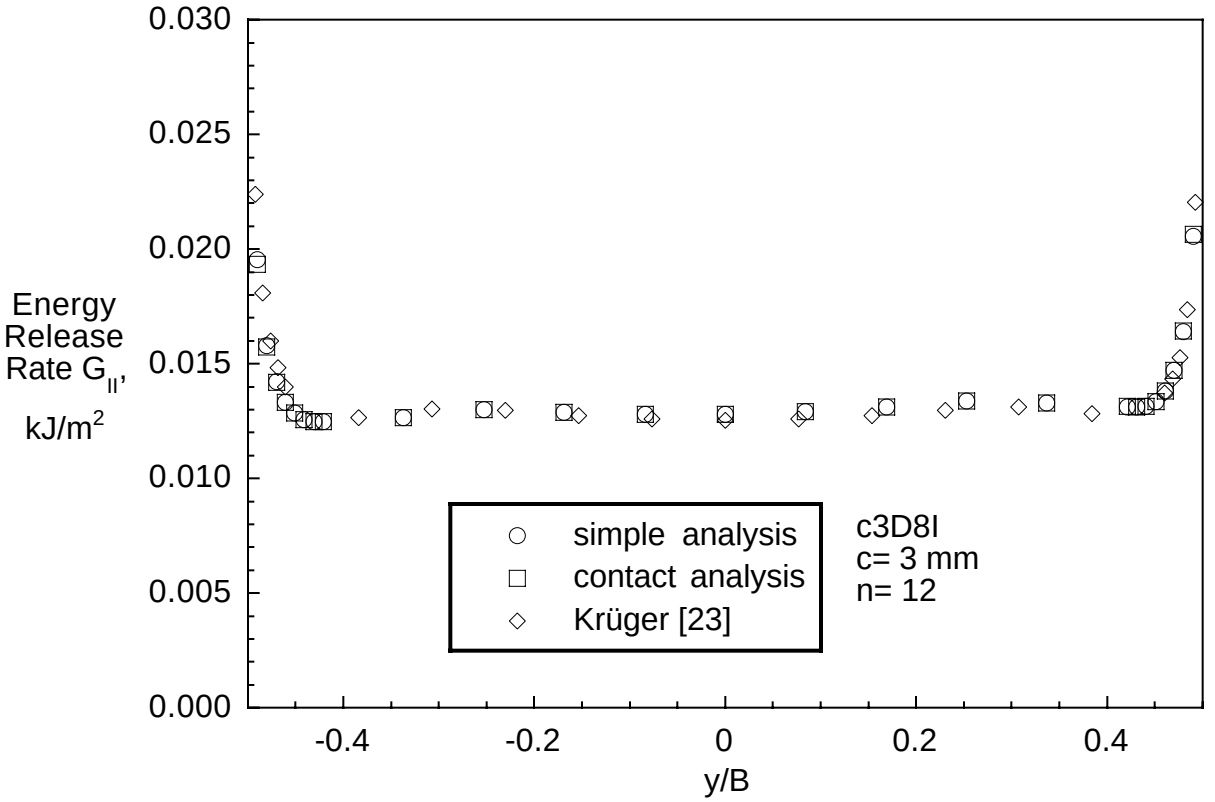

Figure 39. Influence of delamination surface contact on computed mode II strain energy release rate distribution across the width of SLB specimen with D±30 layup.

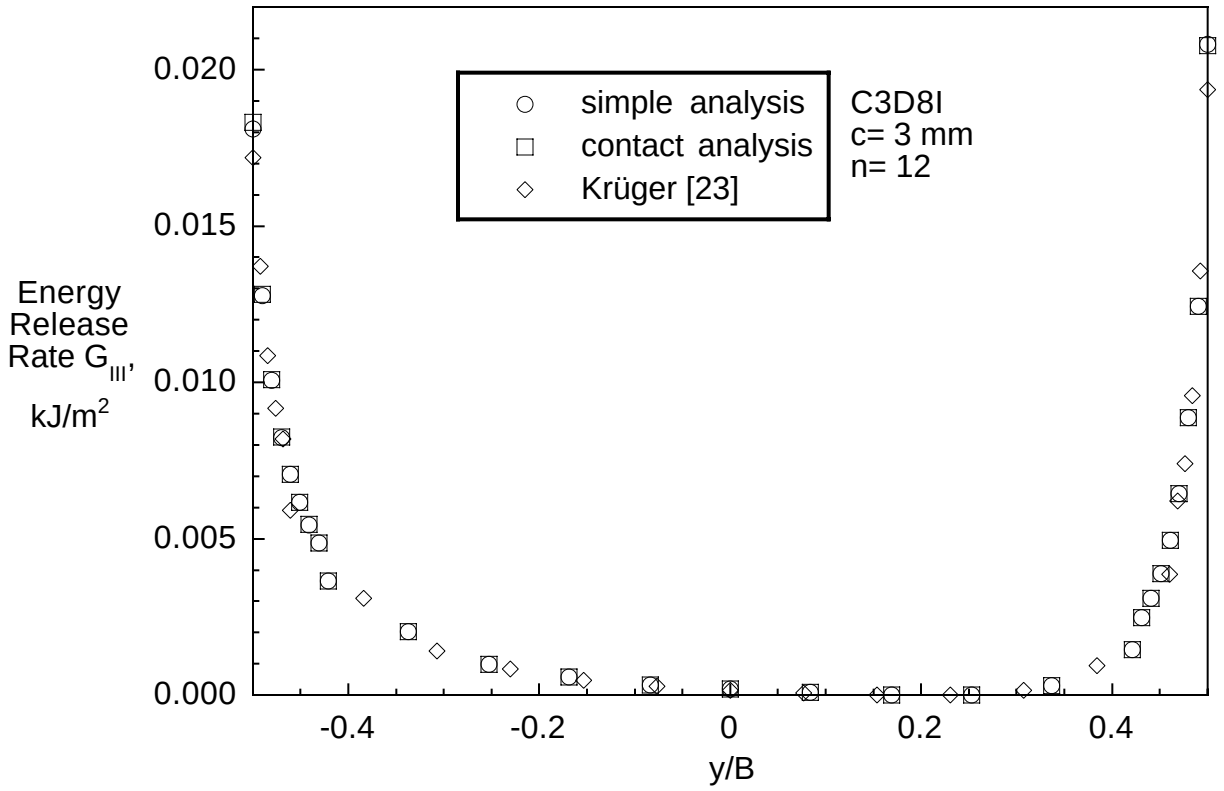

Figure 40. Influence of delamination surface contact on computed mode III strain energy release rate distribution across the width of SLB specimen with D±30 layup.

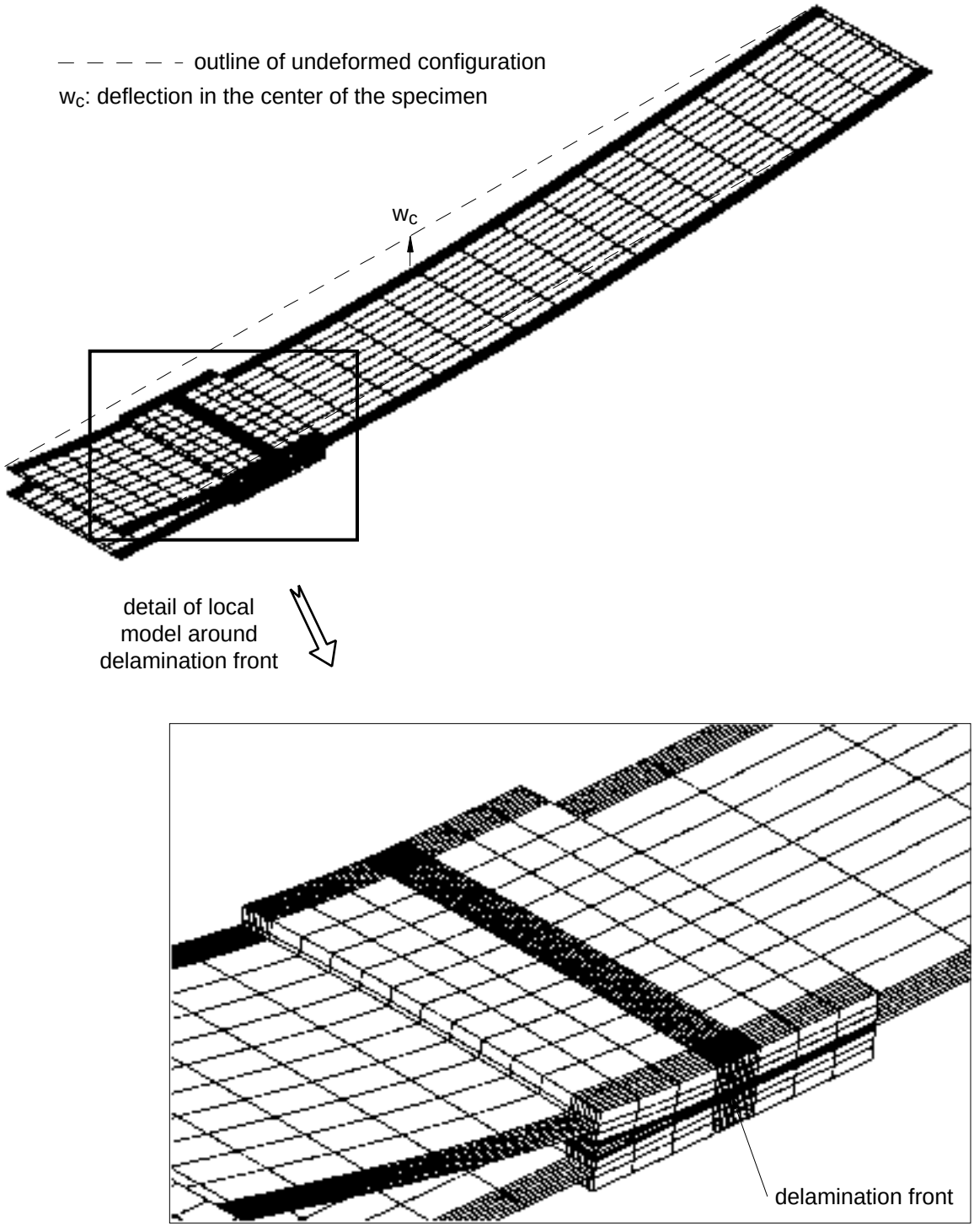

Figure 41. Shell/3Dfinite element model of a SLB specimen with D±30 layup (c= 3 mm, n=12, d= 20 mm)

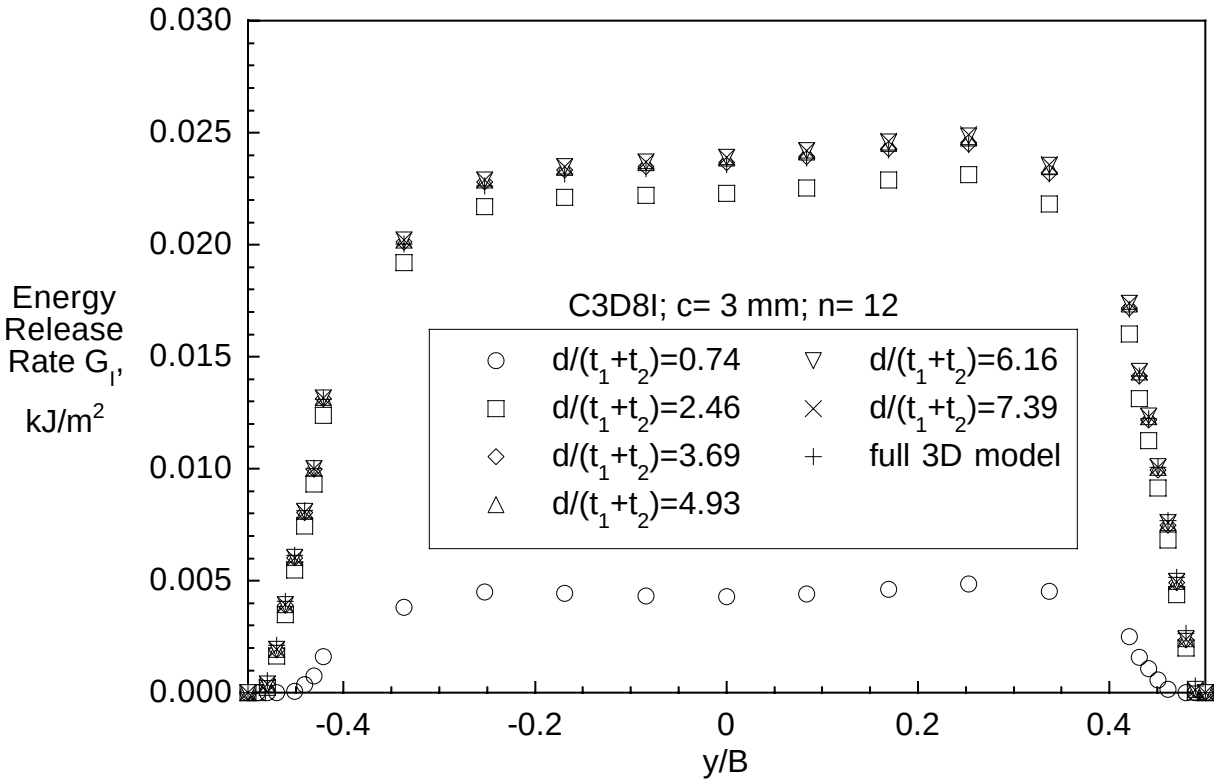

Figure 42. Mode I strain energy release rate distribution across the width of a SLB specimen with D±30 layup calculated using the shell/3D modeling technique

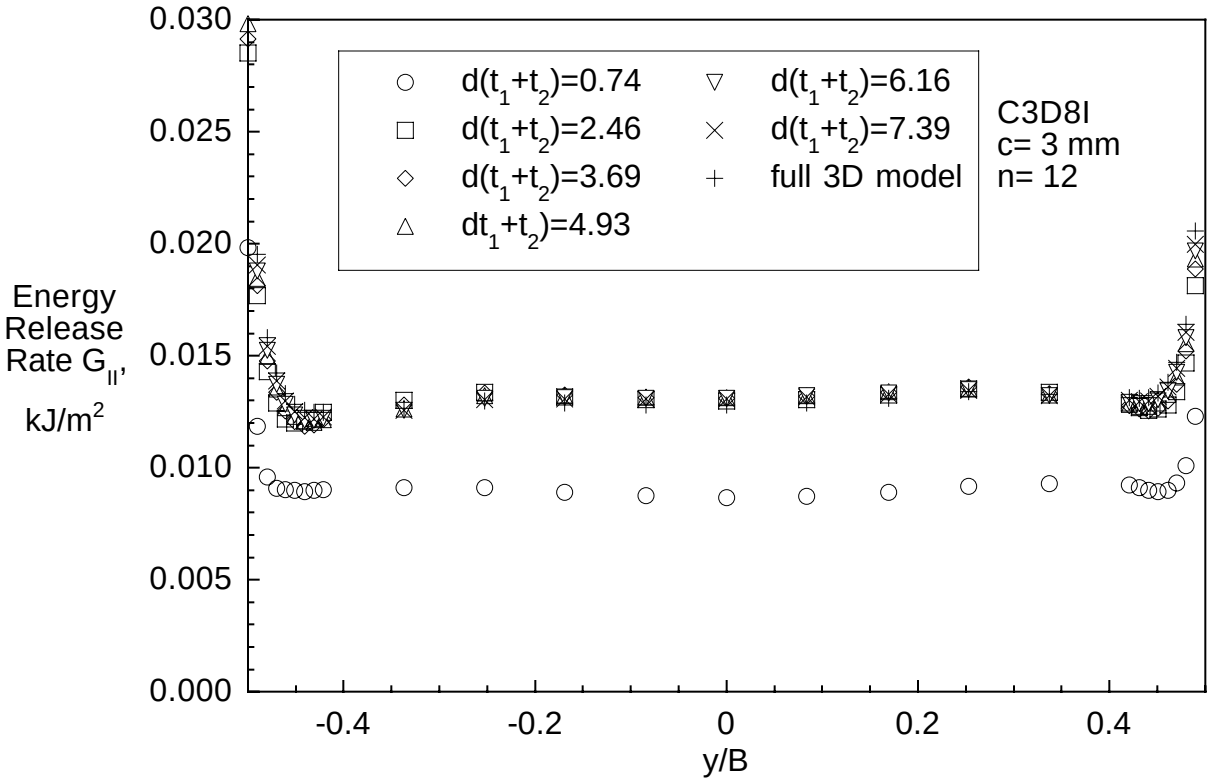

Figure 43. Mode II strain energy release rate distribution across the width of a SLB specimen with D±30 layup calculated using the shell/3D modeling technique

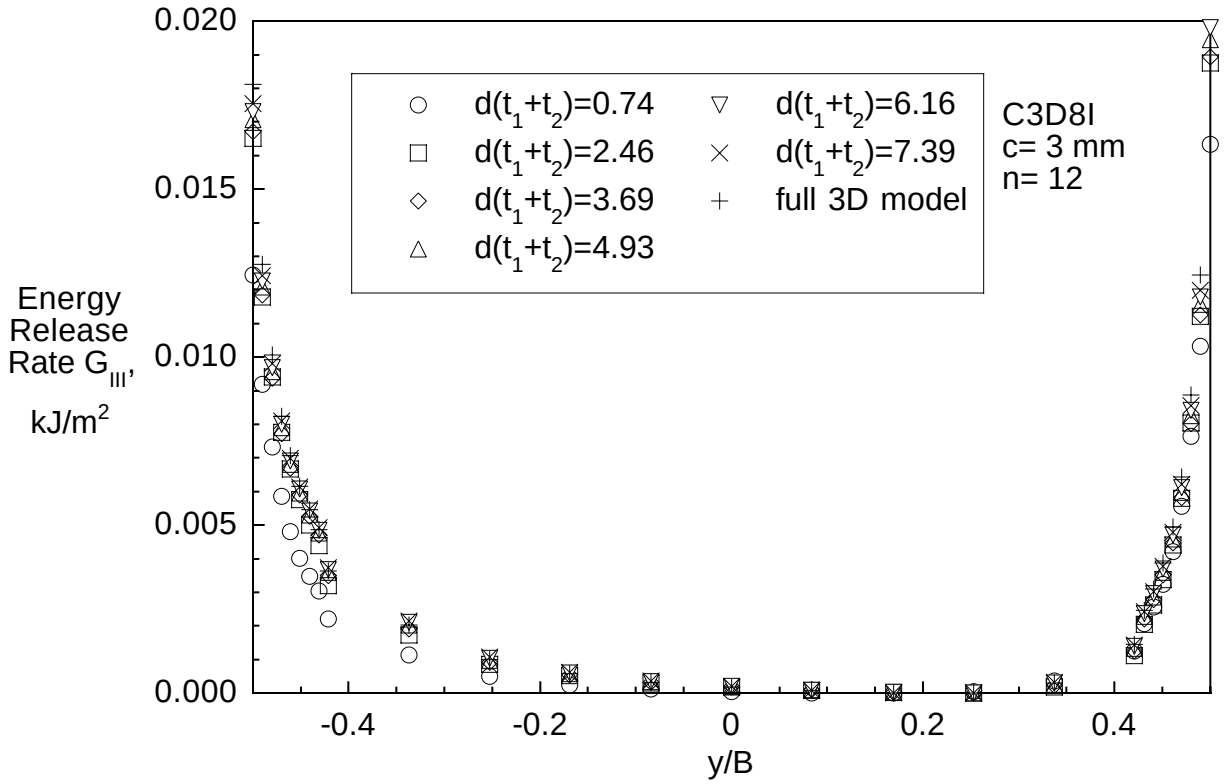

Figure 44. Mode III strain energy release rate distribution across the width of a SLB specimen with D±30 layup calculated using the shell/3D modeling technique

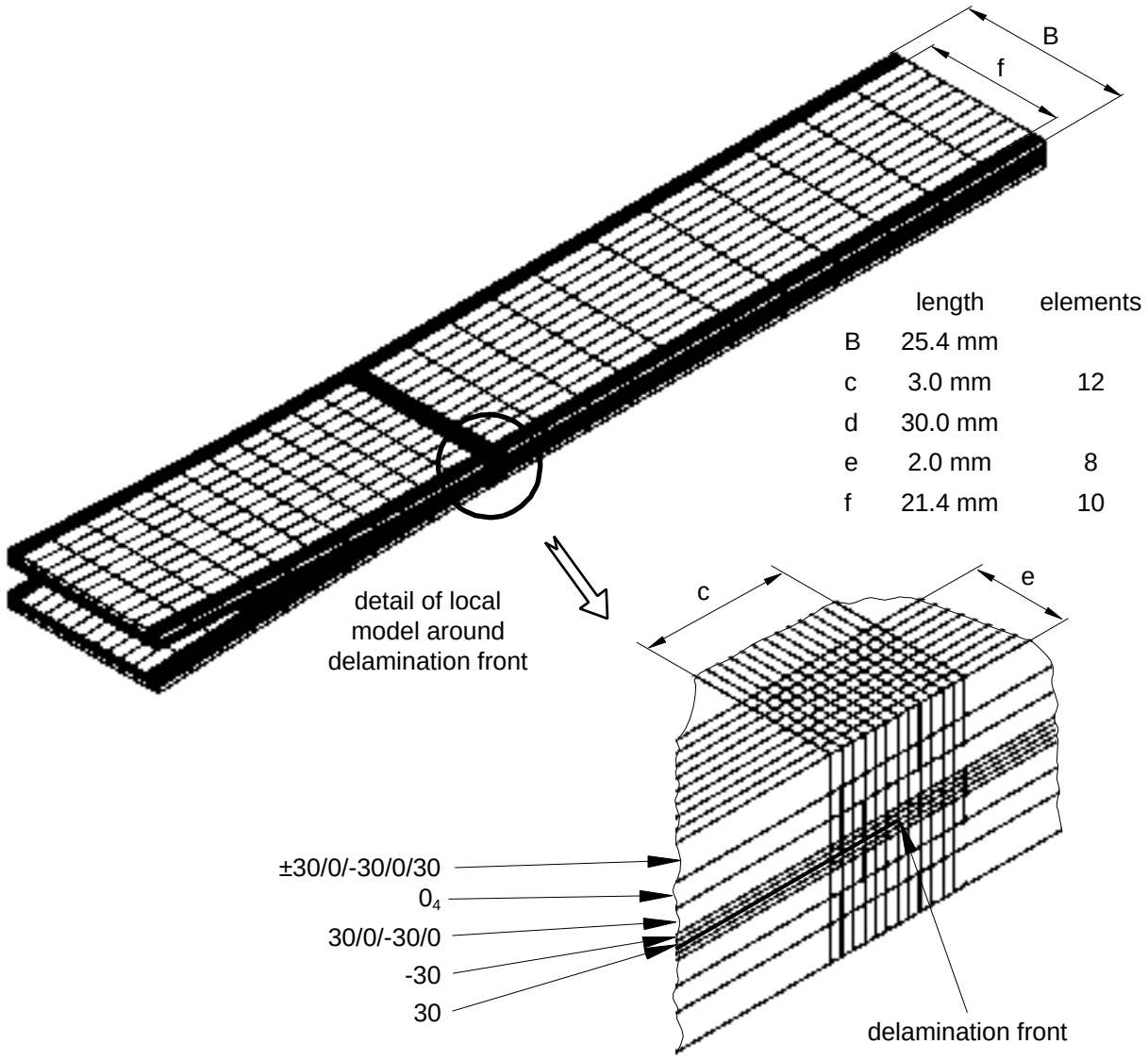

Figure 45. Finite element model of a DCB specimen with D±30 layup

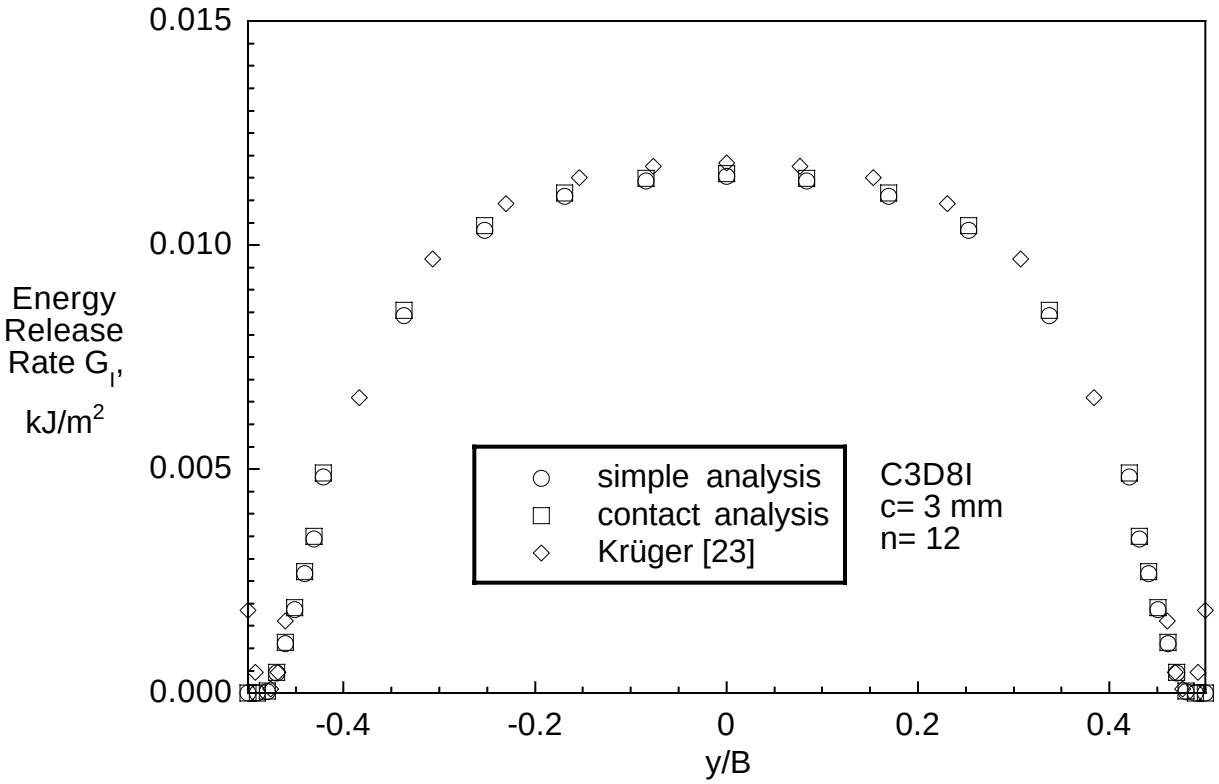

Figure 46. Influence of delamination surface contact on computed strain energy release rate distribution across the width of a DCB specimen with D±30 layup modeled with 8 noded elements

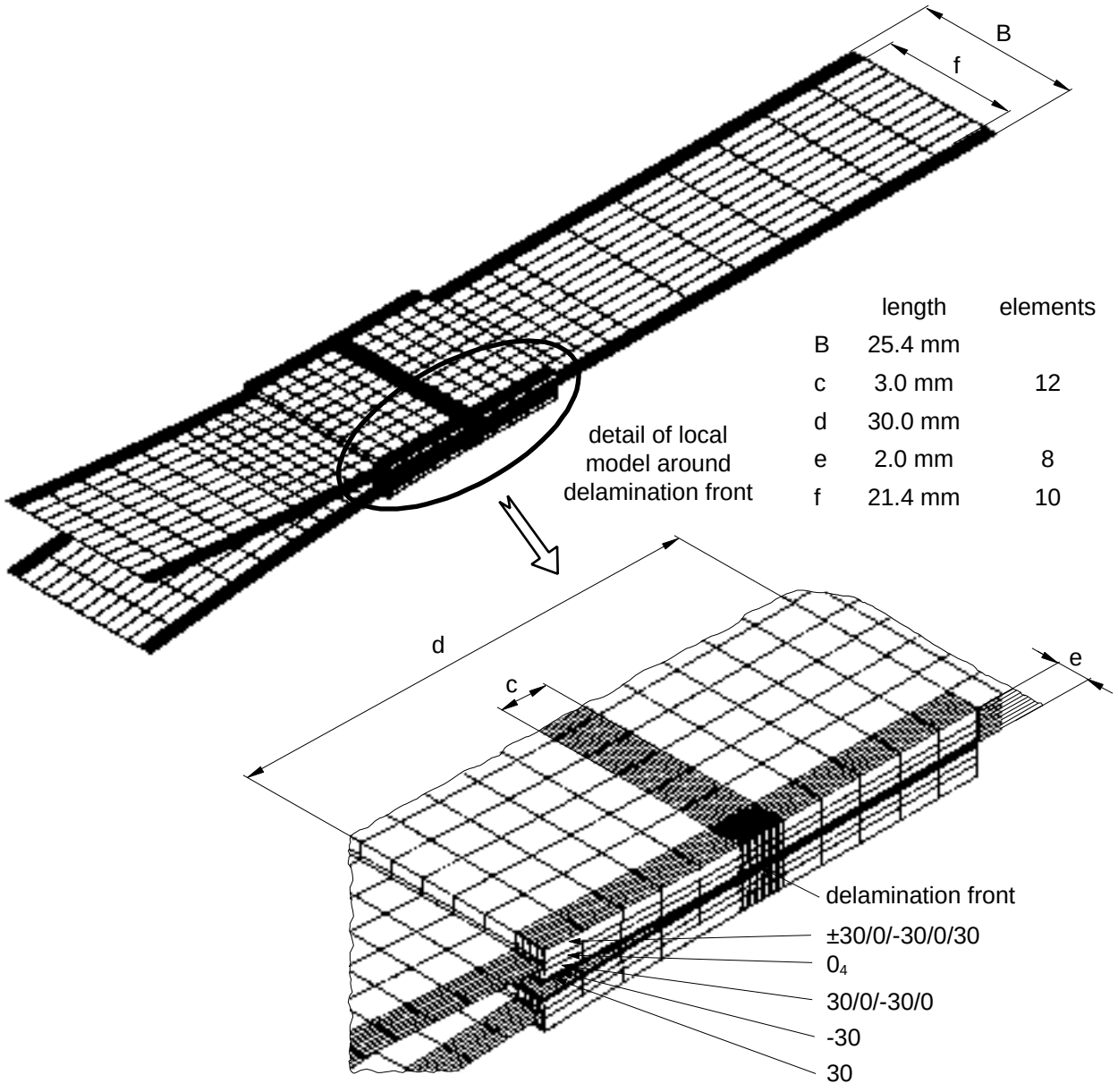

Figure 47. Shell/3Dfinite element model of a DCB specimen with D±30 layup

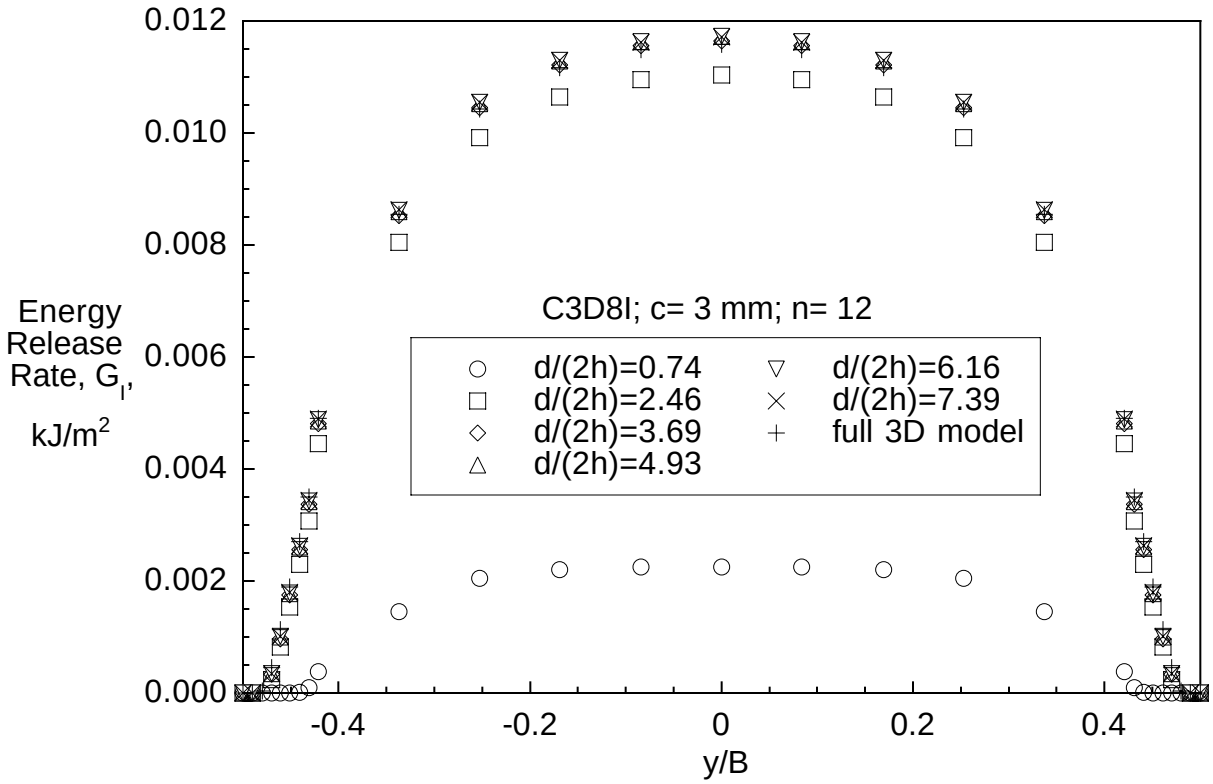

Figure 48. Mode I strain energy release rate distribution across the width of a DCB specimen with D±30 layup calculated using the shell/3D modeling technique

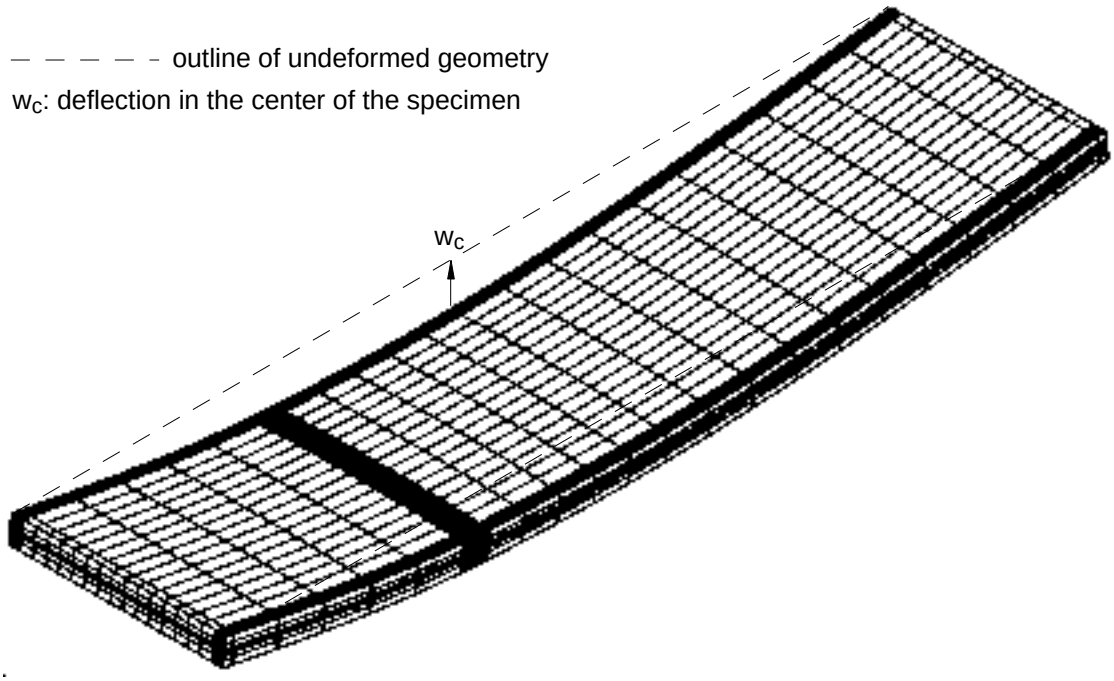

Figure 49. Finite element model of an ENF specimen with D±30 layup

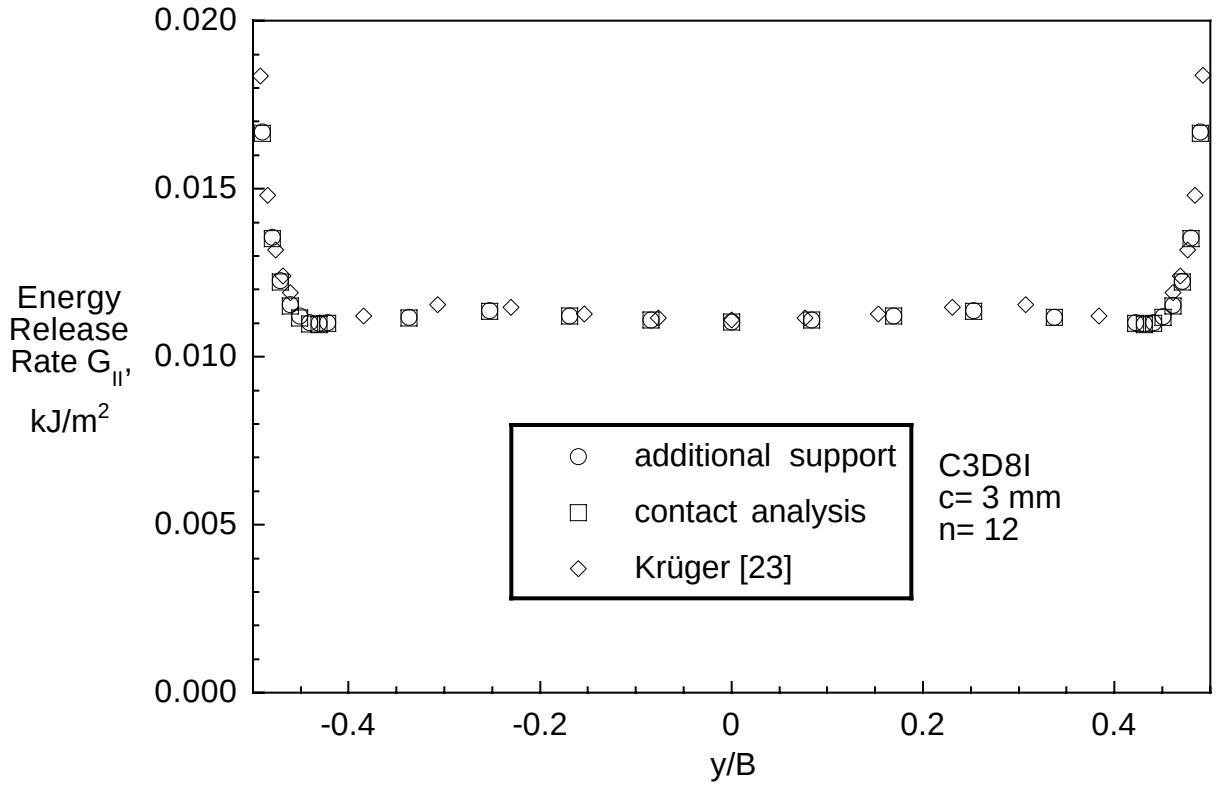

Figure 50. Influence of delamination surface contact on computed mode II strain energy release rate distribution across the width of an ENF specimen with D±30 layup.

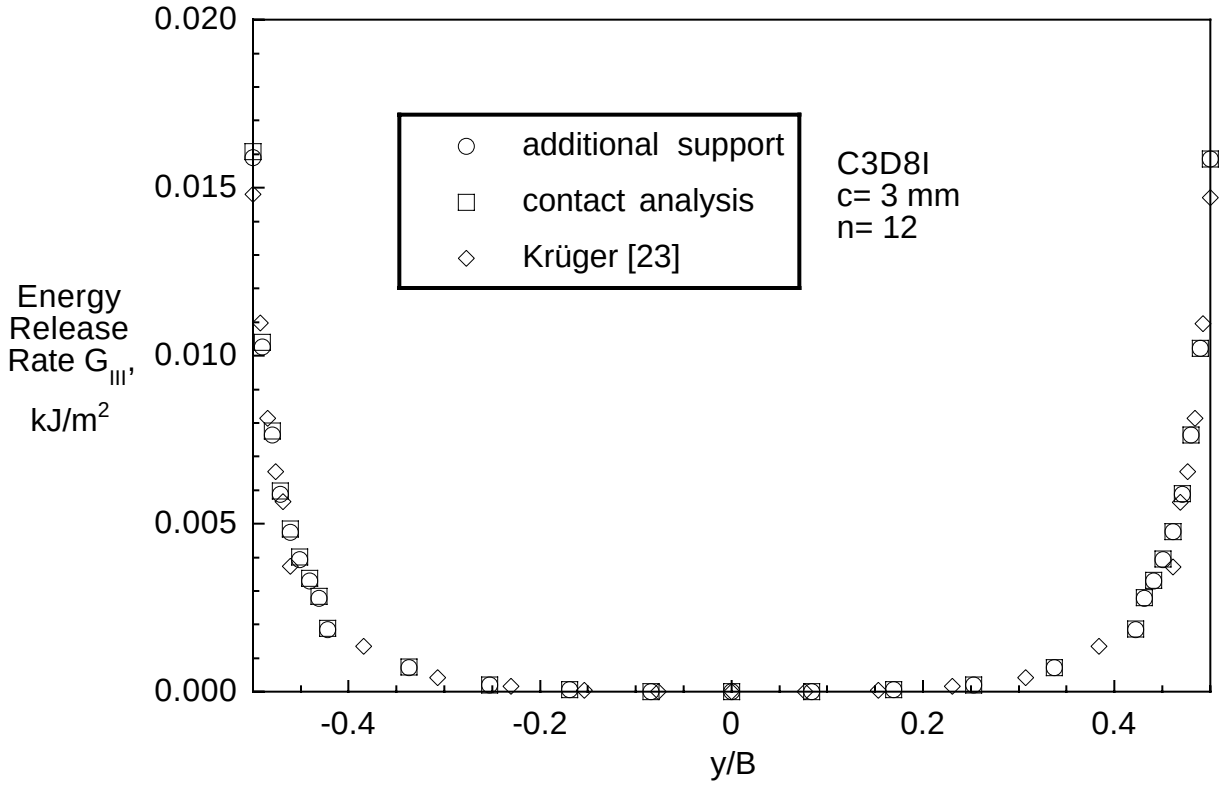

Figure 51. Influence of delamination surface contact on computed mode III strain energy release rate distribution across the width of an ENF specimen with D±30 layup.

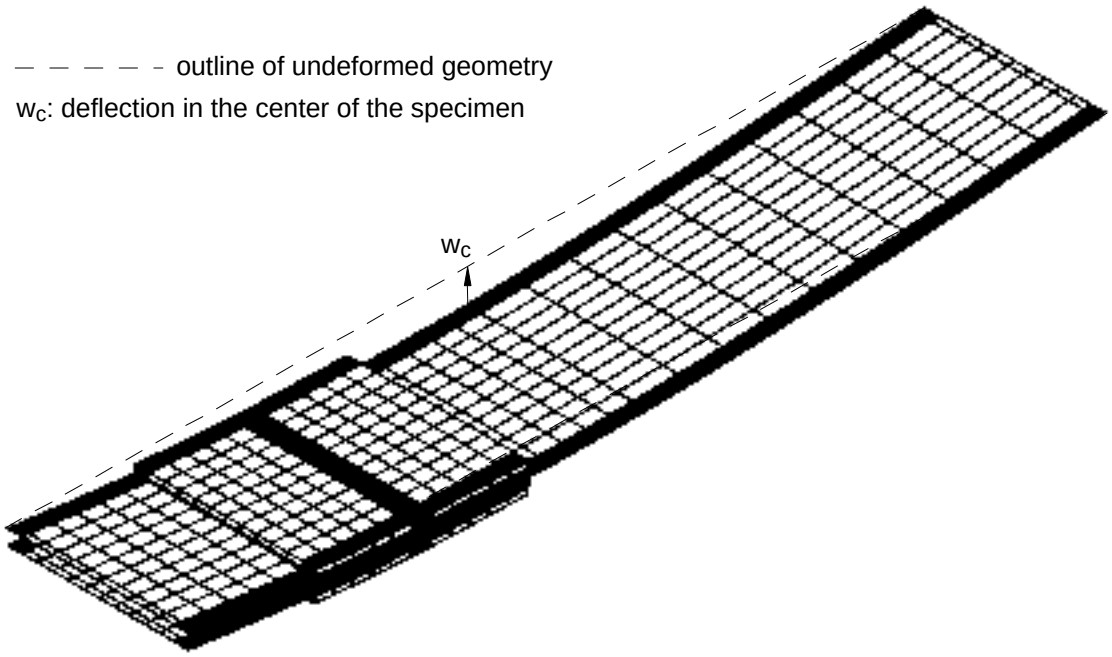

Figure 52. Shell/3Dfinite element model of an ENF specimen with D±30 layup (c= 3 mm, n=12, d= 30 mm)

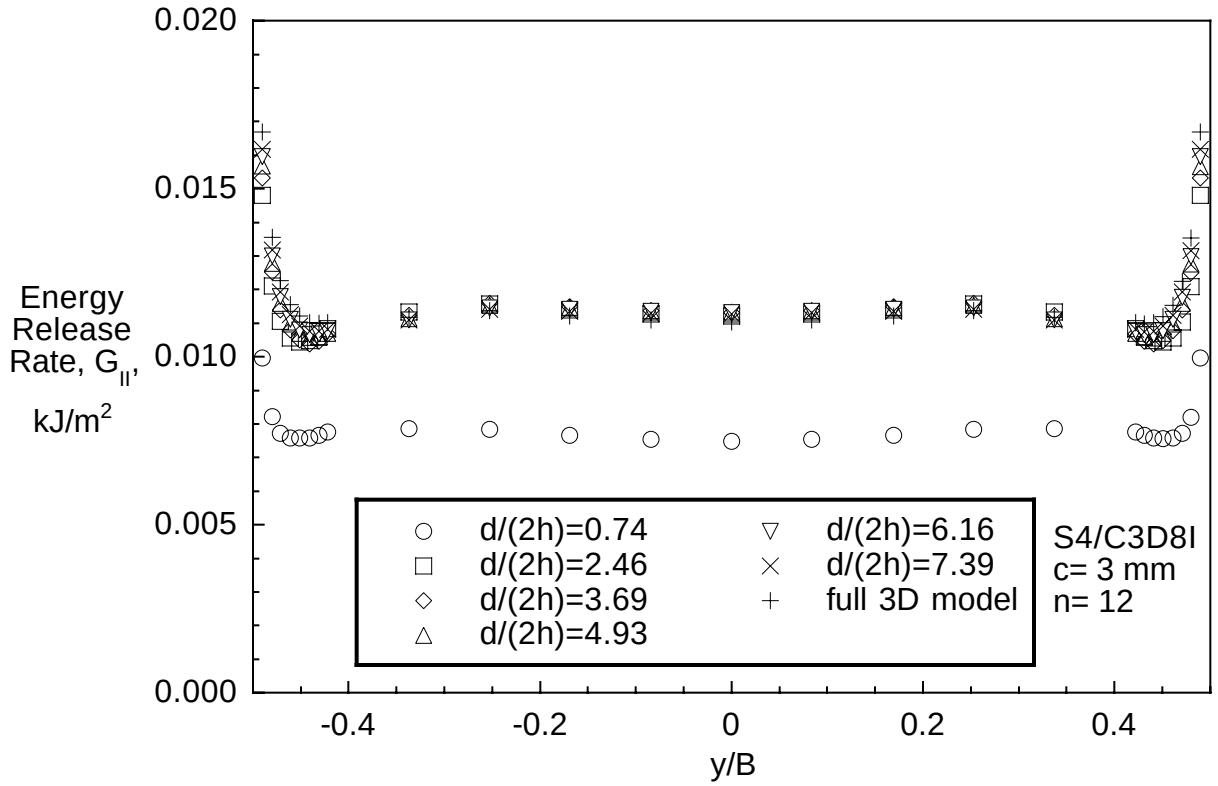

Figure 53. Mode II strain energy release rate distribution across the width of an ENF specimen with D±30 layup calculated using the shell/3D modeling technique

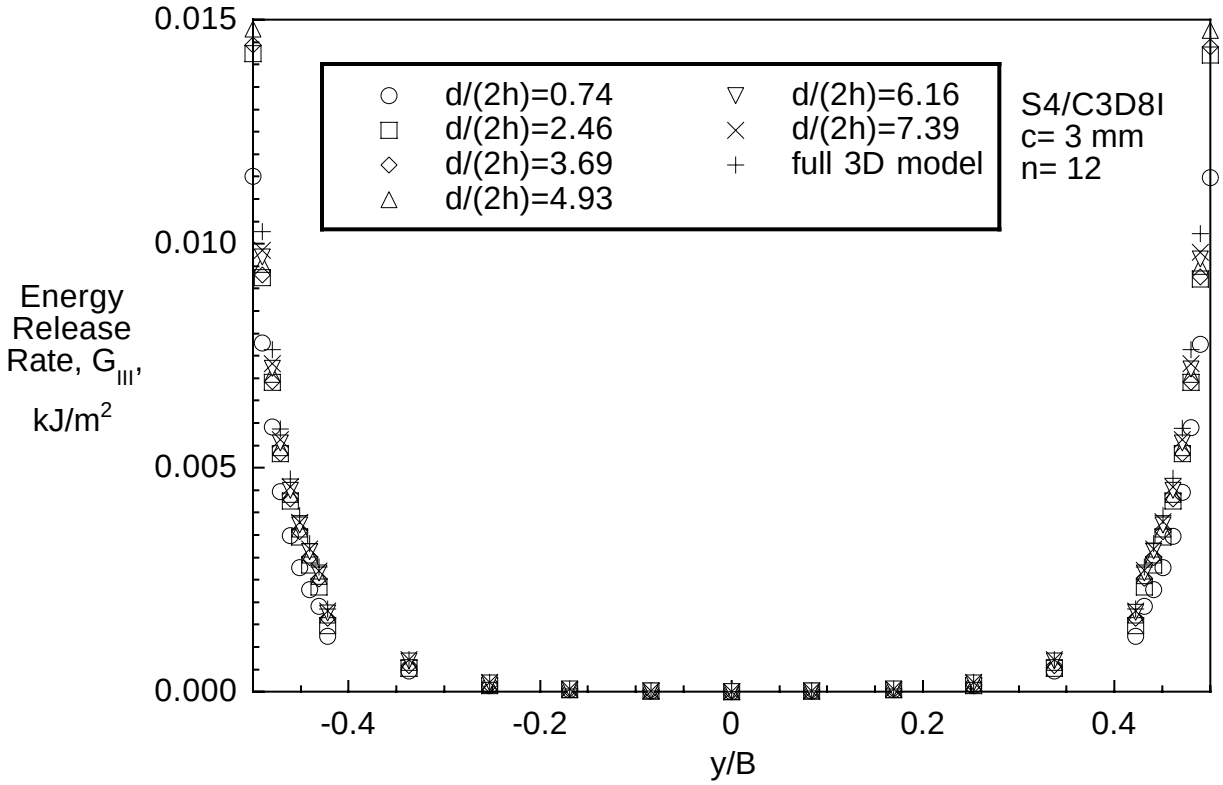

Figure 54. Mode III strain energy release rate distribution across the width of an ENF specimen with D±30 layup calculated using the shell/3D modeling technique

REPORT DOCUMENTATION PAGE

Form Approved
OMB No. 0704-0188

1. AGENCY USE ONLY (Leave blank)	2. REPORT DATE	3. REPORT TYPE AND DATES COVERED
	June 2000	Technical Memorandum

4. TITLE AND SUBTITLE
A Shell/3D Modeling Technique for the Analysis of Delaminated Composite Laminates

5. FUNDING NUMBERS
WU 581-10-21-01

6. AUTHOR(S)
Ronald Krueger and T. Kevin O'Brien

7. PERFORMING ORGANIZATION NAME(S) AND ADDRESS(ES)
NASA Langley Research Center
Hampton, VA 23681-2199

U.S. Army Research Laboratory
Vehicle Technology Directorate
NASA Langley Research Center
Hampton, VA 23681-2199

8. PERFORMING ORGANIZATION REPORT NUMBER
L-17977

9. SPONSORING/MONITORING AGENCY NAME(S) AND ADDRESS(ES)
National Aeronautics and Space Administration
Washington, DC 20546-0001
and
U.S. Army Research Laboratory
Adelphi, MD 20783-1145

10. SPONSORING/MONITORING AGENCY REPORT NUMBER
NASA/TM-2000-210287
ARL-TR-2207

11. SUPPLEMENTARY NOTES
Krueger: National Research Council Research Associate, NASA Langley Research Center, Hampton, VA
O'Brien: U.S. Army Research Laboratory, Vehicle Technology Directorate, NASA Langley Research Center, Hampton, VA

12a. DISTRIBUTION/AVAILABILITY STATEMENT
Unclassified-Unlimited
Subject Category 24 Distribution: Standard
Availability: NASA CASI (301) 621-0390

12b. DISTRIBUTION CODE

13. ABSTRACT (Maximum 200 words)
A shell/3D modeling technique was developed for which a local solid finite element model is used only in the immediate vicinity of the delamination front. The goal was to combine the accuracy of the full three-dimensional solution with the computational efficiency of a shell finite element model. Multi-point constraints provided a kinematically compatible interface between the local 3D model and the global structural model which has been meshed with shell finite elements. Double Cantilever Beam, End Notched Flexure, and Single Leg Bending specimens were analyzed first using full 3D finite element models to obtain reference solutions. Mixed mode strain energy release rate distributions were computed using the virtual crack closure technique. The analyses were repeated using the shell/3D technique to study the feasibility for pure mode I, mode II and mixed mode I/II cases. Specimens with a unidirectional layup and with a multidirectional layup were simulated. For a local 3D model, extending to a minimum of about three specimen thicknesses on either side of the delamination front, the results were in good agreement with mixed mode strain energy release rates obtained from computations where the entire specimen had been modeled with solid elements. For large built-up composite structures the shell/3D modeling technique offers a great potential for reducing the model size, since only a relatively small section in the vicinity of the delamination front needs to be modeled with solid elements.

14. SUBJECT TERMS
Composite materials; Fracture mechanics; Strain energy release rate; Finite element analysis; Virtual crack closure technique

15. NUMBER OF PAGES
72

16. PRICE CODE
A04

17. SECURITY CLASSIFICATION OF REPORT	18. SECURITY CLASSIFICATION OF THIS PAGE	19. SECURITY CLASSIFICATION OF ABSTRACT	20. LIMITATION OF ABSTRACT
Unclassified	Unclassified	Unclassified	UL